



Hochschule für Angewandte Wissenschaften Hamburg
Hamburg University of Applied Sciences

Master Thesis

Adrian Hurst

Development of a generic model to depict airspace-related trajectory inefficiencies for global air traffic scenarios

*Fakultät Technik und Informatik
Department Fahrzeugtechnik und Flugzeugbau*

*Faculty of Engineering and Computer Science
Department of Automotive and
Aeronautical Engineering*

Adrian Hurst

**Development of a generic model to depict
airspace-related trajectory inefficiencies
for global air traffic scenarios**

Master Thesis submitted as part of the Master's examination

in the course Aeronautical Engineering
at the department of Automotive and Aeronautical Engineering
of the faculty of Engineering and Computer Science
at the Hamburg University of Applied Science

in close collaboration with:
DLR – German Aerospace Center
Institute of Air Transportation Systems
Blohmstr. 20
21079 Hamburg

First Examiner: Prof. Dr.-Ing. Gordon Konieczny

Second Examiner: Prof. Dr.-Ing. Volker Gollnick

Supervisors: Dipl.-Ing. M.A. Robin Ghosh and Dipl.-Ing Benjamin Luehrs

Date of submission: 15.12.2015

Abstract

Adrian Hurst

Title of the Master Thesis

Development of a generic model to depict airspace-related trajectory inefficiencies for global air traffic scenarios

Keywords

Trajectory inefficiency, generic model, world regions, trajectory fragmentation

Abstract

In an ideal air transportation system, all aircraft using the airspace would be able to fly on optimal trajectories between their origin and destination. In reality, however, this ideal is not achievable due to various constraints entailing the worsening of trajectory efficiency. To enhance conventional simulations, the developed model depicts airspace-related trajectory inefficiencies required for the evaluation of prospective improvements or degradations of flight guidance by considering various disparities in different world regions. Due to inefficiency variations related to different flight phases and in favor of more precise simulation results the trajectory is split into three flight phases: departure, enroute and arrival. By means of these and in accordance to the passed world regions the trajectory is divided into fragments. The starting and ending coordinates of these fragments as well as the underlying inefficiencies are provided as input parameters for the subsequent simulation. In contrast to conventional simulation results, the results of the simulation regarding inefficiencies show an approximation to the available real data trajectories obtained from an online database.

Adrian Hurst

Thema der Masterthesis

Entwicklung eines generischen Modells zur Abbildung luftraumbezogener Trajektorien Ineffizienzen für globale Luftverkehrsszenarien

Stichworte

Trajektorien Ineffizienz, generisches Modell, Regionen, Trajektorien Fragmentierung

Kurzzusammenfassung

In einem idealen Lufttransportsystem wären alle Flugzeuge die den Luftraum nutzen in der Lage, auf optimalen Trajektorien zwischen deren Start- und Zielflughafen zu fliegen. In der Realität ist dieses Ideal jedoch nicht erzielbar, da unterschiedlichste Einschränkungen zur Verschlechterung der Trajektorien Effizienz beitragen. Um herkömmliche Simulationen dahingehend zu verbessern, bildet das entwickelte Modell luftraumbezogene Trajektorien Ineffizienzen ab, die zur Bewertung zukünftiger Verbesserungen oder Verschlechterungen der Flugführung benötigt werden und berücksichtigt dabei Ungleichheiten in unterschiedlichen Regionen. Durch Schwankungen der Ineffizienzen hinsichtlich unterschiedlicher Flugphasen und zugunsten genauerer Simulationsergebnisse wird die Trajektorie in drei Flugabschnitte unterteilt: Abflug, Enroute und Anflug. Mittels dieser und gemäß der durchflogenen Regionen wird die Trajektorie in Fragmente unterteilt. Sowohl die Start- und Endpunktkoordinaten dieser Fragmente als auch die zugrundeliegenden Ineffizienzen werden als Eingangsparameter für die nachfolgende Simulation bereitgestellt. Gegenüber herkömmlichen Simulationsergebnissen zeigen die Simulationsergebnisse unter Berücksichtigung von Ineffizienzen eine Annäherung an die von einer Online-Datenbank zur Verfügung stehenden Realdatentrajektorien.

Table of Contents

List of Figures	III
List of Tables	V
List of Words	VI
1 Introduction	1
2 Fundamentals	3
2.1 Status quo	3
2.2 Airspace-related trajectory inefficiencies.....	7
2.2.1 Vertical trajectory inefficiencies.....	8
2.2.2 Lateral trajectory inefficiencies.....	11
2.3 Classification of the global airspace	16
2.3.1 Macroscopic approach	16
2.3.2 Microscopic classification	25
2.4 Classification of lateral trajectory inefficiencies	29
3 Modeling trajectory inefficiencies	34
3.1 Important trajectory parameters.....	35
3.2 Modeling regions and flight phases.....	38
3.2.1 Macroscopic modeling.....	38
3.2.2 Microscopic modeling.....	39
3.3 Fragmentation of the GC-trajectory	40
3.3.1 Intersection points with polygons and small circles	40
3.3.2 Elimination of erroneous intersection points	44
3.3.3 Limitation to the model	46
3.4 Data processing and TCM simulation	48
3.4.1 Data provision for the TCM simulation.....	48
3.4.2 Simulation with TCM	48

4	Application of the model	53
4.1	Preparation of data extracted from the IAGOS data base.....	54
4.2	Simulation of exemplary trajectories with the TCM.....	61
4.2.1	Calculation of reference trajectories.....	63
4.2.2	Calculation of real data trajectories	64
4.2.3	Calculation of inefficient trajectories	65
4.3	Results.....	67
5	Conclusion and outlook	73
5.1	Conclusion.....	73
5.2	Outlook.....	76
A	Annex.....	77
	List of references	91
	Declaration of independence	96

List of Figures

2.1	The four layers of AIRCAST depicting the future ATS	4
2.2	Distinction between OD-pair, segment and fragment.....	5
2.3	Real data trajectories between YYZ and FRA	6
2.4	Relative frequency of enroute trajectory inefficiency factors.....	7
2.5	Vertical flight profile of a real data trajectory	10
2.6	Distribution of additional fuel burn	10
2.7	Real data trajectory versus great circle trajectory	12
2.8	Boundaries of world regions.....	18
2.9	Departures and arrivals at Frankfurt International Airport (FRA)	28
2.10	GC-trajectory and real data trajectory between DUS and YYZ	29
2.11	Departure and arrival flight phase	30
2.12	XML-structure of trajectory inefficiencies per time slice and region.....	32
3.1	Functional diagram of the model	34
3.2	GC-trajectory at the northern hemisphere.....	36
3.3	GC-trajectory crossing the anti-meridian	37
3.4	Simplified illustration of the Matlab-function flatearthpoly	39
3.5	Modeling the transition of flight phases.....	41
3.6	Intersection points of transregional small circles	42
3.7	Fragmented GC-trajectory between DUS and YYZ	43
3.8	Azimuth query of potential erroneous intersection points	45
3.9	Longitude-critical trajectory (DXB - SFO).....	47
3.10	Extension of the GC-trajectory	50
3.11	Compression of the GC-trajectory.....	52

4.1	Preparation sequence of IAGOS trajectory data.....	54
4.2	Comparison between raw data and smoothed trajectory.....	56
4.3	Depiction of IAGOS/MOZAIC flights executed in 2012.....	57
4.4	Detection principle of flight phase transitions.....	58
4.5	Simplified trajectory-splitting at the anti-meridian.....	60
4.6	GC-trajectories of IAGOS top 30 segments.....	63
4.7	Real data trajectories of IAGOS top 30 segments.....	65
4.8	Fragmented GC-trajectories of IAGOS top 30 segments.....	66
4.9	Distance, fuel burn, NO _x and ATR ₁₀₀ against GC per segment.....	69
4.10	Comparison of ATR ₁₀₀ components between FRA and PHL.....	70
4.11	Climate cost functions at FL380 derived with AirClim.....	71
A.1	FIRs by ATFM implementation status.....	77
A.2	FIRs by air traffic volume.....	78
A.3	Selection of IAGOS data.....	80
A.4	Result format of IAGOS data.....	80
A.5	Inefficiency analysis of real data trajectories.....	82
A.6	Relative frequency of Distance _{rel} per segment.....	87
A.7	Relative frequency of BurnedFuel _{rel} per segment.....	88
A.8	Relative frequency of ProducedNO _{x,rel} per segment.....	89
A.9	Relative frequency of ATR _{100,rel} per segment.....	90

List of Tables

2.1	Results of the aerodrome airspace analysis	27
2.2	Inefficiencies by region and segment for the AIRCAST base year 2012	31
3.1	Fragment coordinates for the flight between DUS and YYZ.....	43
3.2	Output of the model for a sample flight between DUS and YYZ.....	48
3.3	GC-distance and inefficient distance for the sample flight (DUS-YYZ)	50
4.1	Comparison of distance, fuel burn, NO _x and ATR ₁₀₀ relative to GC	67
A.1	Comparison of projects providing emission inventories.....	79
A.2	Available aerodromes from IAGOS database extraction.....	81
A.3	Distance relative to GC of IAGOS and the model.....	83
A.4	Burned fuel relative to GC of IAGOS and the model.....	84
A.5	Produced NO _x relative to GC of IAGOS and the model	85
A.6	ATR ₁₀₀ relative to GC of IAGOS and the model	86

List of Words

Abbreviations

AIRCAST	Air Travel Forecast
ARR	Arrival
ATC	Air Traffic Control
ATFM	Air Traffic Flow Management
ATM	Air Traffic Management
ATR	Average Temperature Response
ATS	Air Transportation System
BADA	Base of Aircraft Data
BF	Burned Fuel
CCF	Climate Cost Function
CIC	Contrail Induced Cloudiness
DEP	Departure
DFS	Deutsche Flugsicherung (German Air Traffic Services)
DLR	Deutsches Zentrum für Luft- und Raumfahrt (German Aerospace Center)
EASA	European Aviation Safety Agency
ENR	Enroute
FIR	Flight Information Region
FL	Flight Level
GC	Great Circle
IAGOS	In-Service Aircraft for a Global Observing System
IAS	Indicated Air Speed
IATA	International Air Transportation Association
ICAO	International Civil Aviation Organization
ISA	International Standard Atmosphere
ITCZ	Inner Tropical Convergence Zone
MOZAIC	Measurement of Ozone and Water Vapor on Airbus in-service Aircraft

OD	Origin-Destination based on city pairs
SESAR	Single European Sky ATM Research
SID	Standard Instrument Departure
STAR	Standard Instrument Arrival
TAS	True Air Speed
TCM	Trajectory Calculation Module
TOC	Top of Climb
TOD	Top of Descent

Symbols

α	Azimuth at origin	[°]
c	Coefficient of low-pass-filter	[-]
I	Inefficiency factor	[-]
λ	Longitude	[°]
φ	Latitude	[°]
r	Radius of aerodrome airspace	[nm]
s	Ground distance	[nm]
X	Intersection point	[-]

1 Introduction

In an ideal air transportation system (ATS), all aircraft would be able to fly on optimal trajectories through the airspace between their origin and destination leading to lowest flight time, fuel burn and exhaust emissions. In reality, this ideal is not achievable due to various constraints entailing the worsening of trajectory efficiency.¹

In this context, this Master Thesis describes the development of a generic model by depicting airspace-related trajectory inefficiencies required for the evaluation of prospective improvements or degradations of flight guidance efficiency by considering various assumptions and courses of alterations in different world regions. Therefore, the model will be an important component for the calculation of scenarios regarding global flight trajectories in future time slices until 2050 and enables the estimation of climate impacts due to trajectory inefficiencies. To investigate climate impact mitigation effects of operational and technological alterations of the future ATS the DLR (German Aerospace Center) project WeCare was started. For the development of scenarios regarding the ATS, firstly, a quantitative model of global air traffic is required and realized by AIRCAST (air travel forecast), a modular environment which allows the assessment of ATS growth against technological and efficiency improvements. It comprises a simulation of flight missions respectively trajectories which is performed by appropriate trajectory calculators to reproduce flight movements and their associated fuel consumption on the basis of simplified flight performance models. To this, the DLR developed the Trajectory Calculation Module (TCM) which is already applied to analyze and evaluate impacts of new technologies and operational strategies on the ATS. Until now, airspace-related effects are not taken into account within the scope of AIRCAST. Due to unknown future routings, great circle (GC) trajectories between the origin and destination aerodromes are considered in the simulations.² However, the consideration of airspace-related trajectory inefficiencies proves relevant to obtain more realistic simulation results enhancing the accuracy of air traffic scenarios.

¹ Cf. Reynolds (2014) [74], Chapter 1.

² By entering waypoints, the TCM is able to calculate any kind of trajectory, cf. Luehrs (2013) [57].

In order to get an understanding of airspace-related trajectory inefficiencies, Chapter 2 deals with the status quo of today's simulations and the required fundamentals such as the explanation of trajectory inefficiencies. Furthermore, the subdivision of the global airspace into regions is addressed to take potential regional inefficiency differences into account. Due to inefficiency differences between flight phases and in favor of a higher granulation and consequent more precise simulation results the trajectory is divided into three flight phases: departure, enroute and arrival. Finally, Chapter 2 deals with the classification of airspace-related trajectory inefficiencies by region specified for the base year 2012 from literature and kept constant for all time slices. This can be interpreted as a zero-improvement/-worsening scenario serving as a base line ATM technology scenario for further studies.

The development of the generic model is detailed in Chapter 3. Initially, it involves a brief description of important trajectory parameters for their further use within the model. This is followed by the modeling of predefined regions and flight phases which divide the trajectory into fragments creating the core of the model. The trajectory inefficiencies of these fragments are subsequently imported into the model and properly assigned. Finally, the model's output and the further processing within the simulation, executed with the TCM, are explained.

To validate the model, a use case is applied and detailed within Chapter 4. For this purpose, real data trajectories, extracted from the IAGOS (In-Service Aircraft for a Global Observing System) online-database, are prepared. To ensure significant results, three isolated simulations are executed. For comparison purposes, the first simulation calculates relevant parameters of conventional GC-trajectories representing the status quo of today's trajectory simulations. The second simulation calculates the same parameters for the corresponding real data trajectories by using IAGOS trajectory data. Thereupon, within a third simulation, the same GC-trajectories are simulated by means of the applied model and consequently depicting inefficient trajectories. Finally, the simulation results are compared to assess the added value of the model as well as to estimate the approximation to the available real data trajectories.

At the end, Chapter 5 summarizes the results of this Master Thesis and provides a brief outlook of potential pursuing investigations building on these results.

2 Fundamentals

The emphasis of this chapter is to provide a general introduction contributing to the understanding of airspace related correlations, required for this Master Thesis. This is reinforced by a description of the status quo (see Chapter 2.1) and the explanation of airspace related inefficiencies in association with their cause and point of origin (see Chapter 2.2). Moreover, this leads to a classification of world regions and the subdivision of the trajectory into flight phases (see Chapters 2.3) as well as the determination of location-specific inefficiencies related to different world regions and flight phases (see Chapters 2.4).

2.1 Status quo

For a quantitative assessment of potential climate impact mitigation strategies, a comprehensive modeling of different fields of the ATS and their interaction is required. Hence, the DLR project “WeCare” investigates climate impact mitigating effects of technological and operational alterations with regard to the future ATS.

WeCare, among other topics, pursues the goal to consider economic and operational boundary conditions within a global and realistic modeling and evaluation of the ATS until 2050. Initially, a forecast of future air traffic on fleet and network basis is required and realized by a generic model architecture, named AIRCAST, a modular environment considering 4435 cities throughout the world. The aim is to quantitatively link the two major socio-economic drivers, population and gross domestic product to future passenger air traffic network on city pair level which allows the assessment of the ATS growth against technological and efficiency improvements until 2050. In order to enable a simulation of alterations concerning the ATS, it is abstractly divided into four layers, each building on the information from the layer above (see Figure 2.1).¹ The final layer of AIRCAST (Trajectories Network) comprises a simulation of GC-trajectories respectively flight missions calculated by the TCM considering an altering ratio of aircraft generations and amount of aircraft in each seat category. The

¹ Cf. Ghosh et al. (2015) [25].

simulation, implemented by the TCM, uses simplified flight performance models of the EUROCONTROL Base of Aircraft Data (BADA 4.0). It calculates mission dependent values as fuel consumption, exhaust emissions and 3D emission inventories of CO₂ and non-CO₂ climate agents (such as water vapor (H₂O), Nitrogen Oxides (NO_x) and Contrail Induced Cloudiness (CIC)). The latter are generated by detailed modelling of flight profiles which is of particular importance when simulating the introduction of new technologies or operational measures.¹

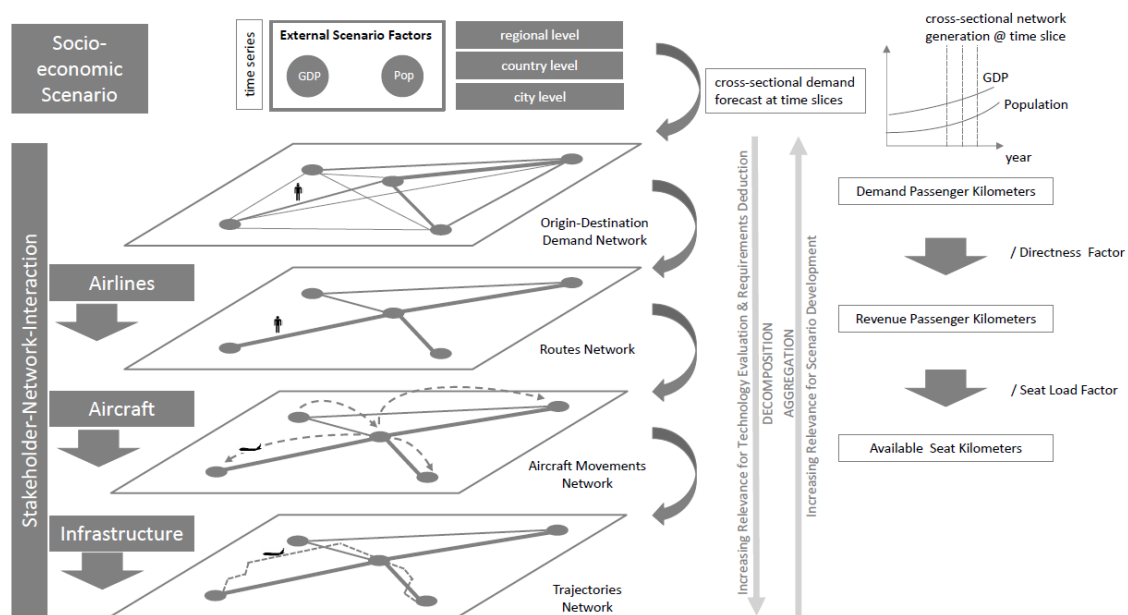


Figure 2.1: The four layers of AIRCAST depicting the future ATS ²

At first, the state of the art with respect to other emission inventory projects and in consideration of trajectory inefficiencies shall be investigated. In support of this, different emission inventories are analyzed to estimate whether and to what extent inefficiencies are considered for the calculation of fuel consumptions and consequent exhaust emissions. Here, of particular importance are those emission inventories also providing future prognoses.³ The results show that three of seven projects take inefficiencies into account which are listed below.⁴

¹ Cf. Ghosh et al. (2015) [26].

² Cf. Ghosh et al. (2015) [25].

³ Cf. Eyers et al. (2004) [21], Gardner et al. (1998) [24], Schaefer et al. (2013) [75], Schmitt and Brunner (1997) [76] and Sutkus et al. (2001) [79].

⁴ For a comparison of various emission inventories refer to Annex A.3.

- **DLR**, considering an average total value for global trajectory inefficiency.¹
- **AERO-MS**, considering 14 regions and their associated inefficiencies which give rise to 196 region pairs obtaining their inefficiency by building the average of both regions.²
- **AIM**, considering seven regions with different inefficiencies and the subdivision of the trajectory into the flight phases: departure, enroute and arrival.³

With the exception of AERO2k, the analyzed projects generate emission inventories on the basis of GC-trajectories.⁴ This has the key benefit of simple calculations and depictions of future unknown air traffic routings in simulations. Additionally, wind effects are commonly neglected in the considered projects due to unknown future wind fields. As in other projects, investigating climate impact mitigation effects and providing emission inventories, the simulations for WeCare are executed on the basis of GC-trajectories to model the segments of an OD-pair (Origin-Destination). OD-pairs denote the itinerary of passengers between their origin and destination which are not necessarily connected in a direct manner. Due to the possibility of changing flights, one OD-pair might consist of several flight segments (see Figure 2.2). Each flight segment describes one flight cycle from takeoff until landing and consists of several fragments.⁵

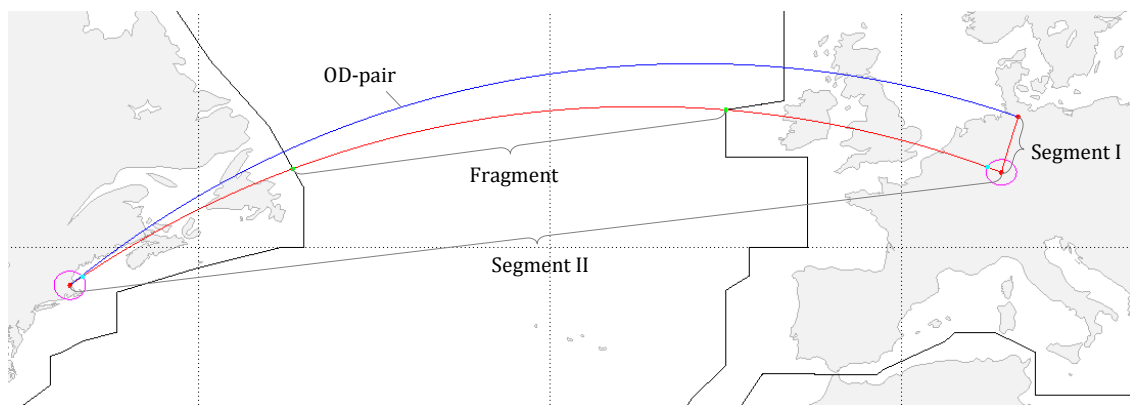


Figure 2.2: Distinction between OD-pair, segment and fragment

¹ A global ATM inefficiency of 7.0 % was estimated for the year 2010, cf. Schaefer et al. (2013) [75].

² Cf. EASA (2010) [12].

³ Cf. Krammer (2011) [55].

⁴ Cf. Gardner et al. (1998) [24], Schaefer et al. (2013) [75], Simone (2013) [78], Schmitt and Brunner (1997) [76], Sutkus et al. (2001) [79] and Wilkerson et al. (2010) [80].

⁵ The fragmentation of the trajectory constitutes the core of the model which is detailed in Chapter 3.3.

For the spatial depiction of takeoff and landing aerodromes, city coordinates are used instead of aerodrome coordinates.¹ Their coordinates can substantially deviate from each other, especially were the aerodrome is located far outside the city. However, due to the lateral granulation of 3D emission inventories ($1^\circ \times 1^\circ$)² the distance of the aerodrome from its city is assumed to be closer than 1° of latitude and longitude to the associated city. In total, 4435 cities with at least one passenger demand in 2012 are taken into account. If there is more than one aerodrome per city, only the largest³ is considered.⁴

Until now, simulations executed for WeCare do not account for trajectory inefficiencies. For this purpose, Figure 2.3 illustrates real trajectories between YYZ (Toronto Pearson International Airport) and FRA (Frankfurt International Airport) against their GC-trajectory (red line). In total, 43 real trajectories from YYZ to FRA are depicted generating a mean enroute inefficiency of approximately 1.75 percent.⁵

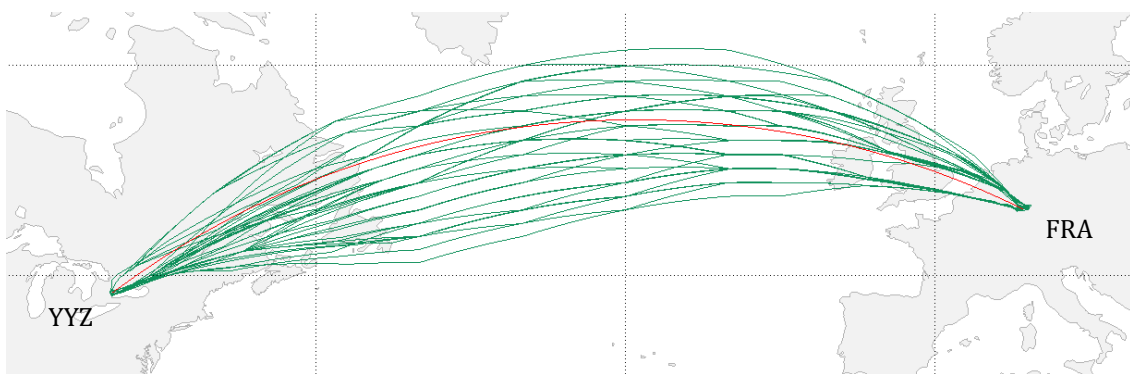


Figure 2.3: Real data trajectories between YYZ and FRA

As shown in Figure 2.3, the real data trajectories (green) diverge from their GC-trajectory (red). The frequency distribution of the same flights is illustrated in Figure 2.4 demonstrating the relevance of considering trajectory inefficiencies to improve simulation results for today and the future.

¹ Cf. Ghosh et al. (2015) [26].

² The resolution of emissions inventories of $1^\circ \times 1^\circ$ is currently applied at the DLR institute of air transportation systems.

³ In this context “largest” means highest volume of passengers.

⁴ Within this Master Thesis aerodromes are considered instead of cities. For further explanations see Chapter 2.3.2.

⁵ The calculation of enroute inefficiency is described in Chapter 4.1.

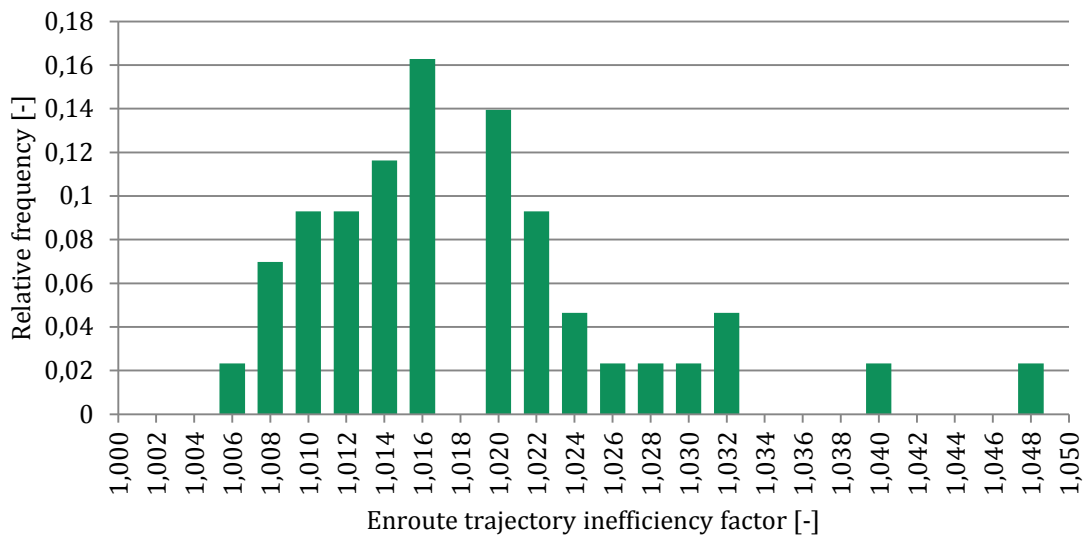


Figure 2.4: Relative frequency of enroute trajectory inefficiency factors

When considering the distribution of the enroute inefficiency factor depicted in Figure 2.4 two outliers to the right are clearly evident potentially distorting the results. Since this also applies for other segments, the median value proves more resistant against these outliers being therefore more representative concerning trajectory inefficiencies and related parameters. The median value for the same trajectories amounts approximately 1.47 percent which better reflects actual trajectory inefficiency distribution.

For a better comprehension of trajectory inefficiencies, the following chapter provides the required definitions and explanations regarding vertical and lateral trajectory inefficiency.

2.2 Airspace-related trajectory inefficiencies

Within the airspace, aircraft fly on four dimensional flight trajectories between their origin and destination. A trajectory comprises three components: a lateral, a vertical and a speed component. While the latter two are not considered within this Master Thesis the horizontal routing contains changes in heading whereas the vertical component comprises the flight profile including changes in altitude. Dependent on the prevailing airspace and weather situation, a real trajectory might occasionally change

its vertical and lateral course, even though connecting the same aerodromes.¹ In contrast to real trajectories a GC-trajectory constitutes the shortest path between two arbitrary points (origin and destination) along the earth's surface.² The difference between the actual and the corresponding GC-trajectory can be interpreted as a sort of inefficiency being still a general term with different definitions dependent from where it is measured and on what perspective it is looked at.³ Therefore, within the ATS each participant has its own perception of inefficiency which holds true for trajectory inefficiency. It is measured from a single aircraft perspective, however in reality aircraft do not fly alone in the airspace. When considering a system point of view, there is a trade-off between efficiency, capacity and safety. Consequently, by means of today's technology, a 100 % efficient trajectory is neither feasible nor optimal without compromising in capacity or safety.

Like the trajectory itself, trajectory inefficiency can be split into a vertical and a lateral component as well. However, the modeling of trajectory inefficiencies within this Master Thesis only considers the lateral component.⁴

2.2.1 Vertical trajectory inefficiencies

Definition

Vertical trajectory inefficiency is defined as the deviation of the actual vertical flight profile from the optimal vertical flight profile.⁵

This subchapter gives a brief introduction in order to better understand the term vertical trajectory inefficiency: The vertical component of a flight trajectory comprises all changes in altitude of the entire flight, such as initial climb, level-off or final descent into the destination aerodrome (see Figure 2.5). As there are different potential causes of vertical trajectory inefficiency resulting from the inability of aircraft to fly an optimal vertical flight profile, differentiation is normally made between two types,

¹ Airspace conditions altering the trajectory are detailed in the following subchapters.

² A great circle represents the intersection of the earth's surface with a plane passing through the center of the earth. Therefore, all longitudes and the Equator are great circles, cf. Mathworks [62].

³ Cf. Eurocontrol (2013) [16], page 60.

⁴ The lateral component of trajectory inefficiency is explained in Chapter 2.2.2.

⁵ Cf. Civil Aviation Authority (2015) [6].

flight level capping and intermediate level-off. Whereas flight level capping primarily affects short haul flights, the consequence of intermediate level-off can affect short haul flights as well as long haul flights.¹

Flight level capping

Flight level capping describes an Air Traffic Flow Management (ATFM) procedure to restrict a flight to a certain altitude at which it is allowed to operate. Usually it is applied to limit air traffic entering a certain vertical sector of the airspace contributing to the balancing of capacity and demand. For this purpose, short haul flights are separated from overflying long haul traffic. Consequently, affected short haul flights are prevented from climbing to their optimum cruising flight level generating additional fuel burn as well as exhaust emissions.

Intermediate level-off

This ATFM procedure is commonly applied to interrupt the climb or descent phase of a flight and primarily results from traffic separation or other operational causes, for instance to delay the descent of aircraft into a congested airspace sector by means of intermediate level-offs. Consequently, affected flights are kept at uneconomical altitudes also generating additional fuel burn and exhaust emissions.²

Figure 2.5 shows a vertical flight profile in which the green solid line represents a vertical flight profile of a real data trajectory. It comprises a level-off during the climb phase ① entailing a delayed top of climb (TOC), a constant cruising flight level with a step-climb ② to a more efficient flight level (for instance due to a change in heading³ or mass) and finally an interrupted descent ③ with a consequent premature top of descent (TOD). In addition, flight level capping is represented by the dashed line ④ where some vertical constraints affect the flight. Both profiles are illustrated against the same associated ground distance.

¹ There are different definitions of short and long haul flights, however, short haul flights are assumed to be shorter than 594 nm (1000 km) and long haul flights are assumed to be longer than 1620 nm (3000 km), cf. Mensen (2013) [68], page 15.

² Cf. Eurocontrol (2008) [15].

³ A change in heading usually entails a change of relative wind direction. Consequently, in favor of better wind conditions, flight levels are changed to reduce total flight time.

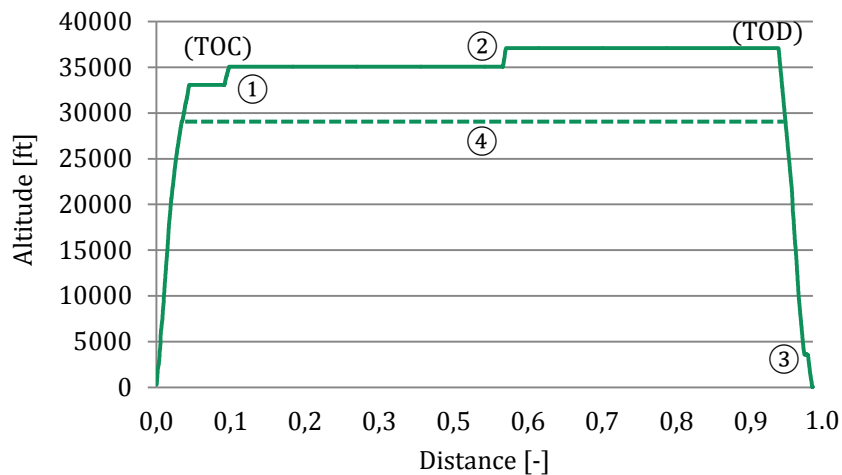


Figure 2.5: Vertical flight profile of a real data trajectory

To evaluate the effects of vertical trajectory inefficiency, Eurocontrol composed a traffic sample based on correlated position report data of 12 July 2007 comprising 26624 flights. As a result of the study, flight level capping was subject to approximately 12 % of the flights whereas approximately 19 % of the flights were affected by interrupted climbs and approximately 42 % by interrupted descents. With respect to total additional fuel burn (7-11 % of optimum fuel burn), Figure 2.6 (left side) shows that approximately 7 percent result from vertical trajectory inefficiencies and approximately 43 percent from lateral trajectory inefficiencies. Other additional fuel burn (50 percent) might be traced back to airborne delays and taxi inefficiency.

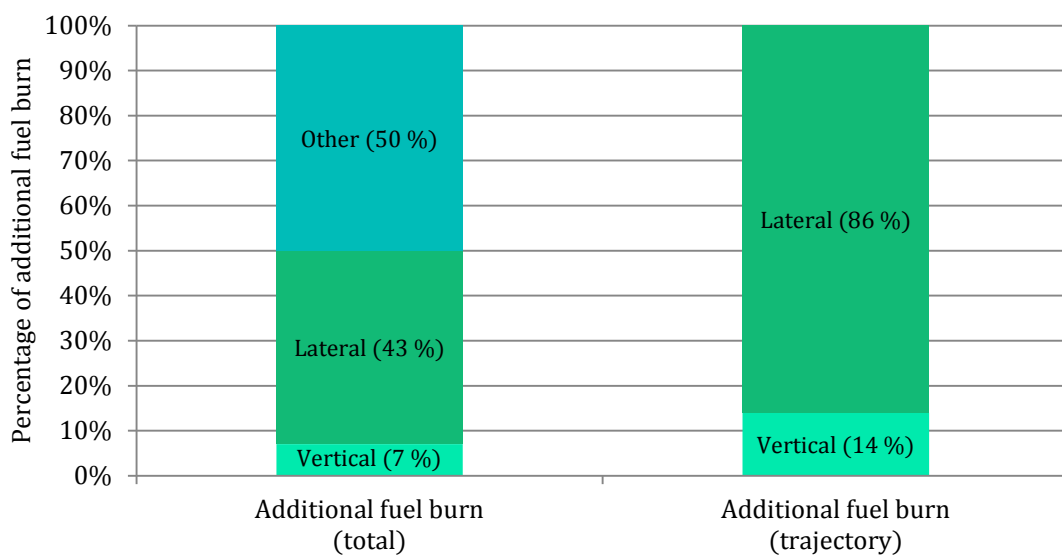


Figure 2.6: Distribution of additional fuel burn

Consequently, when splitting trajectory inefficiency into its components, Figure 2.6 (right side) shows that approximately 14 % result from vertical and about 86 % from lateral trajectory inefficiencies. However, it is very difficult to accurately estimate vertical trajectory inefficiencies, since aircraft mass, weather conditions and standard operating procedures can have substantial impact on the ideal vertical flight profile. For this reason, uncertainty of determining vertical trajectory inefficiency is very high and compared to the values above actual values may substantially differ. Even though there are negative impacts generated by vertical trajectory inefficiencies, they remain relatively small compared to lateral trajectory inefficiencies.¹ Against this background, vertical inefficiency is not considered for the purpose of this Master Thesis.

2.2.2 Lateral trajectory inefficiencies

Definition

For the purpose of this Master Thesis, lateral trajectory inefficiency is defined as the horizontal deviation of a zero-wind trajectory from its corresponding GC-trajectory resulting in a trajectory elongation expressed as extended ground track distance.

Consequently, ground track extension is the Key Performance Indicator (KPI) of trajectory inefficiency, calculated as a percentage of GC-distance. The common measure of distance is a minute of arc or a nautical mile (nm).² To illustrate this context it is useful to set an example. Based on a GC-distance of 500 nm the track is extended by 50 nm due to airspace-related circumstances; the resulting trajectory inefficiency then amounts to 10 percent. The metric of lateral trajectory inefficiency regards “longitudinal” inefficiency (elongation of the trajectory) and is not to be confused with “transversal” inefficiency which would express the offset of the trajectory to either side of the GC-trajectory. Figure 2.7 illustrates a real data trajectory between Dusseldorf International Airport (DUS) and Toronto Pearson International Airport (YYZ). It is obvious that the real trajectory sporadically deviates from the GC-trajectory. Relative trajectory inefficiencies are greatest in the vicinity of the aerodromes where aircraft depart and approach. This becomes evident when considering Figure 2.11.

¹ Cf. Eurocontrol (2008) [15].

² The nautical mile is generally used in aviation to express distance (1 nm = 1852 m), cf. Mensen (2013) [68], page 209.

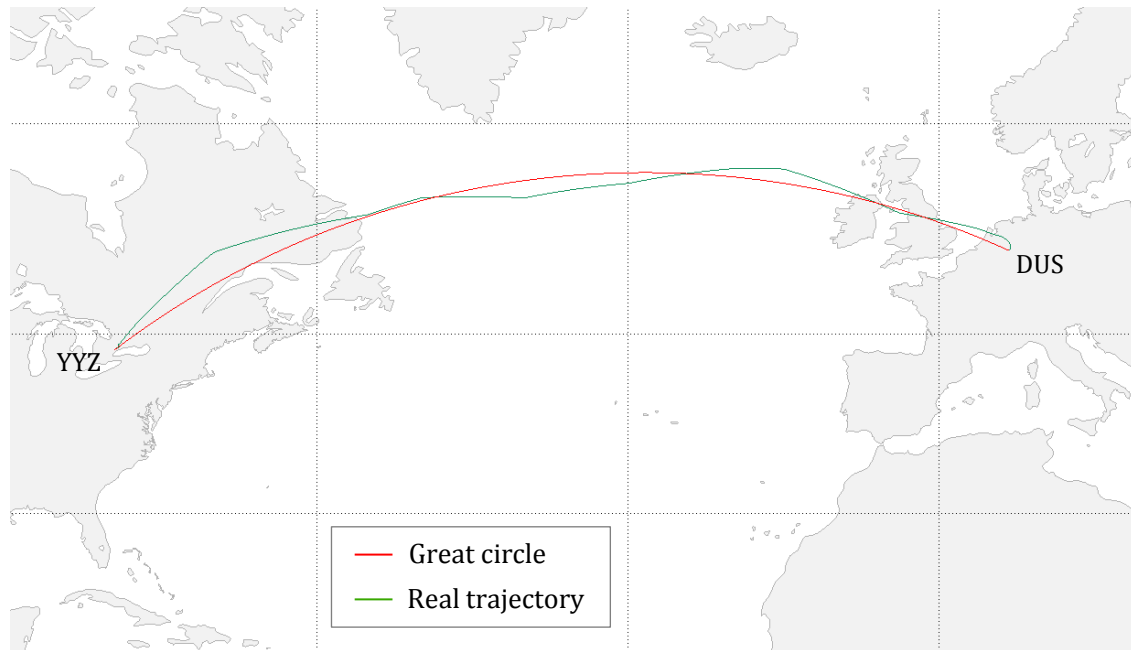


Figure 2.7: Real data trajectory versus great circle trajectory

In trajectory efficiency analysis, GC-trajectories are frequently used as reference because easy to calculate.¹ However, in the choice of routes, wind plays an important role. Therefore, GC-trajectories are not necessarily the shortest route in terms of air distance respectively flight time requiring even more fuel than actually flown routes what makes extended ground track distance hardly interpretable as inefficiency.² But, wind-optimal routes, defined as those minimizing total flight time, are difficult to be calculated, especially for future scenarios, since accurate wind field information is required to determine air distance for all flights. Consequently, due to dominant wind directions, the effect of wind is assumed to cancel out with a sufficient number of bi-directional flights.³ For those reasons, wind effects are neglected within this Master Thesis.

In the following, there are several causes illustrated, primarily related to operational inefficiencies, contributing to the worsening of trajectory efficiency.

¹ Cf. Kettunen (2005) [54], Reynolds (2008) [72] and Eurocontrol (2014) [17].

² Cf. Reynolds (2014) [74], page 66.

³ Cf. Reynolds (2014) [74]. However, this does not necessarily comply with reality since the negative effect of headwind is greater than the positive effect of tailwind for a given ground track.

Route network design

Flights are planned and executed according to allocated airways defined by associated waypoints. In most cases, the selected waypoints do not necessarily coincide with the GC-trajectory. So it is apparent that there already is a deviation during the planning stage of a flight. Consequently, when considering route network design only, trajectory inefficiency (as it is defined above) would potentially be lowest in the case where waypoint density is highest.¹

Restriction and fragmentation of the airspace

In some areas within the airspace flights underlie restrictions, for instance due to military activities such as artillery firing or guided missiles. Due to these hazards it is prohibited to operate aircraft in these areas when the airspace is so called “active”.

The fragmentation of the airspace, for instance in Europe which comprises approximately 650 sectors, entails inconsistency and problems in the seamless processing of air traffic. Additionally, different regulations and organizations as well as the legacy of the national approach regarding ATFM (instead of shifting to a European level) amplify this effect.²

Congestion of the airspace

Congestion can be defined as the exceedance of the capacity of an infrastructure.³ High air traffic volumes, primarily in the vicinity of major aerodromes cause the congestion of the air traffic flow which frequently results in holding or vectoring procedures. Overflying traffic potentially avoids the airspace of high congestion levels by flying around these airspaces with consequent additional ground track distance.

Differences in air navigation charges

A further impairment of trajectory efficiency is represented by occasional significant differences in air navigation charges between flight information regions (FIR). It is apparent, that aircraft operators accept extra ground track distance combined with higher fuel burn and emissions to compensate high air navigation charges in expen-

¹ Cf. Howe-Veenstra (2011) [32], Chapter 6.

² Cf. European Commission (2013) [20].

³ Cf. Economic Research Center (1998) [13], page 13.

sive airspaces.¹ A consistent air navigation charge would potentially eliminate this appeal.

Departure and arrival procedures

For aerodynamic reasons, takeoff and landing are always performed against the prevailing wind. Owing to changes in wind direction and velocity the windward runway is normally used and Standard Instrument Departures (SID) and Arrivals (STAR) consequently assigned to the active runway. During departure and arrival, aircraft proceed according to the defined standard instrument procedures to avoid obstacles and to ensure noise abatement at residential areas. Thus, the trajectory does not necessarily depart or approach the aerodrome by means of the shortest possible route.²

Holding and radar vectoring

Holding and radar vectoring are generally used once the demand of approaches exceeds runway capacity. Both procedures have one common feature: the delay of airborne aircraft. Holding is required if an approaching aircraft is not able to continue its landing approach due to operational or traffic-related reasons. In this case an aircraft enters a holding pattern for a certain period of time.

Radar vectoring is primarily used to adjust the arrival sequence at the destination aerodrome. In this context, a radar vector usually consists of heading, altitude or speed instructions or a combination of these.

Adverse weather conditions

Trajectory efficiency can significantly be influenced by the presence of adverse weather leading to spacious deviations from the GC-trajectory. There are several adverse weather conditions such as thunderstorms (especially within the Intertropical Convergence Zone (ITCZ)) producing heavy turbulence, hail and icing. Fully developed thunderstorms cannot be overflown due to their very high tops.³ For safety reasons flight crews bypass areas of hazardous weather phenomena accepting long route diversions resulting in increased flight time, fuel burn and exhaust emissions.

¹ Cf. Reynolds (2009) [73].

² The aerodrome airspace is a fictive cylindrical airspace around each considered aerodrome defined for the purpose of this Master Thesis to depict different flight phases. For more information refer to Chapter 2.3.2.

³ Cf. Hack (2008) [29].

Unpredictable technical incidents

In most cases technical incidents occur unexpectedly and are therefore not predictable. These can have different causes and extents such as the sudden malfunction of an instrument landing system (ILS) during low visibility conditions which could have the effect of aircraft entering holdings or proceed to an alternate aerodrome resulting in increased trajectory inefficiency. Furthermore, any kind of technical incident affecting an airborne aircraft entails the prioritization of this flight and forces other traffic into holdings until the annulment of the emergency.

However, the causes of trajectory inefficiency mentioned above do not necessarily occur everywhere to the same extent. They primarily depend on regional differences such as the presence of the ITCZ which is roughly situated in the vicinity of the Equator but subject to seasonal fluctuations.¹ On the one hand it would therefore have massive impacts considering the Indian Ocean or South America. But, on the other, there is no effect regarding the North Atlantic. Flights passing through regions where the ITCZ predominates are potentially more prone to detouring caused by adverse weather than by other factors. Another regional dependence of trajectory inefficiency constitutes the congestion of the airspace. Flights within regions of high air traffic volume are usually more vulnerable to holding or radar vectoring than flights within regions comprising lower air traffic density. In this context it can be seen, that the level of airspace congestion strongly depends on air traffic volume. Furthermore, the implementation status of ATFM measures and the ability of air navigation service providers to handle air traffic at capacity limits have substantial impact on the airspace congestion level.²

Both, the implementation status of ATFM measures and air traffic volume are therefore assumed to substantially affect trajectory efficiency and spatially differ significantly. For this reason the following chapter provides a classification of the global airspace with regard to trajectory inefficiency to enable the evaluation of prospective improvements or degradations of flight guidance by considering various assumptions in different world regions.

¹ Cf. Hack (2008) [29].

² An overview of FIR related information can be found online at the ICAO GIS viewer, cf. ICAO [40].

2.3 Classification of the global airspace

For the purpose of ATM, the atmosphere is divided into flight information regions (FIRs) reaching from ground or sea level up to high flight levels (FL).¹ However, FIRs do not necessarily follow national borders, but comply with air traffic flows making them particularly applicable for the spatial delineation of world regions.

2.3.1 Macroscopic classification

This chapter deals with the classification of the global airspace into world regions. The classification has the primary objective of generating coherent regions with preferably homogeneous inefficiencies where alterations of infrastructural technologies and ATFM measures will most likely develop in a similar manner. In particular, when considering the future development of the ATS (for instance after Single European Sky (SESAR)², US NextGen³ implementations or the OneSKY⁴ Australia program). ATFM measures are used to balance air traffic demand with airspace and aerodrome capacity by ensuring the most efficient handling of air traffic. This is achieved by using the maximum possible capacity (without exceedance) specified by the corresponding air navigation service providers.⁵ ATFM measures are for instance:

- Allocating and updating of departure, enroute and arrival slots;
- Re-routing of traffic;
- Alternate flight profiles; and
- Minutes- and mile-in-trail assignment.⁶

Firstly, the implementation status of ATFM measures is globally analyzed per FIR and visualized in Figure A.1 which shows global differences in implementation states of ATFM measures and the related ability of handling air traffic. On the one hand, central Africa and the southern Pacific are striking in particular which are large areas with no

¹ There is no upper limit of the airspace, cf. Mensen (2013) [68], page 512.

² SESAR: Single European Sky ATM Research, cf. DFS [8].

³ Cf. FAA [22].

⁴ Cf. Airservices Australia [4].

⁵ For pursuing information about ATFM measures, cf. ICAO (2009) [38] and ICAO (2014) [39].

⁶ Minutes- and mile-in-trail are ATFM measures for the purpose of separation, expressed as a number of minutes respectively miles between aircraft, cf. ICAO (2014) [39], Chapter 6.

form of ATFM measures implemented. This technological gap can presumably be traced back to low traffic volumes associated therewith (see Figure A.2). On the other, it can be extracted from Figure A.1 that Europe and North America show a widespread implementation of ATFM measures. For the classification of the global airspace it is assumed that FIRs belonging to the same governmental sovereign territory (such as the United States of America) implement ATFM measures simultaneously and to the same extent. This leads to the fusion of several FIRs of joint competences even if there are significant differences in ATFM status and air traffic volume. This is particularly illustrated by FIR Oakland Oceanic East and FIR Oakland Oceanic West comprising differences in the ATFM implementation status and traffic volume. However, due to their joint competence of Oakland they are merged to the same world region in here.¹

Secondly, ICAO air traffic volumes of 2010 are being analyzed to allow for a further global classification into preferably homogeneous world regions. Figure A.2 particularly shows three major air traffic agglomerations differing markedly from other areas. These are the economic metropolis of Europe, the United States of America (US) and China. In addition, Figure A.2 illustrates significant differences in air traffic volumes of continental FIRs compared to oceanic FIRs. Consequently, oceanic regions shall be regarded detachedly what makes the adherence to FIR boundaries not feasible in some parts of the global airspace. Those FIRs, primarily at the transition from continental to oceanic, have an excessive horizontal dimension across the associated coast line. In favor of the strived separation between continental and oceanic regions, the affected FIRs are cut at an appropriate location. These can be determined by comparing the course of FIR boundaries illustrated in Figure A.2 and the boundary lines of the world regions depicted in Figure 2.8 (affected areas are marked red). In total, 21 individual regions are defined, divided into 16 continental and 5 oceanic regions, whose spatial delineations primarily follow the methodology explained above.²

¹ ATFM implementation status of FIRs in 2014 are extracted from the ICAO GIS viewer, cf. ICAO [40].

² The classification of the global airspace is made in all conscience. However, it is very difficult or impossible to classify the global airspace by considering all relevant aspects. Consequently, there are other potential classifications of the global airspace differing from the world regions defined in here.

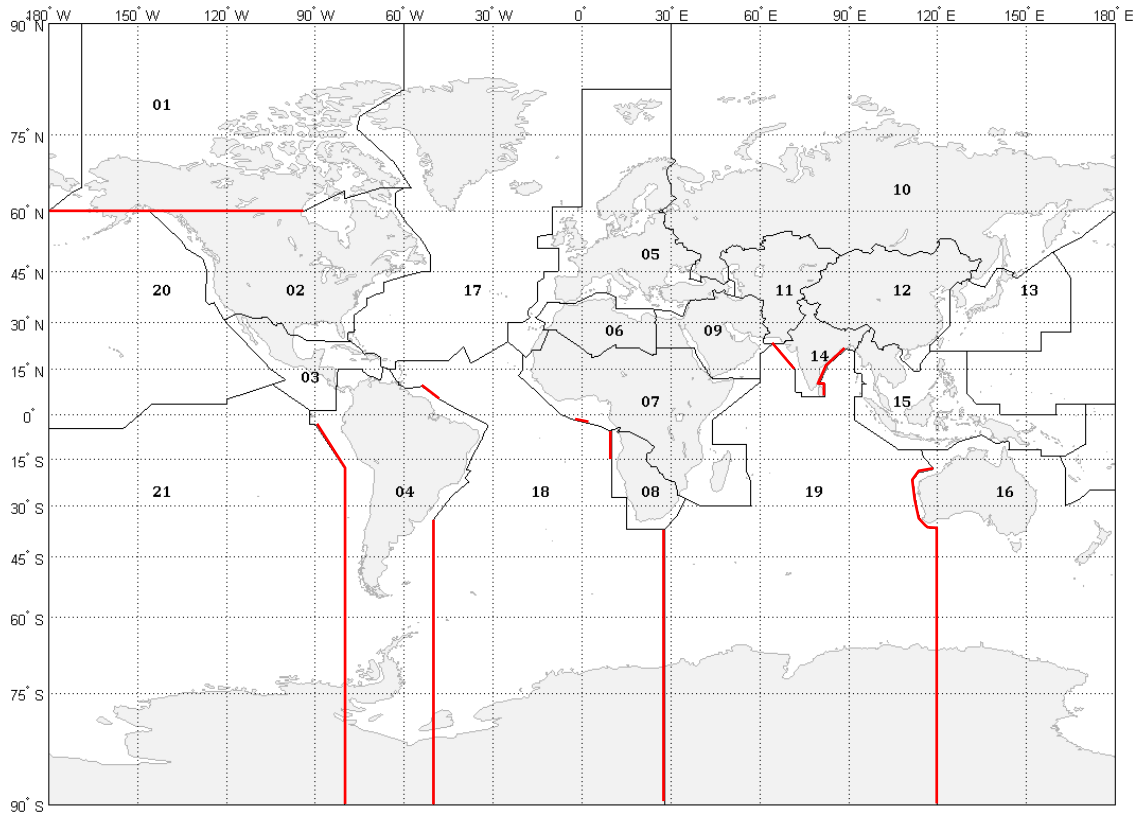


Figure 2.8: Boundaries of world regions

Region 01 – Northern Canada and Alaska

Air traffic volume within this region is assumed to differ from that in the US and the adjacent southern provinces of Canada (see Figure A.2).¹ FIR Anchorage Arctic, FIR Anchorage Continental (major part of the US state of Alaska) and FIR Edmonton (above 60° N, northern political provinces of Canada with Northwest Territories, Nunavut and Yukon) together form region 01.²

Region 02 – US and Southern Canada

The US has one of the highest traffic volumes in the world (see Figure A.2). Region 02 therefore consists of the US continental FIRs (with the exception of FIR Houston Oceanic) and the southern Canadian FIRs. Its northern boundary is defined by the southern part of FIR Edmonton up to 60° N, FIR Winnipeg and FIR Montreal and leads in a southerly direction along the Atlantic coast line, westward through the Gulf of Mexico

¹ Cf. ICAO [35], map 4.

² The southern boundary of 60° N is chosen to exclude the North Pacific track system, cf. ICAO [40].

(south of FIR Houston Oceanic and north of FIR Mexico) and in a northerly direction along the Pacific coast line back to 60° N.

Region 03 – Central America

Considering air traffic volume, FIR Mexico resembles the adjacent FIRs of the US, whereas the remaining FIRs (east of FIR Mexico) equal the FIRs of South America. With regard to ATFM status, only the minority of those FIRs entirely implemented measures yet what differentiates them from US FIRs. Weather also plays an important role within this corner of the world. Due to the warm gulf streams during the summer and fall months tropical revolving storms may develop.¹ However, ICAO already defined the upper airspace of Central America which is largely adopted.² With the exception of FIR Mazatlan Oceanic the following FIRs pertain to region 03: Central American, Curacao, Habana, Kingston, Mexico, Port Au Prince and Santo Domingo.

Region 04 – South America

The northern boundary of region 04 proceeds according to the South American airspace defined by ICAO.³ In the transition area, particularly with regard to traffic volume, the FIRs of South America are slightly different from the FIRs of Central America. Due to increased traffic volume around major aerodromes, ATFM measures are well implemented in those FIRs. There is a slope from north to south regarding ATFM implementation states showing degradation towards the south, except the former FIR Brasilia.⁴ In addition it should be noted that 4 of the 20 fastest growing aerodromes are located in the South American region. Above all, Belo Horizonte with 42.5 % traffic growth between 2010 and 2012.⁵ Due to the differentiation between continental and oceanic regions, South American FIRs are particularly affected. This leads to a longitudinal cut of the FIRs Lima, Antofagasta, Santiago, Puerto Mont, Punta Arenas, Piarco, Rochambeau, Montevideo, Ezeiza and Comodoro Rivadavia (see Figure 2.8).

¹ Cf. Hack (2008) [29].

² Cf. ICAO (2000) [37], chart ATS 5 (CAR W).

³ Cf. ICAO (2000) [37], chart ATS 5 (SAM N).

⁴ The former FIR Brasilia (defined in 2010) extends over the newly defined FIRs (defined in 2015) of Amazonica, Brasilia, Curitiba and Recife, cf. ICAO [40].

⁵ Cf. ICAO [35], map 3.

Region 05 – Europe

Europe has one of the highest air traffic volumes in the world (see Figure A.2) and due to the imminent implementation of a homogeneous airspace regarding ATM it is largely specified according to the Single European Sky (SES). It has the objective to improve the overall performance of ATM, to enhance current standards of air traffic safety and to contribute to the sustainable development of the ATS in Europe.¹ The border of region 05 is almost entirely adopted from SES. An exception is made towards east where the region is enlarged by the FIRs of the countries Armenia, Azerbaijan, Belarus, Georgia, Moldova, Turkey and Ukraine. With the complete implementation of SES, region 05 can be interpreted as a coherent airspace with homogeneous alterations concerning ATFM.

Region 06 – Northern Africa

Due to a different composition of air traffic (tourism, business) in the northern African region it is detached from Central Africa.² With the direct link of northern African cities (Algiers and Tripoli) to the intra-European route network it is assumed that the northern African countries will profit from the proximity to Europe.³

Region 07 – Central Africa

Central Africa is the largest coherent continental region where low traffic volume and the a of ATFM measures predominate (see Figures A.1 and A.2). Furthermore, the ITCZ may possibly develop severe thunderstorms entailing spacious weather-related diversions and consequent increased trajectory inefficiencies.⁴

Region 08 – Southern Africa

With regard to implementation states of ATFM measures, FIR Capetown, Johannesburg stand out against central African FIRs. In terms of air traffic volume these do not necessarily differ. When considering major air traffic flows between Europe and region 08, this is extended by the FIRs Gaborone, Windhoek and Luanda.⁵

¹ Cf. Eurocontrol (2013) [19], page 2.

² Cf. EASA 2010 [12].

³ Cf. African Aviation (1990) [1].

⁴ Cf. Hack (2008) [29].

⁵ Cf. ICAO [35], map 4.

Region 09 – Middle East

It is evident from Figure A.2 that there are significant differences in air traffic volume and implementation status of ATFM measures which makes it difficult to classify in accordance to the conventional methodology. However, for the purpose of air navigation planning and implementation, ICAO defined the Middle East Regional Group containing countries and consequent FIRs relevant for the classification in accordance to the status of ATFM measures.¹

Region 10 – Russia

While ATFM measures are almost entirely implemented, the air traffic volume of FIR Moscow is significantly higher compared to other Russian FIRs. These also differ from European, Chinese, Mongolian and Kazakhstani FIRs which leads to a definition according to the zonal centers of the Unified ATM system of the Russian Federation.²

Region 11 – Western Asia

With respect to the ATFM implementation status, western Asia arises through the difference to northern adjacent regions (05, 10 and 12). However, there is a large area within region 11 where no information about ATFM implementation states is available. Thus it is assumed that there are no ATFM measures implemented. Furthermore, region 11 is limited to the south by regions 09 and 14 which comprise higher air traffic volumes.

Region 12 – China and Mongolia

The Chinese FIRs and the Mongolian FIR Ulan Bator together form region 12. The majority of those FIRs has not yet implemented ATFM measures, except FIR Beijing and FIR Shanghai. Apart from that, China is a very strong economic and political force wherefore it is assumed that ATFM measures will be homogeneously implemented in future. While FIR Shanghai and FIR Guangzhou have very high air traffic volumes there is a large east-west-slope. Nevertheless, the western Chinese FIRs experienced very high air traffic growth rates between 2010 and 2012. Especially FIR Urumqi showed the world's highest air traffic growth which possibly flattens this slope.³

¹ Cf. ICAO [36].

² Cf. Main ATM Center [58].

³ Cf. ICAO [35], map 3.

Region 13 – Northeastern Asia

With respect to the implementation status of ATFM measures South Korea and Japan are detached from region 12 due to their higher technological level against adjacent FIRs (see Figure A.1). Except for FIR Pyongyang, all FIRs of region 13 have ATFM measures implemented. FIR Fukuoka comprises higher air traffic volumes than the adjacent FIRs. To allow for a consideration of traffic between Japan and China, region 13 is enlarged by FIR Incheon, FIR Pyongyang and FIR Taipei.

Region 14 – Southern Asia

Due to a very high density in population in India and the adjacent countries this region is considered separately.¹ The increasing population offers the potential of increasing air traffic demand and consequent increased air traffic volume.² According to traffic volume, region 14 differentiates from the Chinese FIR Kunming (region 12) with a significant lower number of flights in 2012 (see Figure A.2). Apart from that, the traffic volume of FIR Mumbai is considerably higher compared to the traffic volume of the FIRs of region 11 for the same period (see Figure A.2). Furthermore, large oceanic coverage entails the partition of affected FIRs. These are: FIR Mumbai, FIR Chennai, FIR Kolkata and FIR Colombo.

Region 15 – Southeastern Asia

The southeastern Asian region primarily considers the main traffic flows between Australia and Asia.³ Within this region, most FIRs have not yet implemented ATFM measures (see Figure A.1). Furthermore, air traffic within region 15 might be affected by adverse weather caused by the ITCZ.⁴ Furthermore, this region arises through the limitations to other regions and the differentiation between continental and oceanic regions.

Region 16 – Australia and New Zealand

FIR Auckland Oceanic, FIR New Zealand, FIR Brisbane and the eastern part of FIR Melbourne together form region 16. Taking the differentiation between continental and oceanic areas into account, the compliance with FIR boundaries is not entirely

¹ Cf. SEDAC [77].

² Cf. ICAO [35], map 3.

³ Cf. ICAO [35], map 4.

⁴ Cf. Hack (2008) [29].

possible here. This is particularly evident from Figure A.1 where FIR Melbourne comprises an excessive oceanic part wherefore being divided into two parts. These are split by means of the boundary of the upper airspace sectors of Australia.¹

As mentioned above, continental and oceanic territories are separately considered which is primarily traced back to low waypoint density and less domestic traffic. Due to the potential use of standard track systems (such as the North Atlantic Track system) the oceanic regions are separately considered in the following.²

Region 17 – North Atlantic

The North Atlantic airspace connects Europe and North America. It is the busiest oceanic airspace in the world where approximately 460.000 flights were recorded in 2012 which is also striking from Figure A.2. However, due to constraints of lateral separation and a limited number of economic flight levels the north Atlantic airspace is congested during peak hours. In order to provide the best service and to accommodate as many flights as possible, a system of organized tracks is constructed. Dependent on prevailing weather conditions, including the presence of jet streams, separate organized track systems are published daily.³

Region 18 – South Atlantic

The South Atlantic connects South America with Europe and Africa. While some FIRs have not yet implemented ATFM measures, other do with a decreasing tendency towards the south (see Figure A.1). Overall traffic volume above the South Atlantic differs from the North Atlantic which leads to a boundary determined by the southern limits of FIR Santa Maria Oceanic and FIR New York. Due to their large horizontal dimensions, some FIRs at the coastline of South America and Africa are split. The following South American FIRs are affected: FIR Comodoro Rivadavia, FIR Ezeiza and FIR Montevideo.⁴ FIR Accra, FIR Luanda and FIR Johannesburg Oceanic are split to separate the South Atlantic from Southern Africa and the Indian Ocean.

¹ Cf. Civil Aviation Safety Authority (2011) [7], page 10.

² Cf. ICAO (2015) [41].

³ Cf. ICAO (2015) [41] [41].

⁴ These FIRs are cut at 50° W to consider sufficient oceanic parts of the affected FIRs.

Region 19 – Indian Ocean

The majority of eligible FIRs possess large horizontal dimensions beyond the associated coastlines which make it difficult to clearly define the boundary of the Indian Ocean. However, with regard to the course of the coastline it is feasible to cut the following FIRs: FIR Mumbai, FIR Chennai, FIR Kolkata, FIR Colombo and FIR Melbourne to the east. Air traffic volume above the Indian Ocean is comparable with the air traffic volume above the South Atlantic.

Region 20 – North Pacific

The major part of region 20 is determined by FIR Oakland Oceanic East and West. The limitation against north at 60°N allows a separate consideration of the North Pacific track system which has a comparable structure to the North Atlantic track system. Herein, FIR Anchorage Oceanic and the southern part of FIR Anchorage Continental are included as well. However, as previously described, the major part of the North Pacific region is composed by FIR Oakland Oceanic East and West which underlie the responsibility of the US. To the east, region 20 is enlarged by FIR Mazatlan Oceanic defining the boundary to Central America (region 03).

Region 21 – South Pacific

Besides the lack of ATFM measures (see Figure A.1) it possesses a much lower air traffic volume than adjacent regions (see Figure A.2) what is possibly reducible to the large oceanic area. Apart from that, the most frequent route which passes through the South Pacific region connects Sidney and Los Angeles (in total 1800 flights in 2012).¹

The world regions defined above consider specific compositions with regard to traffic volume and technological progress (implementation status of ATFM measures). By applying region-dependent inefficiencies, potentially caused by the interaction of both compositions and the impact of airspace-related circumstances, this regionalization is dedicated to total trajectory inefficiency only and does not allow for a distinction of different flight phases. However, with regard to climate impact, significant portions of NO_x are primarily produced during high thrust settings (such as takeoff and climb). Due to additional ground track distance, caused by departure procedures, this

¹ Cf. ICAO [40].

is intensified within a specific area around the aerodrome. In this case, relative departure trajectory inefficiency is significantly higher than enroute trajectory inefficiency. The same applies to the approach, where certain procedures and traffic separations generate additional ground track distance. Consequently, there must be a more granular classification of the airspace respectively a fragmentation of the trajectory to consider relevant flight phases and their location.¹ To obtain this and to enhance the accuracy of future simulation results the trajectory is split into three flight phases: departure, enroute and arrival. For this purpose, the following chapter addresses the subdivision of the trajectory into these flight phases to subsequently apply differentiated trajectory inefficiencies.²

2.3.2 Microscopic classification

As already mentioned, trajectory inefficiency has different potential causes which can be related to different flight phases. Therefore, this chapter addresses the partitioning of the previously defined world regions into airspace divisions to allow a fragmentation of the trajectory into different flight phases. This has the benefit of more distinguished adjustments of altering ATFM performance and consequent changing trajectory inefficiencies. As shown in Figures 2.3 and 2.9, trajectory inefficiency alters in its course from takeoff until landing.³ Consequently, the trajectory is subdivided into three major flight phases: departure, enroute and arrival. After takeoff aircraft depart from the origin aerodrome and fly at a distance from the ideal trajectory on predefined standard instrument departures (SIDs) to ensure obstacle clearance, noise abatement and traffic separation. The second part of a flight, the enroute phase, comprises the entire part of a flight between the departure and arrival phase, primarily representing the cruise phase of a flight which subsequently merges into the final part of a flight trajectory represented by the approach phase. Here, aircraft fly standard instrument arrivals (STARs), follow vectors assigned by air traffic control (ATC) or enter holdings.⁴ Consequently, these flight phases underlie different inefficiencies

¹ Due to the compression of the extended trajectory, fuel consumption and consequent emissions are relocated into the aerodrome airspaces where actually arise. See Chapter .

² The classification of lateral airspace-related trajectory inefficiencies is detailed in Chapter 2.4

³ Cf. Kettunen et al. (2005) [54].

⁴ For detailed information concerning causes of lateral trajectory inefficiencies refer to Chapter 2.2.2.

what makes them relevant to be separately considered. However, there are different ways how to split the trajectory according to flight phases. Since lateral trajectory inefficiencies are considered in this Master Thesis, the flight phases are classified in a lateral manner. Due to differences between the departure and the arrival phase of a flight (such as engine settings) and to allow for a separate consideration of technological improvements (such as continuous descent), both are separately considered and described below.

Departure phase

The departure phase represents the part of the trajectory passing through the airspace closely associated with the departure aerodrome. It is assumed that, in average, flights depart in a star-shaped manner since destinations are usually equally spread around the origin aerodrome (see Figure 2.9). Consequently, the departure airspace is defined as a circular sector equally spaced around the origin aerodrome and considers trajectory inefficiencies primarily with respect to departure procedures. Due to geographical differences (for instance terrain or airport layout) the spatial delimitation of other airspaces (such as Terminal Maneuvering Areas) is not consistently defined and hence not applicable for a global consideration.

It is assumed that during departure the greater portion of trajectory inefficiencies are reducible to the adherence to SIDs performed within specific areas around the aerodrome (see Figure 2.9 left).¹ Hence, the airspace wherein departure procedures are performed is required. To determine the size respectively the radius of the departure airspaces a specific analysis of several SIDs is executed. For this, several German and international aerodromes with different locations and varying sizes (regarding the number of air traffic movements in 2012) are considered. Here, the GC-distance between the last point of the SIDs and the airport reference point is calculated.² In the calculation of average GC-distance five representative SIDs are selected per aerodrome. In total, 50 SIDs are analyzed whose results can be extracted from Table 2.1 showing a departure median radius of approximately 43.8 nm. For buffering purposes this is rounded up to 50 nm representing the termination of the departure phase.

¹ The fragmentation according to SIDs and STARs is the most intuitive way since directly corresponding to ATC procedures, cf. Kageyama (2010) [53].

² Coordinates are extracted from the corresponding Jeppesen Charts.

Arrival phase

The arrival phase of flights respectively STARs are normally initiated by means of overflying a specific fix point (enroute clearance limit)¹ at a certain altitude. Consequently, inefficiencies related to the arrival phase and caused by approach procedures theoretically occur beyond the enroute clearance limit. Therefore, the same proceeding as for the departure phase is applied to the arrival phase where the GC-distance between the enroute clearance limit and the aerodrome reference point is determined.² For the purpose of consistency, 50 representative STARs of the same airports are considered to calculate the average GC-distance between the enroute clearance limit and the aerodrome reference point. The results can be extracted from Table 2.1 showing an arrival median radius of 60.0 nm representing the initiation of the arrival phase.

Table 2.1: Results of the aerodrome airspace analysis ³

Aerodromes	Movements (2012)	Mean distance (SID)	Mean distance (STAR)
Hartsfield-Jackson Atlanta Intl. Airport ⁴	950119	39.0 nm	60.4 nm
Beijing Capital Intl. Airport ⁵	517584	64.7 nm	34.9 nm
Paris Charles De Gaulle Airport ⁶	499997	67.0 nm	88.7 nm
Frankfurt Airport ⁷	482242	58.8 nm	69.1 nm
Munich Airport ⁸	398039	46.4 nm	59.6 nm
Guarulhos Intl. Airport (Sao Paulo) ⁹	(284184)	43.1 nm	85.0 nm
Incheon Intl. Airport (Seoul) ¹⁰	254037	35.7 nm	60.6 nm
Dusseldorf Airport ¹¹	217219	43.8 nm	57.3 nm
Stuttgart Airport ¹²	131524	43.7 nm	50.8 nm
Hannover Airport ¹³	80139	35.6 nm	41.9 nm
Median		43.8 nm	60.0 nm

¹ This is typically the first point of the STAR within the approach chart.

² Refer to Chapter 2.2.2 to obtain more information about arrival-related inefficiencies.

³ GC-distances are calculated between coordinates obtained from airport charts, cf. Jeppesen [49], [46], [45], [47], [44], [52], [48], [43], [51] and [50].

⁴ Air traffic movements of Hartsfield-Jackson Atlanta Intl. Airport, cf. Airport Council International [3].

⁵ Air traffic movements of Beijing Capital Intl. Airport, cf. Airport Council International [3].

⁶ Air traffic movements of Paris Charles De Gaulle Airport, cf. Airport Council International [3].

⁷ Air traffic movements of Frankfurt Airport, cf. Fraport [23].

⁸ Air traffic movements of Munich Airport, cf. Munich Airport [69].

⁹ Air traffic movements of Guarulhos Intl. Airport in 2013 (no data for 2012), cf. GRU Airport [28].

¹⁰ Air traffic movements of Incheon Intl. Airport, cf. Incheon Airport [42].

¹¹ Air traffic movements of Dusseldorf Airport, cf. Dusseldorf Airport [11].

¹² Air traffic movements of Stuttgart Airport, cf. Fraport [23].

¹³ Air traffic movements of Hannover Airport, cf. Hannover Airport [30].

From Table 2.1 it is evident that there is no correlation between traffic movements and size of SIDs and STARs of the considered aerodromes. The results largely correspond with assumptions made in previous studies defining uniform radii of 50 nm for the departure and arrival airspaces.¹ However, arrival trajectory inefficiencies are typically more pronounced than departure trajectory inefficiencies. Not at least because of a larger area around the arrival aerodrome caused by traffic maneuvering due to STARs and radar vectoring. In contrast, while departing, aircraft fly on SIDs and are typically not affected by radar vectoring entailing a smaller maneuvering area around the departure aerodrome (see Figure 2.9). Against this background, and with regard to the analyzed SIDs and STARs, the radius of the departure airspace is parametrically set to 50 nm to allow for a certain buffer against the calculated radius (43.8 nm). The arrival airspace radius is parametrically set to the calculated radius of 60 nm. Both are a good tradeoff considering variations in SIDs and STARs. The application of the aerodrome airspaces is illustrated in Figure 2.9 showing good coverage for these departures and arrivals of real data trajectories from the IAGOS database.

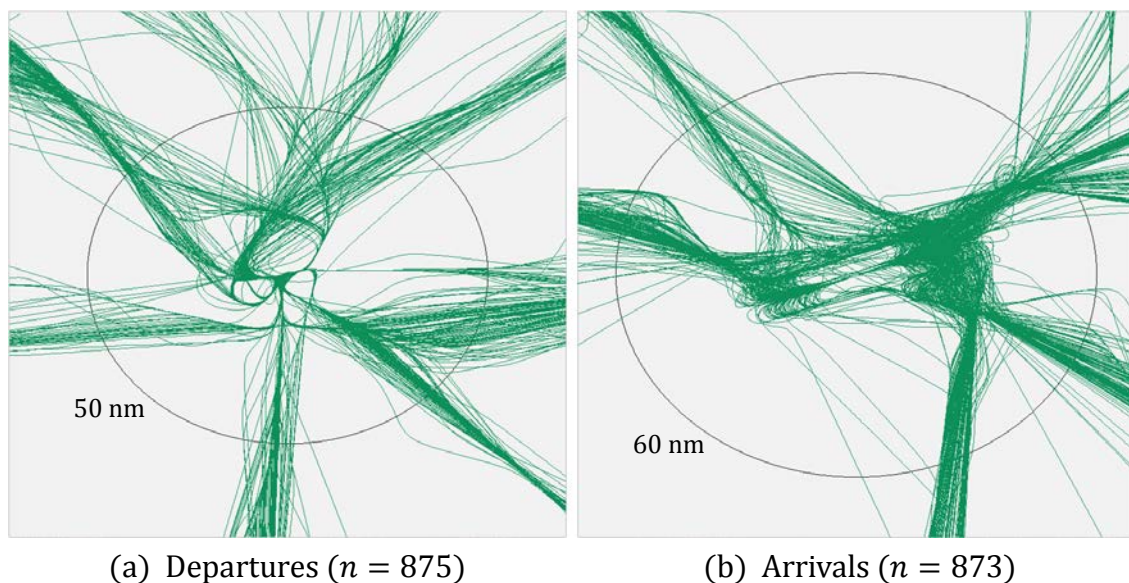


Figure 2.9: Departures and arrivals at Frankfurt International Airport (FRA)

Enroute phase

The enroute phase of a trajectory is located between the departure and arrival phase. It primarily represents the cruise phase of a flight and consequent lateral enroute

¹ Cf. Kettunen (2005) [54] and Reynolds (2008) [72].

trajectory inefficiencies. The enroute flight phase is subsequently further subdivided into a certain number of enroute fragments which comprise a specific quantity of trajectory inefficiency in accordance to the passed regions.

At this point, it is necessary to classify trajectory inefficiencies for each world region. The classification is made for the base year 2012 which is addressed by the following subchapter.

2.4 Classification of lateral trajectory inefficiencies

Figure 2.10 illustrates a representative transatlantic sample flight between Dusseldorf Airport (DUS) and Toronto Pearson Intl. Airport (YYZ). Outside the aerodrome airspaces the real trajectory runs approximately along the GC-trajectory but shows some deviations in places which may have different reasons.¹ To visualize trajectory inefficiency, Figures 2.10 and 2.11 are explained by means of the associated values. Reviewing the enroute section of the real data trajectory in Figure 2.10 the enroute trajectory inefficiency amounts to 2.3 %.

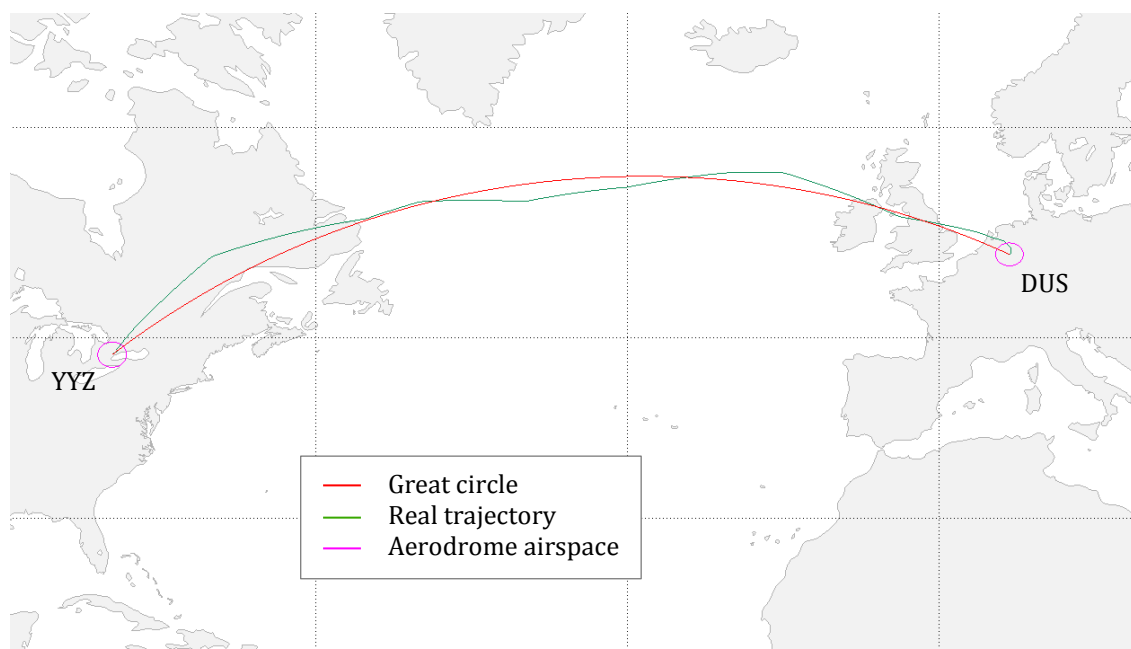


Figure 2.10: GC-trajectory and real data trajectory between DUS and YYZ

¹ For background information regarding lateral trajectory inefficiencies refer to Chapter 2.2.2.

Compared to enroute trajectory inefficiency the arrival and departure trajectory inefficiencies are significantly higher which is not at least the reason for the division of the trajectory into its flight phases. Trajectory inefficiency values associated with the sample flight from above amount to 14.9 % and 18.7 % for the departure respectively arrival phase. The latter is comparatively low and may be traced back to a combination of favorable wind conditions and a trajectory almost pointing towards the landing runway which becomes evident when considering Figure 2.11.

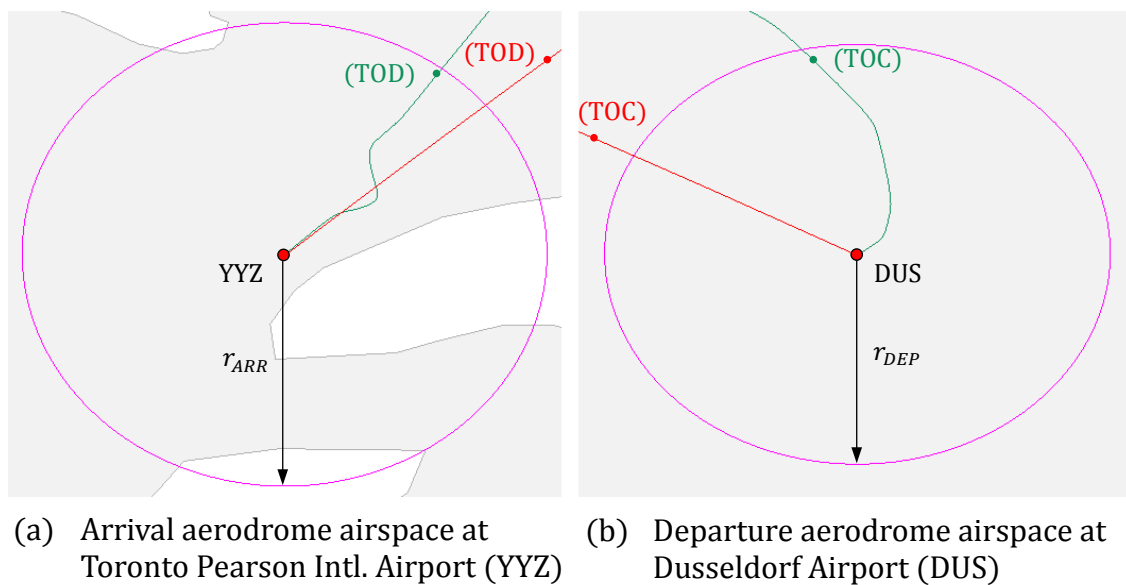


Figure 2.11: Departure and arrival flight phase ¹

To adequately assume trajectory inefficiencies of the underlying world regions², relevant literature is consulted yielding the majority of trajectory inefficiency values presented in Table 2.2.³ While there are numerous studies published related to trajectory inefficiency, most focus on enroute trajectory inefficiency.⁴ One of these studies additionally addresses departure and arrival trajectory inefficiency by analyzing departure and arrival routings of Dallas/Fort Worth International Airport. The results amount to 15.2 % for departure and to 25.2 % for arrival trajectory inefficiency.

¹ Background information on the used abbreviations: TOC (Top of Climb) designates the point of the profile where the climb phase terminates with a level off at cruising altitude. TOD (Top of Descent) designates the point where the cruising phase is terminated by the initiation of the descent.

² The world regions are defined in Chapter 2.3.1.

³ Cf. Eurocontrol (2013) [16], Eurocontrol (2014) [18], Reynolds (2014) [74].

⁴ Cf. Eurocontrol (2004) [14], Howell et al. (2003) [31], Kettunen et al. (2005) [54] and Reynolds (2014) [74].

These are uniformly applied on all regions considered for the inefficiency analysis of this specific study.¹ Against the uniform values of this study there are differences in departure and arrival trajectory efficiency between aerodromes. This is supported by the analysis of real data trajectories obtained from the IAGOS data base (see Figure A.5). However, based on this analysis there are no correlations between departure and arrival trajectory inefficiencies and regions.² Due to the current lack of correlations with regions, additional research is required. Therefore, the values from literature are also uniformly applied on the world regions defined for this Master Thesis. Table 2.2 shows trajectory inefficiencies by flight phase and region. Where no inefficiency values are found in literature, the mean value of the available trajectory inefficiencies is applied (4.4 %).

Table 2.2: Inefficiencies by region and segment for the AIRCAST base year 2012

Region	Departure-inefficiency	Enroute-inefficiency	Arrival-inefficiency
01	15.2 %	4.7 %	25.2 %
02	15.2 %	2.7 %	25.2 %
03	15.2 %	4.4 %	25.2 %
04	15.2 %	4.4 %	25.2 %
05	15.2 %	3.2 %	25.2 %
06	15.2 %	5.1 %	25.2 %
07	15.2 %	5.1 %	25.2 %
08	15.2 %	5.1 %	25.2 %
09	15.2 %	4.4 %	25.2 %
10	15.2 %	6.4 %	25.2 %
11	15.2 %	4.4 %	25.2 %
12	15.2 %	4.4 %	25.2 %
13	15.2 %	4.4 %	25.2 %
14	15.2 %	4.4 %	25.2 %
15	15.2 %	4.4 %	25.2 %
16	15.2 %	4.4 %	25.2 %
17	15.2 %	4.7 %	25.2 %
18	15.2 %	4.4 %	25.2 %
19	15.2 %	2.9 %	25.2 %
20	15.2 %	4.4 %	25.2 %
21	15.2 %	4.4 %	25.2 %

¹ Cf. Reynolds (2014) [74].

² The determination of IAGOS trajectory inefficiencies are explicitly described in Chapter 4.1.

Since the determined inefficiency values related to the analyzed real data trajectories refer to long range trajectories only, these are not applicable to the generic model considering all types of trajectories. With respect to enroute trajectory inefficiency, the values found in literature are occasionally stated as a percentage of total ground track extension wherefore the values need to be corrected for enroute trajectory inefficiency.¹ The affected values are related to regions 06, 07, 08, 10, 17 and 19 based on 50 nm radii for the departure and arrival airspace.² The values for regions 02 and 05 are gained from other sources which are related to a departure and arrival airspace radius of 40 nm respectively 100 nm.³ Regarding region 01, enroute trajectory inefficiency is assumed to be on level with region 17 since overflying traffic predominates.⁴ As mentioned above, the remaining regions obtain their trajectory inefficiency values by the mean value of the regions where data is provided. For the further use within the model the trajectory inefficiency values are provided by a certain structure illustrated in Figure 2.12. This is saved within an XML-file and extended for all world regions (21) and future time slices (2015 to 2050).⁵

```

1  <Data>
2    <Year uID="2012">
3      <Regions>
4        <Region uID="5">
5          <name>Europe</name>
6          <DepInefficiency unit="%">15.2</DepInefficiency>
7          <ArrInefficiency unit="%">25.2</ArrInefficiency>
8          <EnrInefficiency unit="%">3.2</EnrInefficiency>
9        </Region>
10       </Regions>
11     </Year>
12  </Data>

```

Figure 2.12: XML-structure of trajectory inefficiencies per time slice and region

¹ Total ground track extension represents total trajectory inefficiency including departure, enroute and arrival inefficiencies. To obtain enroute trajectory inefficiency only, departure and arrival trajectory inefficiencies are deducted from total trajectory inefficiency.

² For background information concerning trajectory inefficiency values of these regions, cf. Reynolds (2014) [74].

³ For the value of region 02, cf. Eurocontrol (2014) [16]. For the value of region 05, cf. Eurocontrol (2014) [18].

⁴ Cf. ICAO [35], map 4.

⁵ The processing of trajectory inefficiency values within the model is detailed in Chapter 3.4.1.

Assuming a zero-improvement/-worsening scenario, trajectory inefficiencies are kept constant for future time slices presuming no ATFM efficiency enhancement or deterioration over time. With regard to trajectory inefficiency, research is required in terms of prospective studies considering more detailed information of global trajectory inefficiencies by analyzing global mixed trajectories (short, medium and long haul) and their potential development over time.

3 Modeling trajectory inefficiencies

This chapter addresses the development of a generic¹ model designed with Matlab, to enable the consideration of airspace-related trajectory inefficiencies in simulations executed with the TCM and contributes to the improvement of trajectory calculations and consequent simulation results. However, before getting down to the heart of this subject, the determination of different important parameters such as trajectory coordinates, distance and azimuth are explained serving as the basis for further calculations (see Chapter 3.1). In the following to that, a detailed description of the model is provided whose sequence is structured into three functional blocks (Figure 3.1).

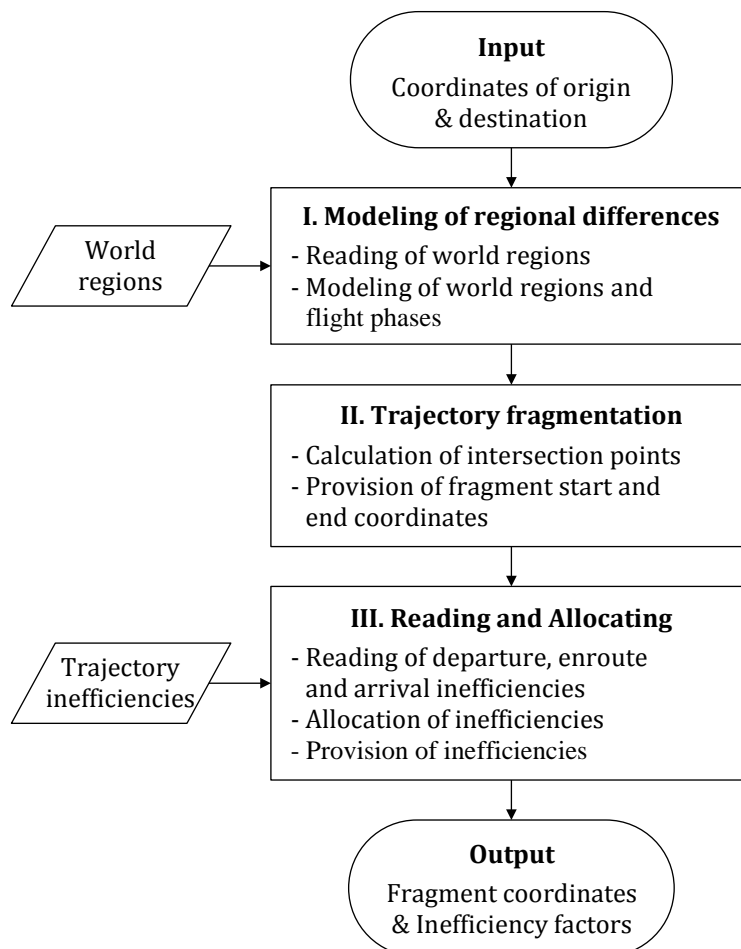


Figure 3.1: Functional diagram of the model

¹ The model is of a generic type to enable the ability of arbitrary air traffic scenarios.

In a first step (Figure 3.1, Block I.), the previously defined world regions are read in and modeled by means of polygons to allow a global gradation of airspace-related trajectory inefficiency differences.¹ In the following to that, the aerodrome airspaces are defined in terms of small circles around the trajectory's origin and destination aerodromes to allow for a distinction between trajectory inefficiencies related to different flight phases (see Chapter 3.2). Afterwards (Figure 3.1, Block II.), the intersection points between trajectory and regions are calculated (see Chapter 3.3). The resulting region-related trajectory fragments are further used in order to read in the respective inefficiency factors of the affected regions (Figure 3.1, Block III.). Finally, the output of the model and the further data processing within the simulation are explained (see Chapter 3.4).

It should be noted, that most of the implemented Matlab functions are provided by the Mapping Toolbox only. Consequently, these can solely be applied once the Mapping Toolbox is available.² The preferred latitude and longitude values of origin and destination are between $\pm 90^\circ$ respectively $\pm 180^\circ$.³

3.1 Important trajectory parameters

During the further course of Chapter 3 some equations regarding GC-calculations are frequently applied which shall be briefly explained in the following.

Discretization of the GC-trajectory

Initially, it is necessary to define the GC-trajectory for later applications. In this context the Matlab function `track2` calculates latitude φ_n and longitude λ_n values between a start point (φ_i, λ_i) and an end point $(\varphi_{i+1}, \lambda_{i+1})$.⁴ The discretization can be parametrically adjusted by stating the trajectory's number of discrete points n . This is described by means of Equation (3.1).⁵

¹ The world regions are defined in Chapter 2.3.1.

² The Mapping Toolbox is extensively described in Mathworks [62].

³ The input of longitude values in the form of 0° to 360° is also possible.

⁴ The documentation of the Matlab function `track2` can be found on the homepage of Mathworks, cf. Mathworks [66].

⁵ The number of discrete points along the trajectory is parametrically set to $s_{AB}/10 \text{ nm}$ (rounded up to the next integer).

$$(\overrightarrow{\varphi_n}, \overrightarrow{\lambda_n}) = \text{track2}(\varphi_i, \lambda_i, \varphi_{i+1}, \lambda_{i+1}, n) \quad (3.1)$$

Distance and azimuth

The Matlab function `distance` calculates the distance s and azimuth α of a GC-trajectory between two points on the earth's surface.¹ It is a function of latitude φ_A and longitude λ_A of a start point and an end point (φ_B, λ_B) .

$$(s_{AB}, \alpha) = \text{distance}(\varphi_A, \lambda_A, \varphi_B, \lambda_B) \quad (3.2)$$

In subsequent chapters Equation (3.2) is used whenever an individual fragment length between two consecutive intersection points is to be calculated. The correlation is visualized by Figure 3.2 which schematically illustrates a GC-trajectory between two arbitrary points A and B at the northern hemisphere.

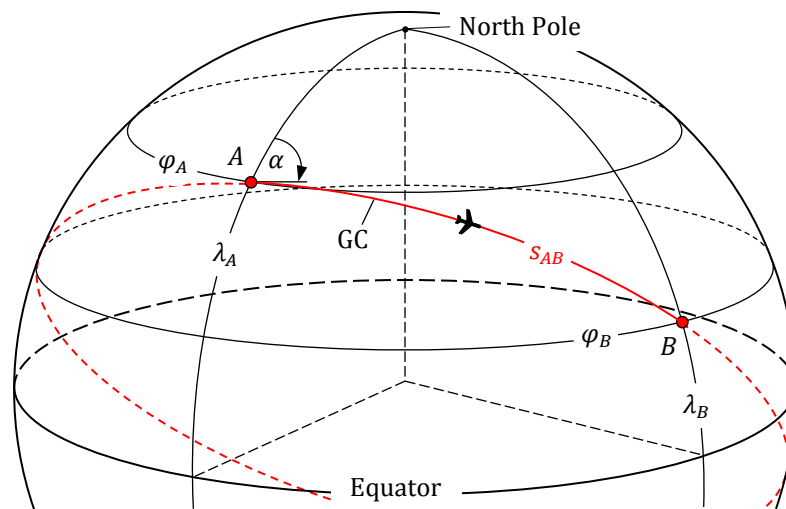


Figure 3.2: GC-trajectory at the northern hemisphere

GC-trajectories passing the anti-meridian

At the anti-meridian ($\lambda = \pm 180^\circ$) the trajectory does not proceed in a conventional manner. As soon as the trajectory reaches the anti-meridian it sweeps around the longitudes (approximately at crossing latitude) and connects the last point of the trajectory before and the first point beyond the anti-meridian. Due to its discretization

¹ The documentation of the Matlab function `distance` can be found on the homepage of Mathworks, cf. Mathworks [60].

the GC-trajectory does therefore not necessarily meet the anti-meridian (see Figure 3.3 (a)). Consequently, there is no intersection point X calculated, even though a polygon would run along the anti-meridian.¹ Unfortunately, the generated connection line generates intersection points with other, normally not affected regions R .

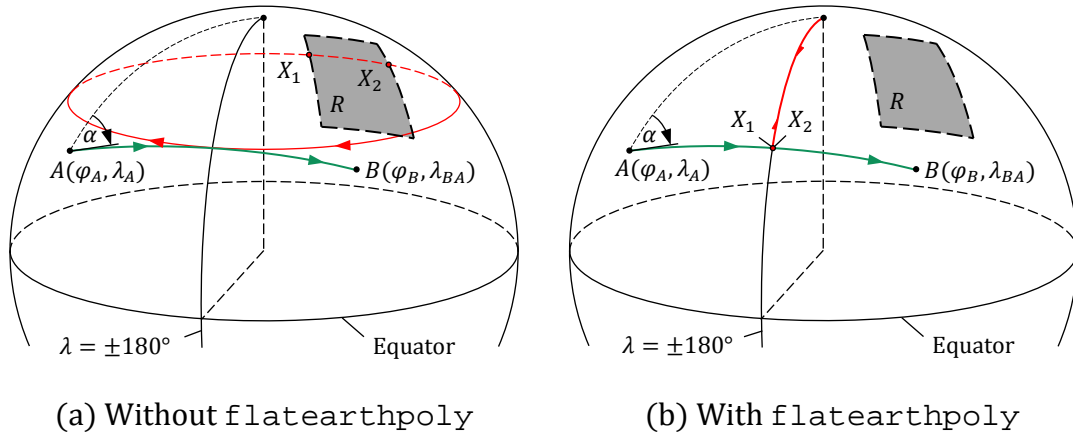


Figure 3.3: GC-trajectory crossing the anti-meridian

This is bypassed by the Matlab function `flatearthpoly` which inserts additional points at the anti-meridian ($\lambda = \pm 180^\circ$) and the nearest pole (see Figure 3.3 (b)).² Furthermore, there is the possibility of an exceptional case, where both, the longitudes of origin λ_A and destination λ_B are located on the anti-meridian. Thus the trajectory runs along the anti-meridian entailing a negative impact on following calculations. Consequently, the absolute values of the longitudes are shifted westward by 0.01° when the condition ($|\lambda_A| = |\lambda_B| = 180^\circ$) is true.³ This value proves as low as possible but as large as necessary having no significant influence on further calculations. The maximum error made is 0.6 nm at the equator declining towards the poles.

¹ The modeling of polygons is detailed in Chapter 3.2.1.

² Cf. Mathworks [61].

³ The latitudes are not changed.

3.2 Modeling regions and flight phases

In accordance to Figure 3.1 (Block I), the modeling of world regions (see Chapter 3.2.1) and flight phases (see Chapter 3.2.2) is explained in the following to allow for a distinction of trajectory inefficiency variations.¹

3.2.1 Macroscopic modeling

As already explained in Chapter 2.3.1, the delimitations of the world regions are defined in accordance with the peripheral boundaries of the considered FIRs. The geographical coordinates of the FIRs are entered in form of vectors to define closed polygons. For this purpose, each region is defined by two vectors, one containing latitude-values and the other containing longitude-values. In general, latitude and longitude values are directly extracted from the ICAO FIR viewer. Where this is not possible, the coordinates are gathered using the position function of the measurement toolbox of the ICAO FIR viewer.² It is evident that in Equations (3.3) and (3.4) the number of vector elements i depends on the number of extracted points defining each polygon n .

$$\overrightarrow{\varphi}_n = (\varphi_1; \varphi_2; \dots \varphi_i) \quad (3.3)$$

$$\overrightarrow{\lambda}_n = (\lambda_1; \lambda_2; \dots \lambda_i) \quad (3.4)$$

The polygons are defined within a separate Matlab .m-file and subsequently read in by the model at the beginning of the program sequence.³

Polygons crossing the anti-meridian

However, there are polygons crossing the anti-meridian due to their predefined geographical delimitations.⁴ Figure 3.4 (a) schematically illustrates the case of a change in sign of longitudes (from $+180^\circ$ to -180° and vice versa). Here the polygon meets the anti-meridian (X_1), sweeps across the longitudes (approximately at crossing latitude) to the other side of the anti-meridian (X_2) from where it regularly continues via C_2 and C_3 until it meets the anti-meridian again (X_3). Here, the procedure starts to-

¹ The definition of regions and aerodrome airspaces can be found in Chapter 2.3.

² For more FIR related information, cf. ICAO [40].

³ The data provision is detailed in Chapter 3.4.1.

⁴ Region 10, 20 and 21 are affected (see Figure 2.8).

wards the other direction until the polygon's initial point C_1 . Consequently, the affected polygons are closed on the wrong side which results in problems for their further application (see Chapter 3.3.1).

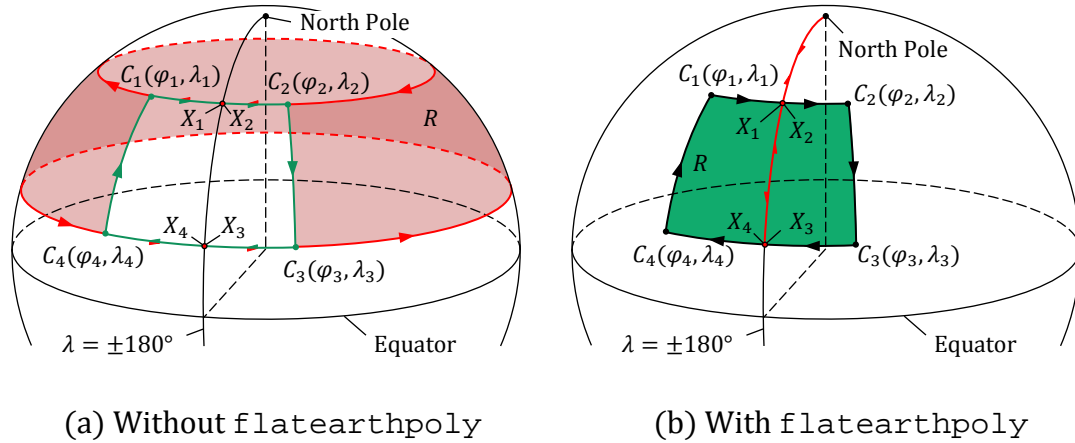


Figure 3.4: Simplified illustration of the Matlab-function flatearthpoly

This is bypassed by the Matlab-function flatearthpoly which is applied on the affected polygons and schematically illustrated in Figure 3.4 (b).¹ Against the initial course of the polygon it now reaches the anti-meridian (X_1), drops to the nearest pole, sweeps across the longitudes at the pole and follows the anti-meridian to the other side of the crossing (X_2) from where it regularly continues. The same procedure is conversely applied on the returning polygon when reaching the anti-meridian again (X_3 – pole – X_4). Consequently, the Matlab-function flatearthpoly correctly closes the polygon. However, this erroneously creates an imaginary region boundary at the anti-meridian entailing side effects during the calculation of intersections with the trajectory. This problem is bypassed with the help of querying latitude values of the intersections at the anti-meridian according to Equation (3.8).²

3.2.2 Microscopic modeling

To enable the consideration of trajectory inefficiencies, related to departure and arrival phases, it is necessary to model the corresponding flight phases by means of air-

¹ The documentation of the Matlab function flatearthpoly can be found on the homepage of Mathworks, cf. Mathworks [61].

² For the elimination of erroneous intersection points refer to Chapter 3.3.2.

spaces around the aerodromes. As already mentioned, the aerodrome airspaces are defined as circular sectors around the aerodromes modeled by small circles.¹ They are applied by means of the Matlab function `scircle1` which calculates latitudes and longitudes of the small circle $(\varphi_{SC}, \lambda_{SC})$ by considering the values of latitude φ_{CP} and longitude λ_{CP} of its center point (coordinates of origin and destination) and the parametrically defined radii allowing for later adjustments.² By default the radius r is set to 50 nm for the origin aerodrome respectively 60 nm for the destination aerodrome.³ Equation (3.5) shows the functional correlation.

$$(\overline{\varphi_{SC}}, \overline{\lambda_{SC}}) = \text{scircle1}(\varphi_{CP}, \lambda_{CP}, r) \quad (3.5)$$

3.3 Fragmentation of the GC-trajectory

This subchapter deals with the calculation of intersection point coordinates of the GC-trajectory with polygons and small circles to fragment the GC-trajectory.

3.3.1 Intersection points with polygons and small circles

Firstly, the length of the GC-trajectory is calculated and tested for a certain distance condition. If the GC-distance between origin and destination is less than 110 nm consequently no intersection points with the polygons are calculated.⁴ In this case, there is no enroute flight phase identified whereby the aerodrome airspaces overlap to some extent so that a clear distinction between departure and arrival is hardly possible. Therefore the radius weighted mean trajectory inefficiency is calculated according to Equation (3.6) considering both airspace radii (r_{DEP} and r_{ARR}) as well as both trajectory inefficiencies (I_{DEP} and I_{ARR}).

$$I(S_{AB} < 110 \text{ nm}) = \frac{(I_{DEP} \cdot r_{DEP} + I_{ARR} \cdot r_{ARR})}{(r_{DEP} + r_{ARR})} \quad (3.6)$$

¹ A small circle is generally defined as the intersection of the sphere's surface with a plane not passing through the center of this sphere. Hence, all latitudes are small circles (except the equator). Mathematically small circles are defined by distance from a center point, cf. Mathworks [62].

² The documentation of the Matlab function `scircle1` can be found on the homepage of Mathworks, cf. Mathworks [65].

³ The determination of the radii is defined in Chapter 2.3.2.

⁴ The sum of both aerodrome airspace radii results in 110 nm.

Thus, the model output for flights shorter than 110 nm comes to the coordinates of origin and destination as well as the mean inefficiency value.¹

In a next step (trajectories longer than 110 nm), the trajectory is divided into the flight phases; departure, enroute and arrival. This is done by determining the intersection points between the GC-trajectory and the small circles. The latitude $\varphi_{X,SC}$ and longitude $\lambda_{X,SC}$ of the intersection points at the small circles are calculated by means of the Matlab-function `reckon`.² It is a function of distance s on a specific azimuth α from a center point, here with the latitude φ_A and longitude λ_A . The intersection points are calculated in accordance to Equation (3.7) and illustrated in Figure 3.6.

$$(\varphi_{X,SC}, \lambda_{X,SC}) = \text{reckon}(\varphi_A, \lambda_A, r, \alpha) \quad (3.7)$$

For the calculation of intersection points X_{SC} with the small circle at the origin A this function is applied with the departure radius ($r = r_{DEP}$). The intersection point with the small circle at the destination is calculated again by generating a small circle around the origin A with the radius ($r = s_{AB} - r_{ARR}$). The herewith calculated points are further used as enroute starting and ending point dividing the GC-trajectory into the three flight phases.

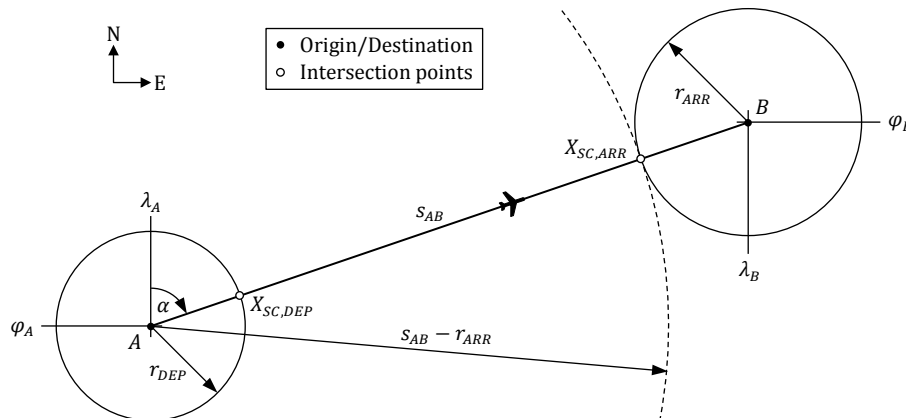


Figure 3.5: Modeling the transition of flight phases

¹ Refer to Chapter 3.4.1 to obtain more information about data provision.

² The documentation of the Matlab function `reckon` can be found on the homepage of Mathworks, cf. Mathworks [64].

In order to calculate intersection points with the polygons to consider regional differences of trajectory inefficiency and their consequent application on the GC-trajectory, only the enroute trajectory is considered.¹ The major advantage of this approach is to exclude potential intersection points within the small circles. This becomes relevant if the distance between the trajectory's starting or ending point and the potential intersection point with the polygon is less than the radius of the associated small circle (Figure 3.6).

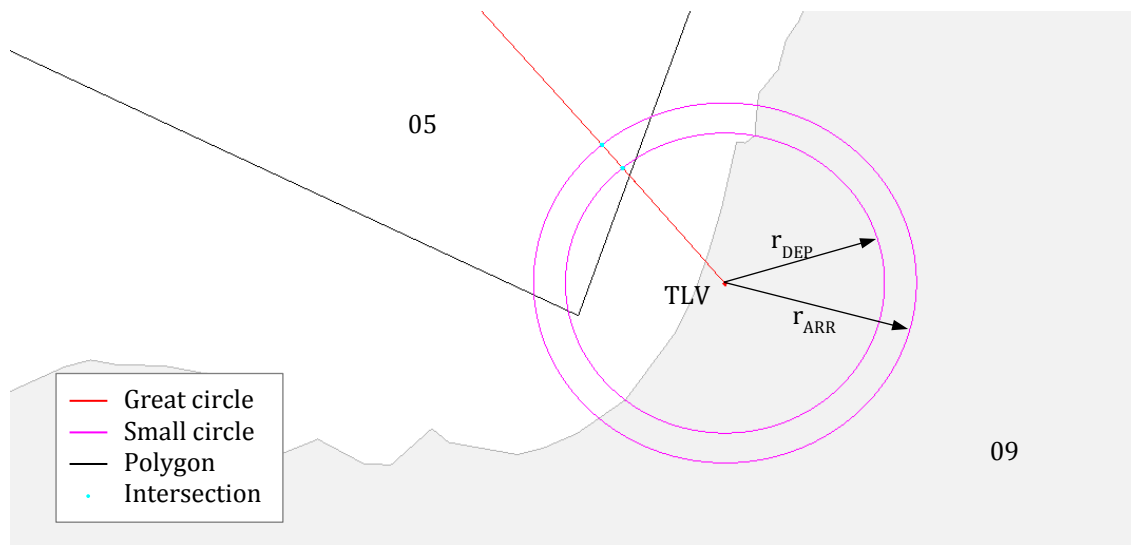


Figure 3.6: Intersection points of transregional small circles

To subsequently subdivide the GC-trajectory in accordance to the passed regions, its intersection points with the polygons are calculated with the help of the Matlab function `polyxpoly`² by checking each polygon for at least one common intersection point with the GC-trajectory.³ The calculated intersection points with small circles and polygons as well as the coordinates of origin and destination are joined into one common matrix. This, however, may include erroneously calculated intersection points caused by side effects from the calculations described in here. Consequently, erroneous intersection points are to be eliminated to ensure a proper depiction of common trajectories on a global scale especially with regard to the fragmentation.⁴

¹ For the application of trajectory inefficiencies refer to Chapter 3.4.1.

² It should be noted that `polyxpoly` returns the intersection points in a planar Cartesian system generating a very small and therefore negligible error at the projection, cf. Mathworks [63].

³ The documentation of the Matlab function `polyxpoly` can be found on the homepage of Mathworks, cf. Mathworks [63]. It returns a matrix including all enroute intersection points with the polygons.

⁴ The elimination of erroneous intersection points is detailed in Chapter 3.3.2.

In the following, the fragmentation of the trajectory is illustrated by means of a sample flight between DUS and YYZ visualized in Figure 3.7. The aerodrome airspaces (magenta circles) as well as the intersection points generated by the GC-trajectory (red line) and the polygons (black line) are clearly evident.



Figure 3.7: Fragmented GC-trajectory between DUS and YYZ

In total, this sample flight comprises five trajectory fragments. While the first fragment represents the departure phase, the last represents the arrival phase. Their intersection points with the GC-trajectory are defined by the radii of the aerodrome airspaces (50 and 60 nm). Furthermore, there are three enroute fragments complying with the regions 05, 17 and 02. The associated fragment entry- and exit-coordinates are to be found in Table 3.1.

Table 3.1: Fragment coordinates for the flight between DUS and YYZ

Fragment	Type	Region	Entry-coordinates	Exit-coordinates
1	Departure	5	51.2894 N, 6.7667 E	51.6752 N, 5.5830 E
2	Enroute	5	51.6752 N, 5.5830 E	55.3647 N, 10.0000 W
3	Enroute	17	55.3647 N, 10.0000 W	53.7670 N, 54.9587 W
4	Enroute	2	53.7670 N, 54.9587 W	44.3270 N, 78.5911 W
5	Arrival	2	44.3270 N, 78.5911 W	43.6766 N, 79.6306 W

With the help of the calculated intersection points the model is able to determine the length of each fragment by means of Equation (3.2). By applying trajectory inefficiencies (see Table 2.2 and Table 3.2) on the associated fragments the ground track extension is calculated but not provided for the TCM since independently calculated within the simulation.¹

However, there is the possibility of intersection points being erroneously calculated whose elimination is detailed in the following subchapter.

3.3.2 Elimination of erroneous intersection points

To detect and eliminate erroneously calculated intersection points several solutions are applied for each individual case described below.

Multiple intersection points

Adjacent polygons are defined by the same coordinates at their joint delimitation. Because each polygon is separately checked for intersection points with the GC-trajectory there are always two intersection points calculated, one for each adjacent polygons. To eliminate one of the double values all intersection points are sorted within a matrix and compared row by row. If two consecutive elements are identical (within a certain tolerance) the second will be deleted.

Erroneous intersection points at the anti-meridian

There is a potential source of error when both, origin and destination are located on the anti-meridian ($|\lambda_A| = |\lambda_B| = 180^\circ$) generating unexpected erroneous intersection points along the anti-meridian. In this theoretical case the absolute longitudes are subtracted by 0.01° to shift the entire trajectory westward by 0.01° .² The maximum shifting error amounts to 0.6 nm at the equator and decreases towards the poles.

By dropping to the nearest pole the Matlab function `flatearthpoly` generates erroneous intersection points with the polygons along the anti-meridian (see intersection points X_2 and X_5 in Figure 3.8). These are filtered out by specifying a condition

¹ To obtain information concerning the simulation with the TCM refer to Chapter 3.4.2.

² G. Konieczny (personal communication, October 20, 2015).

regarding the calculated intersection points and the arrangement of the regions at the anti-meridian. The following expression mathematically describes the condition.

$$\exists X(\varphi, \lambda): (|\lambda| = 180^\circ) \wedge ((-5^\circ < \varphi < 3.5^\circ) \vee (\varphi < -25^\circ)) \quad (3.8)$$

As soon as the absolute longitude $|\lambda|$ of the intersection points X is equal to 180° (anti-meridian) and the latitude φ of the intersection points lies either between -5° and 3.5° or is smaller than -25° the checked intersection point is correctly calculated. In all other cases at the anti-meridian the intersection points are deleted. The latitude values describing the condition above represent the course of the regions at the anti-meridian (see Figure 2.8). Furthermore, the Matlab function `flatearthpoly` generates erroneous intersection points by sweeping around the longitudes at the poles. These are eliminated by means of the following method.

Erroneous intersection points at the poles

Erroneously calculated intersection points at the poles are detected by means of a comparison of the azimuths which is schematically illustrated in Figure 3.8. For this purpose, the azimuth values α_X are calculated from the origin A to all intersection points by means of Equation (3.2). In a next step, each azimuth value is compared with the actual azimuth α of the GC-trajectory.

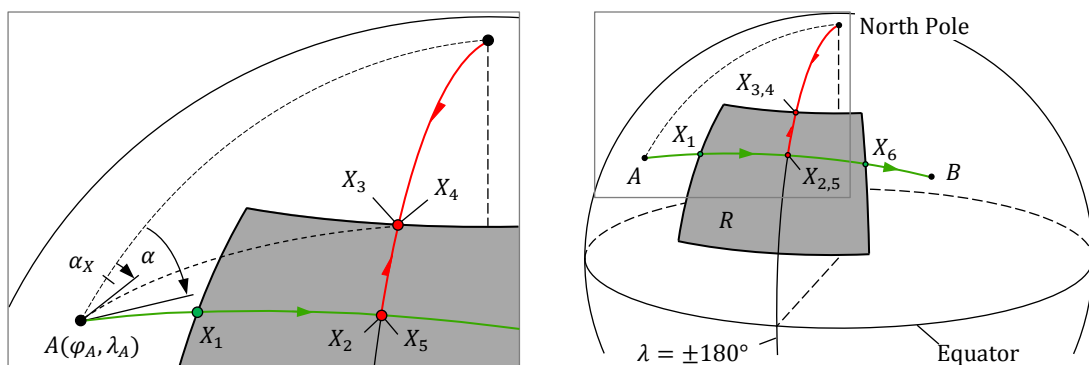


Figure 3.8: Azimuth query of potential erroneous intersection points

The intersection point X is correctly calculated and located on the trajectory if the absolute azimuth difference is smaller than the tolerance ε and if the absolute value of the latitude $|\varphi|$ is not equal to 90° .¹

$$\exists X(\varphi, \lambda): (|\alpha - \alpha_X| < \varepsilon) \wedge (|\varphi| \neq 90^\circ) \quad (3.9)$$

However, the performance of the model is limited by an exceptional case which also entails the calculation of erroneous intersection points. Consequently, the associated regions and their inefficiencies are erroneously allocated. This constraint is detailed in the following subchapter.

3.3.3 Limitation to the model

Due to the infinite multitude of trajectory courses as well as side effects accompanying the handling of special cases (see Chapter 3.3.2), the elimination of all exceptions is not entirely feasible. While all known exceptional cases containing errors are eliminated, there is one case identified which is not patched and therefore briefly explained.

As soon as origin and destination are located on opposite longitudes the trajectory proceeds across the poles ($|\lambda_A| + |\lambda_B| = 180^\circ$). In this process, there is the chance of intersection points being not at all or incorrectly calculated entailing regions being assigned to wrong trajectory fragments resulting in wrong allocations of inefficiencies. This does not stop program sequence but generates errors within the functional chain so that the results of this special case are unusable for further simulations with the TCM. However, it is assumed that such theoretical cases do not necessarily occur in reality, wherefore the consideration of this special case is abstained.

This exceptional is illustrated by means of a real flight being one of the longest direct flights flown.² The flight from DXB (Dubai International Airport) to SFO (San Francisco International Airport) is assumed to be critical regarding the arrangement of origin and departure longitudes.³ Figure 3.9 shows the course of the GC-trajectory

¹ The tolerance ε is parametrically set to $\varepsilon = 10^{-2}$.

² Cf. Die Welt [9].

³ The difference in longitudes for the flight from DXB to SFO amounts to: $|\lambda_A| + |\lambda_B| = 177.7393^\circ$.

and the correctly calculated intersection points. Consequently, fragment inefficiencies are properly assigned.

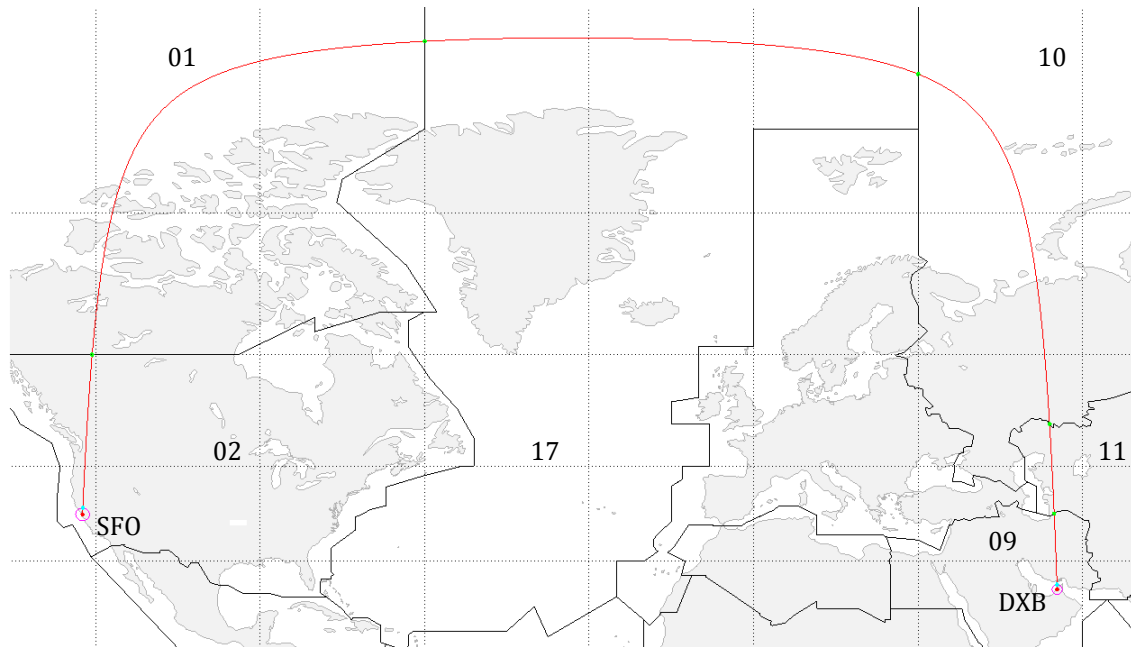


Figure 3.9: Longitude-critical trajectory (DXB - SFO)

Besides the flight from DXB to SFO there are other very long direct flights (such as SYD-DFW)¹. Due to a larger difference between origin and destination latitudes their longitudes are less critical. In addition, there is the possibility of opposite aerodromes being located closer to the poles reducing overall flight distance. However, it is assumed that passenger demand, regarding direct connections across the pole, decreases with population density towards the poles.² To completely exclude the event of two opposing aerodromes, the city coordinates of all AIRCAST cities with regard to connections among themselves need to be analyzed in prospective studies.

After the development of the model and the elimination of critical factors leading to erroneous intersection points, the following subchapter deals with the data provision as well as the further processing within simulations executed with the TCM.

¹ SYD: Kingsford Smith International Airport Sydney; DFW: Denver/Fort Worth International Airport.

² For population information cf. SEDAC [77].

3.4 Data processing and TCM simulation

After the completion of the model, this chapter addresses the data output and the further processing within the simulation of trajectories.

3.4.1 Data provision for the TCM simulation

For the simulation of inefficient trajectories, the TCM requires specific data provided by the model. This includes entry and exit coordinates of each trajectory fragment as well as its trajectory inefficiency factors. The latter are saved to an .xml-file¹ and obtained by applying the open-source function `xml2struct` to read the inefficiency values of the involved regions into the model where transformed from a percentage into an inefficiency factor I and provided for the simulation.² The fragment entry and exit coordinates are saved together with the inefficiency factors as Matlab .mat-file which constitutes the interface between the model and the TCM.³ When loading the .mat-file, a struct-variable with the name *Trajectory* is transferred into the Matlab workspace. Table 3.3 illustrates the output structure of the model by means of the introduced sample flight from DUS to YYZ.

Table 3.2: Output of the model for a sample flight between DUS and YYZ

Trajectory.SegCoordinates				Trajectory.SegInefficiency
(Entry-coordinates)		(Exit-coordinates)		(Inefficiency factor I)
51.2894 N	6.7667 E	51.6752 N	5.5830 E	1.152
51.6752 N	5.5830 E	55.3647 N	10.0000 W	1.032
55.3647 N	10.0000 W	53.7670 N	54.9587 W	1.047
53.7670 N	54.9587 W	44.3270 N	78.5911 W	1.027
44.3270 N	78.5911 W	43.6766 N	79.6306 W	1.252

3.4.2 Simulation with TCM

In the following, with regard to trajectory inefficiency, the calculation of trajectories by the TCM shall be explained.

¹ The .xml-file structure is illustrated in Chapter 2.4.

² The inefficiency data is imported by using the open-source function `xml2struct` available at the file exchange, cf. Mathworks [67].

³ The fragment entry and exit coordinates are calculated according to Chapter 3.3.

The program sequence of the Matlab based TCM is roughly divided into four functional blocks. Within the first main block a vertical target flight profile is generated in accordance to user defaults and the lateral trajectory. Subsequently, block two and three comprise the lateral respectively vertical navigation (such as potential turns and changes of flight phases). The fourth main block contains the flight performance calculation where the control of the aircraft movement as well as the evaluation of the engine and aerodynamic model is executed. Based on this information, the flight condition of the following time increment is determined by a numeric integration of the flight conditions over time which is, in turn, the starting point of the next run. This simulation loop is executed as long as the complete trajectory is simulated to then save the simulation results to a Matlab .mat-file.¹

The trajectory is simulated assuming equal atmospheric conditions based on the International Standard Atmosphere (ISA)² and a standard flight profile³ with constant cruise Mach number ($Ma = 0.82$) and a constant altitude (FL380)⁴. For the calculation of take-off mass a seat load factor of 85 % and 5 % contingency fuel are assumed.⁵ To obtain realistic and aircraft related simulation results, the aircraft performance data of the Airbus A340-313 is provided by BADA 4.0 (yields burned fuel, H₂O and CO₂).⁶ Non CO₂-emissions are determined by applying the Boeing Fuel Flow Method 2 (yields produced NO_x).⁷

In the following, the procedure of applying trajectory inefficiencies on the GC-trajectory is explained. For this purpose, the inefficient trajectory is simulated by extending the trajectory fragments by their associated inefficiency factors. In a next step, the extended trajectory is compressed and relocated onto the initial trajectory length and position.

¹ Cf. Luehrs (2013) [57].

² The International Standard Atmosphere is a statistic and idealized model of the atmosphere which represents mean atmospheric conditions (such as air temperature, pressure and density) as a function of altitude, cf. Hack (2008) [29].

³ For more information concerning the standard flight profile, cf. Luehrs (2013) [57].

⁴ Flight level (FL) 380 corresponds to an altitude of 38,000 ft.

⁵ Contingency fuel is measured from trip fuel. For this purpose no other fuel reserves (such as alternate or holding fuel) are included.

⁶ Cf. Nuic et al. (2012) [71].

⁷ Cf. DuBois et al. (2006) [10] and Liebeck (1995) [56].

Elongation of the GC-trajectory

For the purpose of trajectory elongation, each interval (fragment) distance of the reference trajectory (AB) is extended in length by its associated inefficiency factor I and stringed together to an ancillary trajectory ($A'B'$). Based on the sample flight (DUS-YYZ) Table 3.3 illustrates the extension of intervals by their inefficiency factors.

Table 3.3: GC-distance and inefficient distance for the sample flight (DUS-YYZ)

Interval (n)	Region	Type	I [-]	s_{GC} [nm]	s_{ineff} [nm]
1	5	Departure	1.152	50.0	57.6
2	5	Enroute	1.032	597.1	616.2
3	17	Enroute	1.047	1540.6	1613.0
4	2	Enroute	1.027	1081.4	1110.6
5	2	Arrival	1.252	60.0	75.1
Total			1.043	3329.1	3472.5

Consequently, the ancillary trajectory is simulated with the extended ground track distance. For this purpose, the starting point of the trajectory is located on the equator at the prime meridian (at 0°N and 0°E). Figure 3.10 illustrates the departure of the trajectory at the ancillary origin (A') with an azimuth α of 90° . By passing along the equator all intersection points are moved in an easterly direction. The factor of total ground track extension is obtained by comparing total distance of both the initial and the ancillary trajectory.

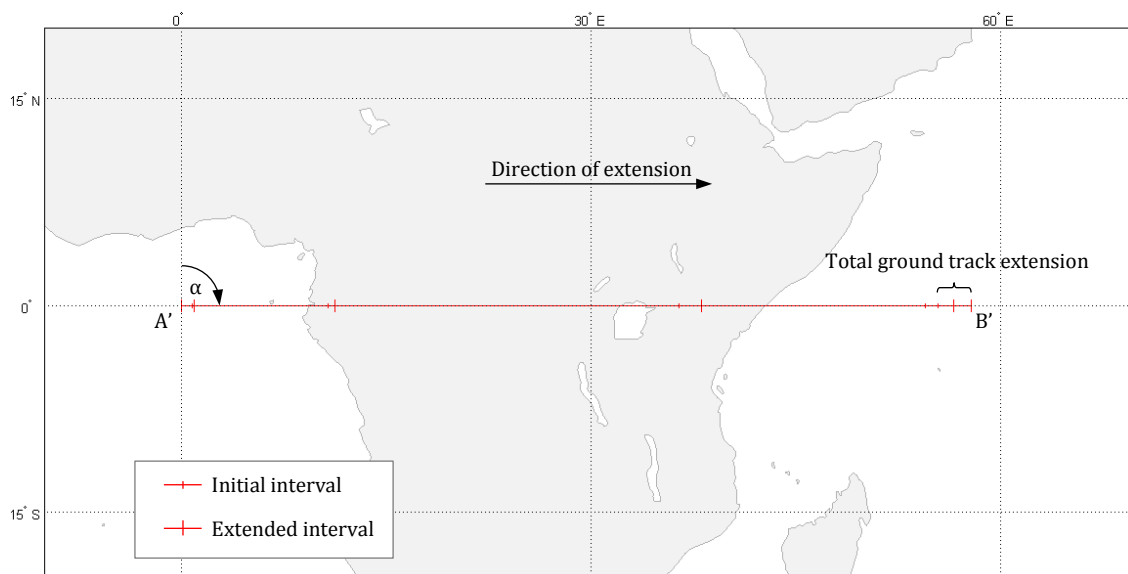


Figure 3.10: Extension of the GC-trajectory

As mentioned above, the trajectory is simulated by means of time increments respectively discrete points along the trajectory for which relevant parameters (such as burned fuel, produced NO_x or flight time) are calculated and cumulated. Consequently, total values are obtained by querying the last point of the trajectory. According to the function `inverseGC`, illustrated by Equation (3.10), the GC-distance is calculated between consecutive discrete points. The discrete distances $ds_{ineff}(i)$ are subsequently saved to a Matlab `.mat`-file utilized during the further processing.¹

$$(ds_{ineff}(i), \alpha(i)) = \text{inverseGC}(\varphi_i, \lambda_i, \varphi_{i+1}, \lambda_{i+1}) \quad (3.10)$$

Compression of the GC-trajectory

For the determination of climate impact, however, it is insufficient to only calculate extended trajectories along the equator. Rather it is necessary to project the arising emissions onto the actual GC-trajectory (AB) since every point within the atmosphere has different climate impact sensitivities defined by the climate cost function (CCF).² For this purpose, the ancillary trajectory ($A'B'$) is compressed and relocated onto the initial trajectory (AB). In this process, the entire vertical profile is compressed as well. Assuming constant climb and descent profiles, both, top of climb (TOC) and top of descent (TOD) are each shifted towards the nearest aerodrome. This is conform to real data trajectories where TOC and TOD are shifted towards the nearest aerodrome due to detouring caused by departure and arrival trajectory inefficiencies (see Figure 2.11).

Regarding trajectory compression and relocation, initially, the starting point (A') of the ancillary trajectory is relocated onto the actual starting point (A). Since the azimuth (α) of the initial trajectory (AB) is known, the GC on which the inefficient trajectory proceeds is known as well. In a next step, the prior saved distances between consecutive discrete points $ds_{ineff}(i)$ are compressed by dividing each distance by the associated inefficiency factor $I(n)$. On the basis of the previous discrete point and

¹ The Matlab routine `inverseGC` is used during TCM calculations to determine distance and azimuth between two points on a sphere. It is therefore comparable to the Matlab function `distance`.

² For more information regarding the climate cost function refer to Chapter 4.2.

the compressed distance the following discrete point is generated by Equation (3.11).¹

$$(\varphi_{i+1}, \lambda_{i+1}) = \text{directGC}\left(\varphi_i, \lambda_i, \alpha(i), \frac{ds_{ineff}(i)}{l(n)}\right) \quad (3.11)$$

Subsequently, the azimuth between the new discrete point and the trajectory's ending point (B) is calculated by Equation (3.10). This loop is repeated for each discrete point until the complete compression of the trajectory. Relevant parameters of each discrete point are not changed but provided with new coordinates. This is done for all discrete points along the trajectory leading to the required compression (Figure 3.11).

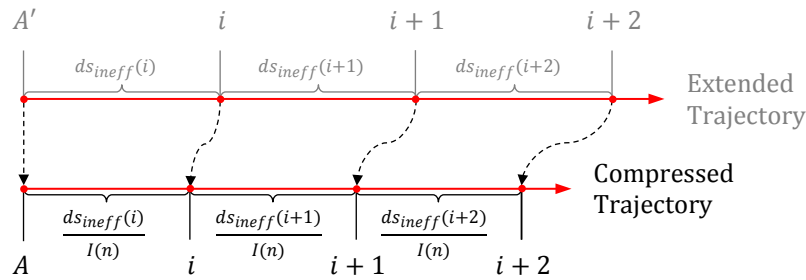


Figure 3.11: Compression of the GC-trajectory

Consequently, the interval transition points coincide with the previously calculated intersection points² (see Table 3.2). The ending point of the ancillary trajectory (B') is relocated on the actual trajectory's ending point (B).

To qualitatively verify the expansion and compression as well as the performance of the model, the following chapter addresses the validation of the implemented model. For this, a use case is applied to compare simulation results of pure GC-trajectories with model-based simulation results and simulation results of the available real data trajectories.

¹ The Matlab function `directGC` is based on a sphere (great circle). The applied equations are to be found in Bronstein (2006) [5], Chapter 3.4.3.4.

² For the calculation of intersection points refer to Chapter 3.3.1.

4 Application of the model

Within this chapter, the qualitative alteration of ground track extension, fuel burn and NO_x-emissions as well as climate impacts shall be demonstrated by means of the simulation of exemplary trajectories if airspace-related trajectory inefficiencies are taken into account. For this purpose, in order to ensure isolated analyses, three separate simulations are executed. Firstly, pure GC-trajectories are conventionally simulated for certain available segments exhibiting the benchmark without the application of trajectory inefficiency. Secondly, real data trajectories are simulated for the same segments to depict a potential contrast between the conventional simulation and “reality”. Finally, inefficient trajectories are simulated by means of the implemented model illustrating the enhancement of simulation results and the approximation to the simulation results of the available real data trajectories. The latter are extracted from the database of IAGOS (In-service Aircraft for a Global Observing System) and MOZAIC (Measurement of Ozone and Water Vapor on Airbus in-service Aircraft)¹, a European Research Infrastructure executing long-term observations of the atmospheric composition measured by internationally operating airlines around the world providing certain Airbus A340 aircraft.² For the purpose of research, the data is available out of charge providing, amongst others, position data with the required trajectory latitude and longitude values.³

For the purpose of trajectory analysis, initially, the preparation of the IAGOS-data and the consequent preprocessing is described (see Chapter 4.1). Secondly, three isolated simulations are executed, based on same segments and equal boundary conditions to point out individual simulation results (see Chapter 4.2).⁴ Finally, the added value of the implemented model is estimated by means of a comparison of these simulation results (see Chapter 4.3).

¹ In the following, the term IAGOS is used for both IAGOS and MOZAIC.

² For the period of interest the participating airlines are: Lufthansa (three aircraft), Air Namibia (one aircraft) and Air China (one aircraft), cf. IAGOS [33].

³ To obtain information concerning the download of the IAGOS-data refer to Annex A.4.

⁴ The year 2012 is defined as the base year, cf. Ghosh (2015) [26].

4.1 Preparation of data extracted from the IAGOS data base

The preparation of IAGOS trajectory data, downloaded from the database, is divided into six individual blocks and performed pursuant to the sequence illustrated in Figure 4.1. Initially, the composition of the raw data files is described (I. block). Secondly, the separation of the data chain into single trajectories is explained (II. block) which are smoothed and removed from latent trajectory inefficiency (III. block). Since there are segments operated by several aircraft, the aircraft-related trajectories are allocated to the associated flight segments (IV. block) and subsequently subdivided according to previously defined flight phases¹ (V. block) for which trajectory inefficiencies are calculated (VI. block).

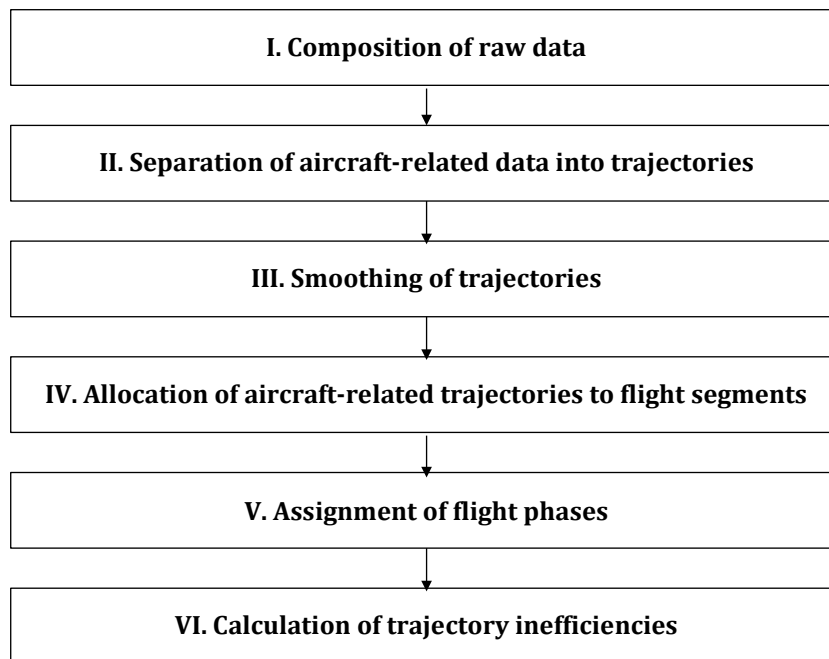


Figure 4.1: Preparation sequence of IAGOS trajectory data

Composition of raw data

In 2012 the available trajectory data is provided by five Airbus A340-300² of three internationally operating airlines. As there is one file per aircraft the extracted trajectories are originally aircraft-related. These are individually read in including at least seven columns of information dependent on the amount of atmospheric information (such as air temperature or relative humidity) additionally selected. Since solely lati-

¹ The delimitation of flight phases is explicitly described in Chapter 2.3.2.

² The Airbus A340-300 is a typical long range aircraft, cf. Airbus [2].

tude and longitude values are of importance for the trajectory analysis, only one atmospheric measurement is additionally selected serving as a dummy to keep the data volume as low as possible. The queried information includes date, time, latitude, longitude, barometric altitude, radio altitude and one atmospheric measurement. Consequently, there is a time-dependence of latitude and longitude values with a sampling time of 4 seconds which is utilized for the further processing.

Separation of aircraft-related data into trajectories

At first, it is evident that there are flights executed beyond the turn of the years 2011/2012 and 2012/2013 resulting in incomplete flights which are manually removed from the raw data files. Herein, at some positions, there are time gaps of irregular duration between executive raw data points, indicating the aircraft's ground times.¹ These are used to divide the data chain of consecutive data points into single flights respectively trajectories. For this purpose, the Matlab function `datenum` is applied to convert the conventional format of date and time into a numeric array representing each point in time as a number of days enabling a simplified time comparison of consecutive data points.² In a next step, successive elements of this time array are compared. The condition to split the data chain into trajectories is fulfilled, where the difference of two consecutive time values exceeds 30 minutes. In this case a new trajectory starts and lasts until the repeated fulfillment of the condition.³

The raw data trajectory latitude and longitude values hold two decimal places. In conjunction with a sampling time of 4 seconds this entails a quite rough trajectory resolution. For this purpose, the trajectories are smoothed to ensure correctly calculated trajectory inefficiency factors.

¹ The available data points are available from takeoff until landing.

² The Matlab function `datenum` is of the type: `datenum(Y, M, D, H, MN, S)`, cf. Mathworks [59]. (Y=Year; M=Month; D=Day; H=Hour; MN=Minutes; S=Second)

³ The ground time condition is parametrically set to 30 minutes which is as long as necessary to bridge potential irregular step sizes and as short as possible to ensure a consideration of the entire ground times of all aircraft.

Smoothing of trajectories

From Figure 4.2 it is evident, that raw data trajectories do not necessarily proceed in a straight way entailing some kind of “latent” inefficiency. As trajectory overall length is calculated by cumulating all point to point distances this has negative impacts on the results of the inefficiency calculation.¹

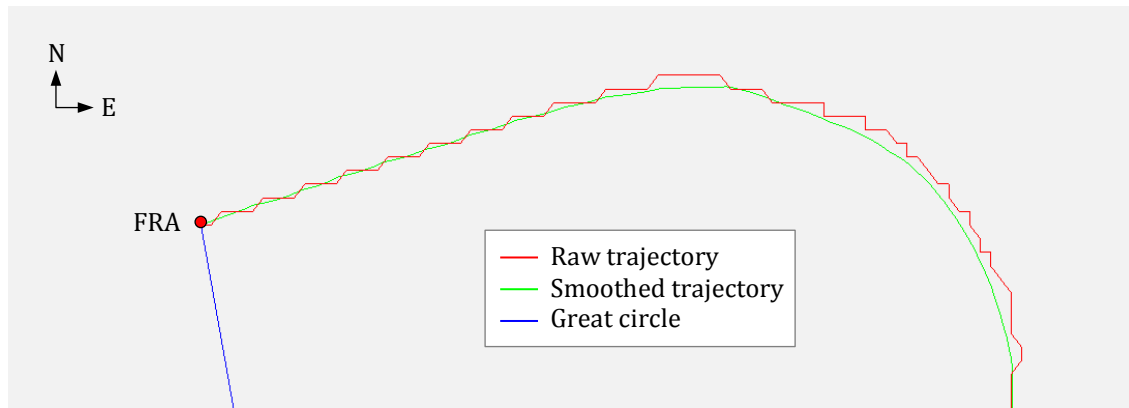


Figure 4.2: Comparison between raw data and smoothed trajectory

Therefore, the peaks of the raw data trajectory are smoothed by means of a low-pass filter applied on the raw data vectors containing latitude φ_{raw} and longitude λ_{raw} values. Consequently, new vectors are created by Equations (4.1) and (4.2) containing smoothed latitude $\varphi_{smoothed}$ and longitude $\lambda_{smoothed}$ values.

$$\varphi_{smoothed}(z) = c_1 \varphi_{smoothed}(z-1) + c_2 \varphi_{raw}(z) \quad (4.1)$$

$$\lambda_{smoothed}(z) = c_1 \lambda_{smoothed}(z-1) + c_2 \lambda_{raw}(z) \quad (4.2)$$

$$\text{with } c_1 + c_2 = 1.$$

The coefficients c_1 and c_2 are determined empirically and have to add up to 1 otherwise the result would be amplified or weakened.² The variable z reaches from 2 to Z which is equal to the number of raw data trajectory elements. While the first value of the smoothed trajectory is equal to the first value of the raw data trajectory ($\varphi_{smoothed}(1) = \varphi_{raw}(1)$; $\lambda_{smoothed}(1) = \lambda_{raw}(1)$), the last value of the smoothed and the raw data trajectories do not comply. Therefore, the last value of the raw data

¹ The calculation of inefficiencies concerning real data trajectories is detailed in Chapter 4.3.

² The low-pass filter coefficients are set to $c_1 = \frac{9}{10}$ and $c_2 = \frac{1}{10}$ showing the best filtering results.

trajectory is added to the end of the smoothed trajectory ($\varphi_{smoothed}(Z + 1) = \varphi_{raw}(Z)$; $\lambda_{smoothed}(Z + 1) = \lambda_{raw}(Z)$). The smoothed, but aircraft-related trajectories are superimposed and illustrated in Figure 4.3. For the period of interest, 98 segments (bidirectional) entailing 2215 flights¹ are extracted from the database; most of the flights originate or terminate in FRA (Frankfurt International Airport). It can be recognized that large portions of the globe are covered. While there is an apparent broad coverage of the North Atlantic, there is no coverage of Australia.

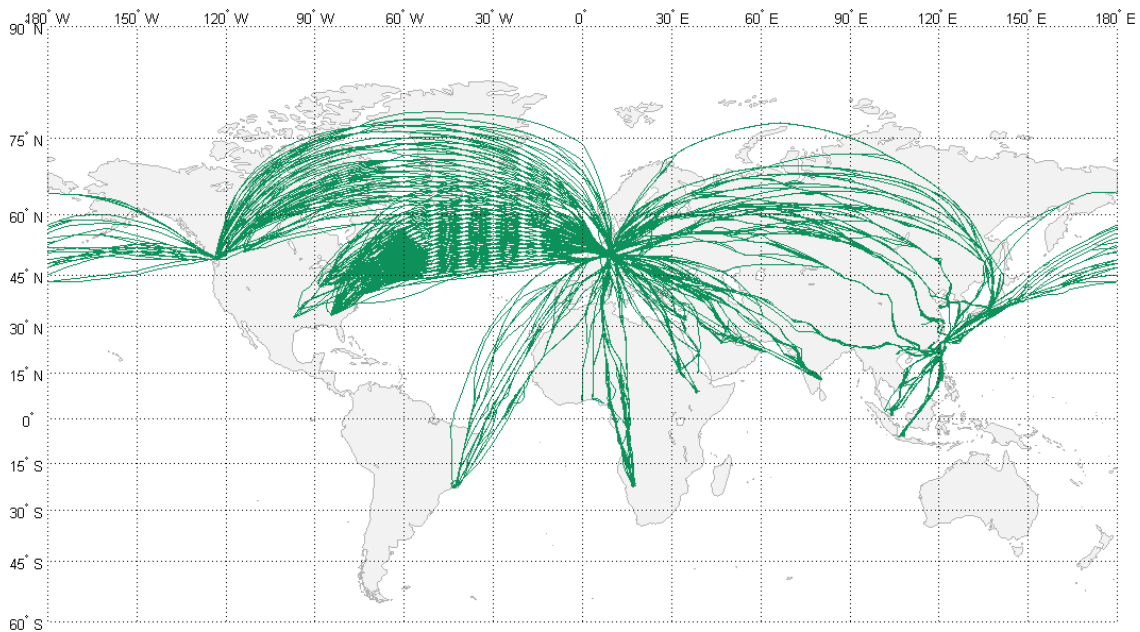


Figure 4.3: Depiction of IAGOS/MOZAIC flights executed in 2012

Allocation of aircraft-related trajectories to flight segments

For further trajectory analyses and forthcoming simulations, the aircraft-related trajectories need to be assigned to segments since there is the chance of segments being operated by several aircraft. For this purpose, the starting and ending points of all trajectories are queried for the consecutively numbered aerodromes.² Thus, each trajectory comprises a set of two numbers which are written one above the other into a matrix which consequently consists of two columns containing the unsorted numbers of departure aerodromes (first column) and arrival aerodromes (second column). Subsequently, the trajectories are ascendingly sorted for the numbers of departure and arrival aerodromes. The segments are then separated by means of a comparison

¹ The number of flights already excludes segments with only one flight in 2012.

² The numbering is made according to the alphabetic order of the 69 aerodromes operated in 2012.

of consecutive numbers of the sorted trajectories within the matrix. If there is a difference either in the first column (departure aerodrome) or in the second column (arrival aerodrome), there is a change over to a new segment for which a further index is generated to ensure the proper allocation of trajectory latitude and longitude values to the correct segment. By joining the latitude and longitude values of the sorted trajectories to the associated segment, the trajectories are related to their segments which are finally saved within a Matlab .mat-file.

Assignment of flight phases – Termination of the departure flight phase

Originating from the trajectory's start point A the GC-distances between consecutive grid points G of the real data trajectory are calculated and cumulated to a departure trajectory distance. Simultaneously, the GC-distance between each grid point and the start point is calculated and compared with the departure radius r_{DEP} . As soon as the distance between G and A is greater than r_{DEP} (grid point located outside of the departure aerodrome airspace) the loop is stopped and the step variable $(i - 1)$ is saved (see Figure 4.4 (a)). Subsequently, the GC-distance between $G(i - 1)$ and the intersection point X_{DEP} with the small circle (magenta line) is determined and added to the cumulated departure trajectory distance. In order to obtain the departure inefficiency factor, the departure distance of the real data trajectory is compared with the departure radius.

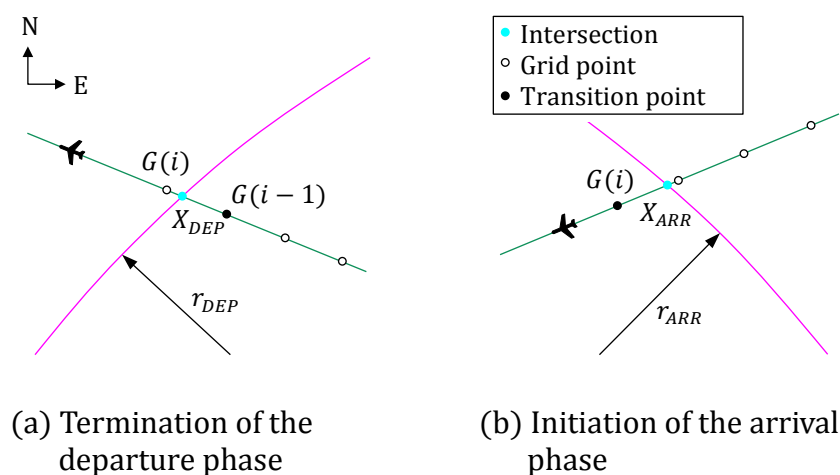


Figure 4.4: Detection principle of flight phase transitions

Assignment of flight phases – Initiation of the arrival flight phase

The arrival trajectory is determined by calculating and cumulating the GC-distance between consecutive grid points G originating from the trajectory's start point A . Simultaneously, the GC-distance between each grid point G and the trajectory's end point B is calculated and compared with the arrival radius r_{ARR} . As soon as the GC-distance between G and B is less than r_{ARR} (grid point located inside of the arrival aerodrome airspace) the loop is stopped and the step variable (i) is saved (see Figure 4.4 (b)). Subsequently, the arrival trajectory distance is determined by calculating and cumulating the GC-distances between consecutive grid points from $G(i)$ to B . Additionally, the distance between $G(i)$ and the intersection point X_{ARR} with the small circle is determined and added to the cumulated arrival trajectory distance. To obtain the arrival inefficiency factor, the arrival trajectory distance is divided by the arrival radius.

Assignment of flight phases – Determination of the enroute flight phase

The enroute trajectory length is straightforwardly determined by subtracting the cumulated departure and arrival trajectory distances from total trajectory length. The result is compared with the enroute segment of the GC-trajectory which is determined by subtracting the departure and arrival radii from total GC-distance.

Calculation of trajectory inefficiencies

To calculate the trajectory inefficiency values, the smoothed trajectory of each flight phase is compared to the associated GC-trajectory. The frequency weighted total median values, concerning departure and arrival inefficiencies of all trajectories, amount to approximately 19.2 % respectively 34.8 %. The frequency and distance weighted¹ total median value of the enroute inefficiencies amounts to approximately 2.5 %. In contrast to the values of departure and arrival inefficiency, the enroute value is lower than the median value from literature.^{2,3} This is traced back to varying compositions of trajectories. While the numbers from above correspond to long haul trajectories only, the values published in literature correspond to mixed trajectories (short, medium and long haul). Consequently, the trajectory inefficiency values from above do

¹ The weighting according to distance as well conduces to the reduction of the impact of short trajectories with potentially higher trajectory inefficiency.

² To obtain information concerning trajectory inefficiencies published in literature, see Chapter 2.4.

³ A detailed inefficiency analysis is illustrated in Annex A.6.

not necessarily represent trajectory inefficiency on a global scale which is the reason why IAGOS trajectory inefficiency values are not applied on the model (see Chapter 2.4). A comparison of enroute trajectory inefficiency could, therefore, only be drawn in regions, where solely long haul traffic is predominant.

Besides the descriptions from above, concerning the determination of enroute trajectory inefficiency, there is an exceptional case where trajectories cross the anti-meridian (see Figure 4.3). In this case the enroute trajectory inefficiency cannot be conventionally calculated, because, as soon as there is a change in sign at the anti-meridian ($\lambda = \pm 180^\circ$), the trajectory sweeps around the longitudes at approximately crossing latitude and connects the last grid point of the trajectory before and the first point beyond the anti-meridian. Due to the change in sign, the depiction and calculation of the affected trajectories are not correct (see Figure 4.5 (a)) and hence, the trajectory smoothing generates erroneous grid points along the connection line. Thereby the entire distance around the earth is additionally calculated entailing a total trajectory length being up to five times longer than the actual trajectory.¹ Consequently, a much too high inefficiency is calculated making the results not usable. This problem is not solved by the Matlab function `flatearthpoly` since the distance from crossing latitude to the pole and back to crossing latitude is calculated as well.² Therefore, the trajectories of the affected segment (TPE-YVR and vice versa) are split at the anti-meridian into two pieces (see Figure 4.5 (b)). For this purpose, consecutive grid points are compared and where there is a change in sign, the step variable (i) is saved.

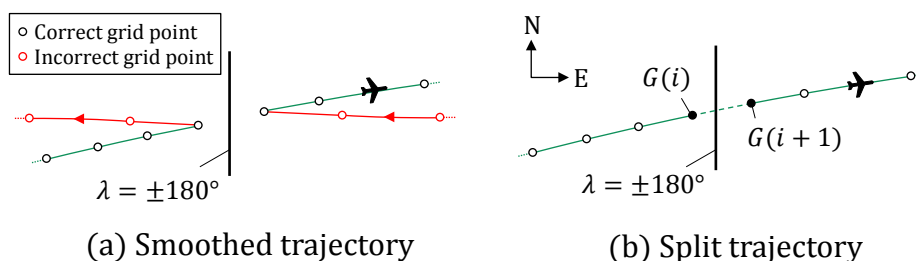


Figure 4.5: Simplified trajectory-splitting at the anti-meridian

¹ The extent of the additional distance depends on actual trajectory length.

² For more information regarding the Matlab function `flatearthpoly` refer to Chapter 3.3.2.

Consequently, the first part of the trajectory ranges from the start point A of the trajectory to the grid point $G(i)$. The second part starts at the grid point $G(i + 1)$ and ranges to the end point B of the trajectory. For both parts the trajectory length is calculated and subsequently added to obtain the actual trajectory length. The determination of trajectory inefficiency then complies to the methodology from above. However, the trajectory segment between the grid point before and beyond the anti-meridian is not considered (dashed line). Regarding a typical cruising speed of 250 m/s and the step size of 4 seconds the absolute error corresponds to approximately 1000 m (0.540 nm).¹ With an average total trajectory distance of 5189 nm the maximum error corresponds to approximately 0.01 % which is neglected.

4.2 Simulation of exemplary trajectories with the TCM

To validate the model, three isolated simulations are executed with the TCM. For this purpose, a trajectory selection of the IAGOS data is extracted in accordance to certain boundary conditions. Since the available real data trajectories are based on the long range aircraft Airbus A340-300, only those flights are considered fulfilling the long range distance condition (1620 nm).² The segment FRA-TLV (bidirectional), however, constitutes an exceptional case whose GC-trajectory is only 1593 nm long. Its inclusion is, firstly, because the corresponding real data trajectories are longer (1634 nm) and, secondly, the GC-trajectory of the next shorter flight is only 1190 nm long.³ The second condition is specified by the number of flights. Therefore, only those segments are considered providing at least 20 flights to ensure a certain degree of representativeness.⁴ After narrowing down the data, 30 segments (bidirectional) entailing 1566 flights are taken into account for the application of the model (see Table A.2).

Assumptions

Hereafter, the trajectories of the selected segments are simulated by the TCM assuming equal atmospheric conditions based on the International Standard Atmosphere (ISA) and without applying wind. Furthermore, a standard flight profile with constant

¹ A typical cruising speed is assumed to be 250 m/s, cf. Luehrs 2013 [57].

² Cf. Mensen 2013 [68].

³ The next shorter flight is TPE-SGN (bidirectional).

⁴ The choice of the frequency condition of 20 flights is arbitrary.

cruise Mach number ($Ma = 0.82$) and constant altitude of 38,000 ft (FL380) is simulated. For the calculation of take-off mass a seat load factor of 85 % and 5 % contingency fuel are assumed.¹ The aircraft performance data of the Airbus A340-313 is provided by BADA (yields burned fuel, H_2O and CO_2).² Non CO_2 -emissions are determined by applying the Boeing Fuel Flow Method 2 which yields produced NO_x .³

In general, air traffic affects climate by emitting carbon dioxides (CO_2), nitrogen oxides (NO_x), water vapor (H_2O)⁴ and aerosols being primarily formed during the cruise phase of a flight.⁵ Assuming a stoichiometric combustion, CO_2 and H_2O are formed directly proportional to fuel burn.⁶ Therefore, only burned fuel and produced NO_x are considered in addition to trajectory inefficiency to validate the model. NO_x -emissions typically increase with increasing engine thrust and are highest during takeoff and climb. Furthermore, NO_x -emissions increase with increasing thrust class particularly of long range aircraft.⁷ As long range flights comprise excessive cruise phases at climate sensitive altitudes, it is necessary to additionally consider their climate impact. This is calculated by AirClim and expressed as Average Temperature Response (ATR_{100}) for each climate agent over 100 years. Its spatial distribution is referred as climate cost function (CCF) which is available for large portions of Europe and North America as well as for the northern Atlantic. However, due to the limited number of available trajectories proceeding within this area a global statement concerning ATR_{100} results, in particular concerning the model, is not feasible, since climate sensitivity and consequent ATR_{100} values are strongly location-dependent. A validation by means of ATR_{100} is therefore excluded.

In the following, firstly, GC-trajectories of the considered segments are simulated without applying any efficiency constraints constituting the state of the art within

¹ The amount of contingency fuel is measured from trip fuel. For the purpose of the simulations no other fuel reserves (alternate or holding fuel) are included.

² Cf. Nuic et al. (2012) [71].

³ Cf. DuBois et al. (2006) [10] and Liebeck (1995) [56].

⁴ The emission of H_2O causes the formation of contrails potentially resulting in Contrail Induced Cloudiness (CIC).

⁵ Cf. Luehrs (2013) [57].

⁶ During the stoichiometric combustion of 1 kg fuel, 3.15 kg of CO_2 and 1.24 kg of H_2O are formed, cf. Gmelin (2008) [27].

⁷ Cf. Mensen (2013) [68], page 1419.

AIRCAST serving as the reference simulation (see Chapter 4.2.1). Secondly, real data trajectories are simulated by means of the available IAGOS trajectories (see Chapter 4.2.2). Finally, the GC-trajectories are simulated with the implemented model providing trajectory inefficiencies (see Chapter 4.2.3) to enable the subsequent estimation of the benefits of the model by comparing the results with the previous simulations.

4.2.1 Calculation of reference trajectories

For comparison purposes pure GC-trajectories are simulated without any constraints in ATM and ATS representing the status quo of TCM simulation and therefore serving as the benchmark for the following analysis. Based on the assumptions from above, the reference simulation yields certain absolute values of trajectory distance, burned fuel and NO_x for each segment. These values are obtained by simulating pure GC-trajectory of each segment.¹ The GC-trajectories (bidirectional) are illustrated in Figure 4.6 where origins and destinations are indicated by means of their IATA three letter codes.²

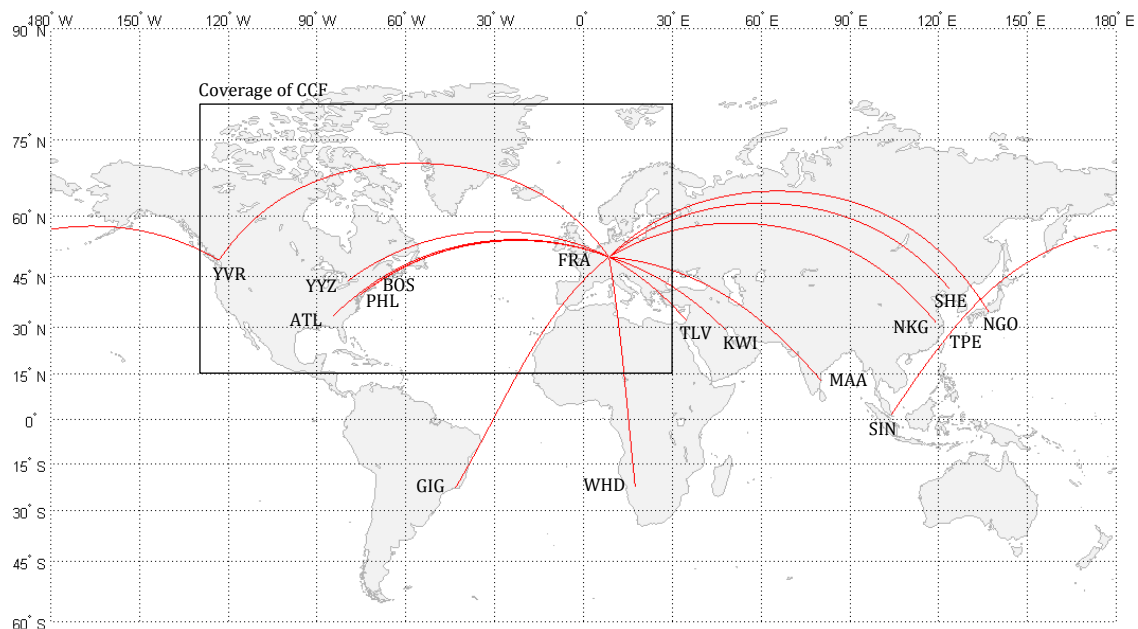


Figure 4.6: GC-trajectories of IAGOS top 30 segments

¹ For detailed information concerning the simulation with TCM cf. Luehrs (2013) [57].

² The underlying aerodromes and their coordinates are listed in Annex A.5.

In a next step, the climate impact of these GC-trajectories is calculated by means of AirClim and expressed as ATR_{100} . This is calculated for each trajectory between 15°N and 80°N latitude and between 130°W and 30°E longitude. Vertically it is limited by FL250 and FL390. Due to the lateral delimitation of the CCF the analysis is limited to a certain number of trajectories exclusively proceeding between Europe and North America. In this context, it is quite possible that the ATR_{100} of a GC-trajectory is higher than the ATR_{100} of its corresponding real data trajectory although its ground distance is longer. This can be traced back to a routing of the real trajectory within a less climate sensitive region (see Figure 4.11).¹

4.2.2 Calculation of real data trajectories

In contrast to the reference simulation, this section describes the simulation of real data trajectories. For the purpose of comparison, the results are normalized to the reference value of the reference GC-trajectory by using the Equations (4.1) to (4.4).²

$$S_{AB,rel} = \frac{S_{AB}}{S_{AB,ref}} \quad (4.1)$$

$$m_{BF,rel} = \frac{m_{BF}}{m_{BF,ref}} \quad (4.2)$$

$$m_{NO_x,rel} = \frac{m_{NO_x}}{m_{NO_x,ref}} \quad (4.3)$$

$$ATR_{rel} = \frac{ATR}{ATR_{ref}} \quad (4.4)$$

Afterwards, the median of each segment is calculated and weighted by frequency to a total value for comparison purposes.³ When comparing the trajectories illustrated in Figure 4.7 with those of the previous simulation (see Figure 4.6) an occasional lateral deviation is evident entailing increased values of burned fuel and NO_x . In total, the frequency weighted values of burned fuel and NO_x exceed the benchmark by approximately 3.87 percent respectively 4.22 percent. The associated additional ground track distance only amounts to approximately 3.29 percent which, in turn, can be in-

¹ Cf. Niklaß et al. (2015) [70].

² A detailed comparison of burned fuel and NO_x per segment can be found in the Annexes A.8 and A.9.

³ The weighting according to frequency conduces to the reduction of the impact of segment with less connections but potentially higher trajectory inefficiency and consequent increased burned fuel and produced NO_x .

terpreted as total trajectory inefficiency. With respect to the climate impact of real data trajectories the results show an increased ATR_{100} value as well.¹ This exceeds the benchmark by approximately 6.98 percent.²

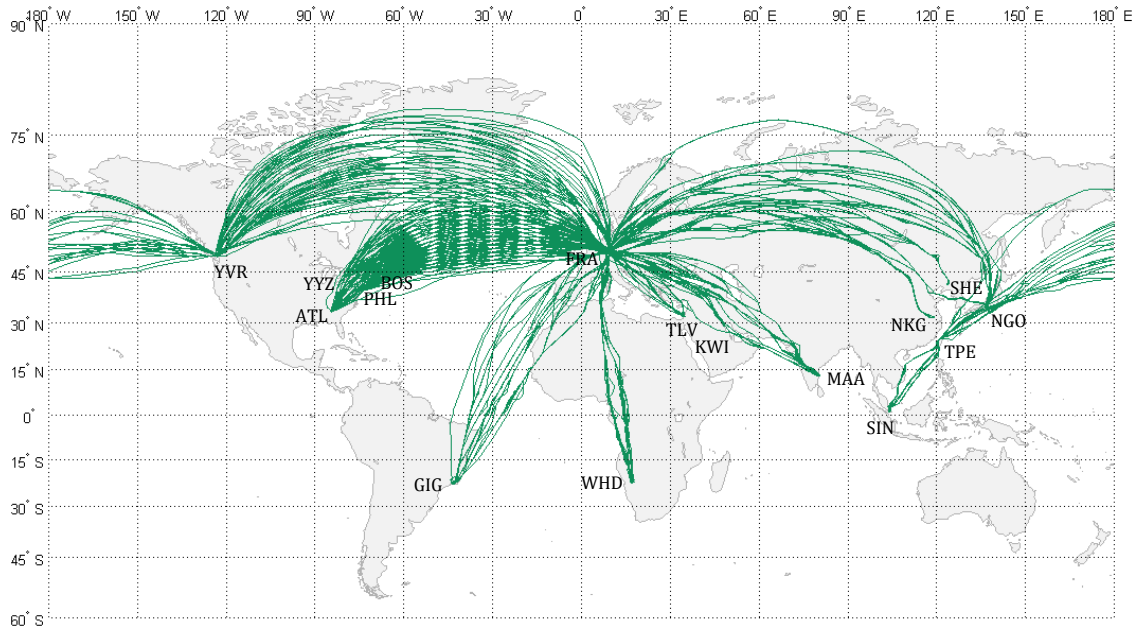


Figure 4.7: Real data trajectories of IAGOS top 30 segments

4.2.3 Calculation of inefficient trajectories

This chapter addresses a simulation comparable with the simulation of pure GC-trajectories, however, by applying trajectory inefficiencies by means of the implemented model (model-based simulation).³ For this purpose, first, the aerodrome coordinates are made available for the model. With the help of these coordinates the considered GC-trajectories are fragmented.⁴ The GC-trajectories (bidirectional) are illustrated in Figure 4.8 showing the fragmentation by regions (black polygons) and aerodrome airspaces (magenta circles). The intersection points with the polygons and the aerodrome airspaces are represented by the green respectively cyan points.⁵ Due to the small map scale and bidirectional trajectories, entailing a graphical overlapping of the departure and arrival aerodrome airspaces, their distinction is not nec-

¹ For the calculation of climate impact cf. Niklaß et al. (2015) [70].

² A detailed ATR_{100} -comparison of the underlying segments can be found in Annexes A.10 and A.14.

³ The development of the model is described in Chapter 3.

⁴ For the fragmentation of the trajectory refer to Chapter 3.3.

⁵ The intersection points are calculated in accordance to the methodology explained in Chapter 3.3.1.

essarily evident which, however, only refers to the selected graphical representation and does not affect calculations.¹ Afterwards, the trajectory inefficiencies of the affected regions are assigned to the associated trajectory fragments and provided for the simulation.²

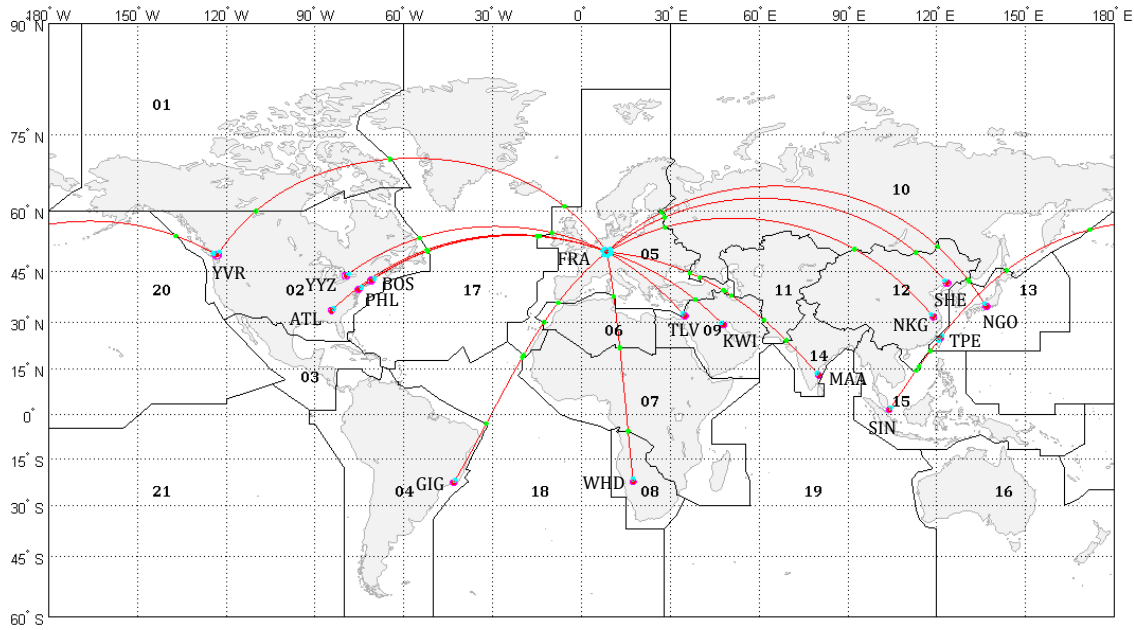


Figure 4.8: Fragmented GC-trajectories of IAGOS top 30 segments

By means of the provided data, the trajectories are simulated by the TCM.³ Compared to the results of the reference simulation, the values of burned fuel and NO_x exceed the benchmark by approximately 5.77 percent respectively 6.33 percent. The associated additional ground track distance amounts to about 4.86 percent. The determined climate impact (ATR_{100})⁴ exceeded the reference simulation of pure GC-trajectories by approximately 5.51 percent.⁵

¹ A more detailed illustration of the overlapping of departure and arrival aerodrome airspaces can be found in Figure 3.6. For their separate illustration refer to Figure 3.7.

² The data provision for the simulation is described in Chapter 3.4.1.

³ The simulation is performed in accordance to Chapter 3.4.2.

⁴ For the calculation regarding ATR_{100} cf. Niklaß et al. (2015) [70].

⁵ A detailed ATR_{100} -comparison of the underlying segments is listed in Annexes A.10 and A.14.

4.3 Results

In the previous sections, three isolated trajectory simulations were performed whose results are used to assess the benefits of the implemented model relative to pure GC-simulations and to show the approximation to real data. Compared to the GC-based simulation, both, the simulation of real data trajectories and the simulation with applied inefficiencies (model-based simulation) show elevated levels of distance, burned fuel, NO_x and ATR_{100} . Total results from the simulations above are provided in Table 4.1 from where it is evident that, against conventional simulation results, simulation results with regard to the implemented model approximate the results of the considered real data trajectories of IAGOS.¹

Table 4.1: Comparison of distance, fuel burn, NO_x and ATR_{100} relative to GC ²

Parameter	IAGOS	Model	Difference Model-IAGOS
$s_{AB,rel}$	1.03289	1.04861	0.01572
$m_{BF,rel}$	1.03867	1.05767	0.01901
$m_{\text{NO}_x,rel}$	1.04218	1.06333	0.02115
$\text{ATR}_{100,rel}$	1.06979	1.05511	-0.01467

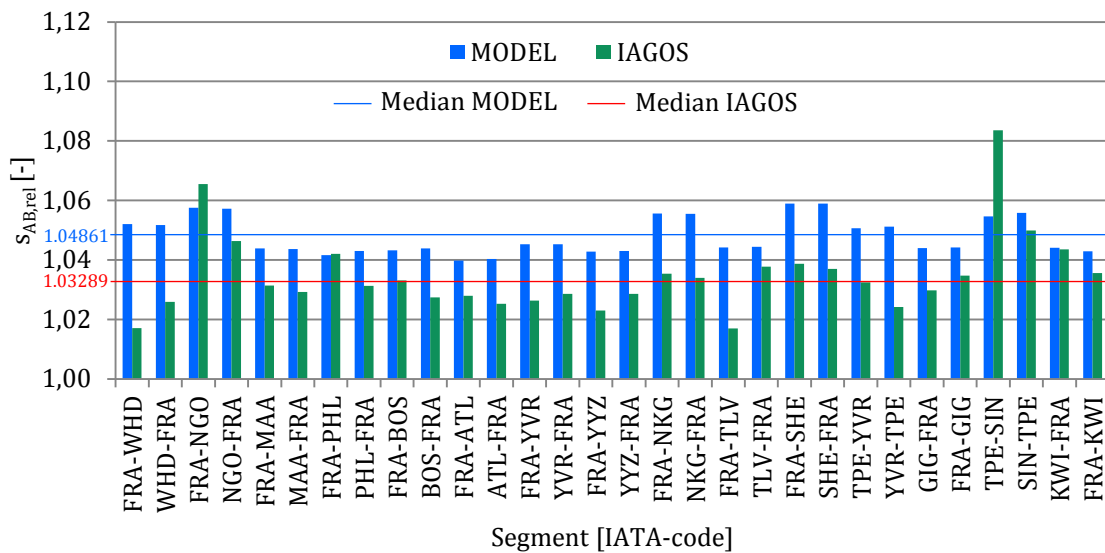
It is also striking that the relevant parameters disproportionately increase against trajectory inefficiency ($s_{AB,rel}$). The increased relative values of burned fuel and NO_x are reducible to higher takeoff masses caused by an increased fuel requirement due to longer trajectories. Consequently, the heavier aircraft entails a reduced climb rate and therefore a longer climb phase which raises NO_x emissions. Furthermore, with reservation regarding the available real data trajectories, it is evident that model-based simulation results overestimate the results of the IAGOS simulation. This is presumably reducible to the application of general trajectory inefficiencies on long range trajectories wherefore the model-based simulation consequently calculates a more inefficient ATS compared to the available real data trajectories. In contrast, ATR_{100} underestimates the IAGOS simulation results. This, however, only refers to the analyzed data and can substantial differ when considering other trajectories.

¹ A detailed comparison on segment level can be found in the Annexes A.7, A.8, A.9 and A.10.

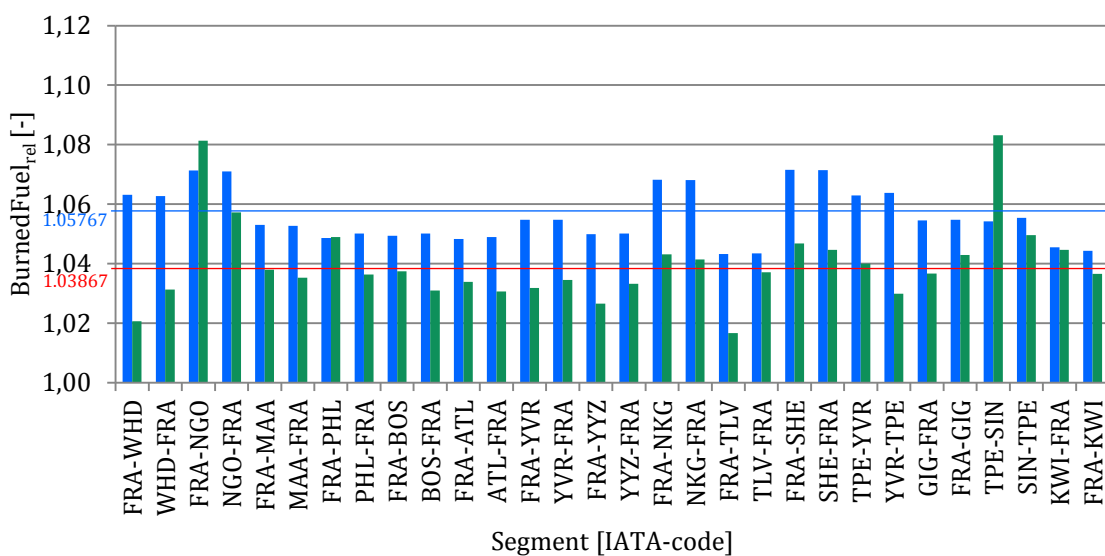
² While $\text{ATR}_{100,rel}$ is related to segments between Europe and northern America only (n=10), $s_{AB,rel}$, $m_{BF,rel}$ and $m_{\text{NO}_x,rel}$ are related to all considered segments (n=30).

Figure 4.9 visualizes the values of Table 4.1 against model-based and IAGOS simulation results per segment which are sorted by frequency in descending order. Considering each segment individually, it is evident that model-based simulation results are almost consistently closer to the analyzed real data trajectories than to pure GC-trajectories. Contrary to the standard, there are two sheering segments resulting from real trajectories being less efficient than estimated by the model. This is also reflected in the parameters $BurnedFuel_{rel}$ and $ProducedNO_{x,rel}$ and presumably reducible to a particularly inefficient routing. In this context, the segment TPE-SIN especially strikes (Figure 4.9 (a) to (c)).

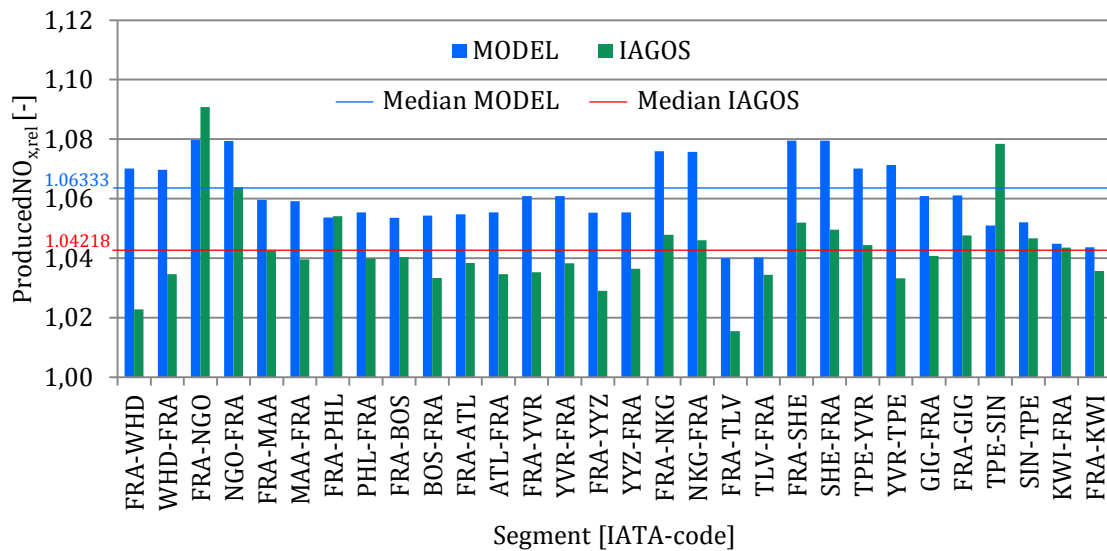
(a) Distance relative to GC of IAGOS and model-based simulation per segment



(b) Burned fuel relative to GC of IAGOS and model-based simulation per segment



(c) Produced NO_x relative to GC of IAGOS and model-based simulation per segment



(d) ATR_{100} relative to GC of IAGOS and model-based simulation per segment

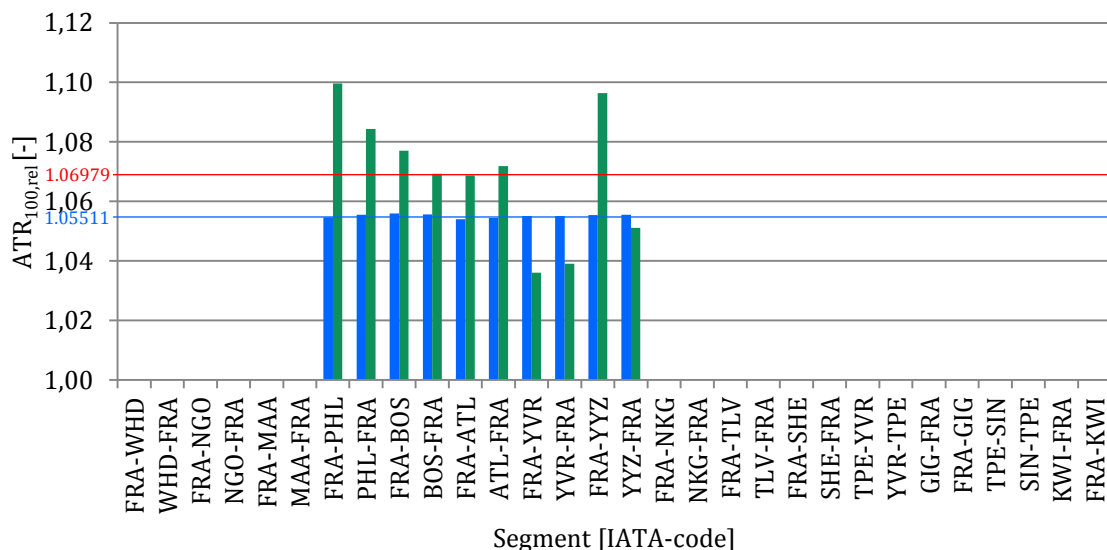


Figure 4.9: Distance, fuel burn, NO_x and ATR_{100} against GC per segment

Considering $\text{ATR}_{100,rel}$ (Figure 4.9 (d)) it is evident that only a limited number of segments is available. Because of this and due to the special delineation of the CCF a global statement is not possible. For this special case, however, the $\text{ATR}_{100,rel}$ results underestimate the corresponding IAGOS simulation results by approximately 1.47 percent.¹ Since deviating from the results of other parameters (BurnedFuel_{rel} and $\text{ProducedNO}_{x,rel}$) the underestimation of $\text{ATR}_{100,rel}$ requires a further analysis wherefore it is split into its components. These are $\text{ATR}_{\text{CO}_2,rel}$, $\text{ATR}_{\text{NO}_x,rel}$, $\text{ATR}_{\text{H}_2\text{O},rel}$ and $\text{ATR}_{\text{Cont},rel}$ being compared by means of a sample flight between FRA and PHL visual-

¹ In contrast, the other parameters overestimate IAGOS simulation results (see Figure 4.9 (a) to (c)).

ized in Figure 4.10. The results of the model-based simulation (blue) are contrasted with the results of the IAGOS simulation (red) and the simulation of pure GC-trajectories (black). For this specific sample flight it is evident that the frequency weighted median values of IAGOS trajectories are only slightly underestimated by the respective model-based simulation results showing, however, an almost complete agreement, except for $ATR_{Cont,rel}$ which is the reason why this sample flight is especially significant for this analysis.

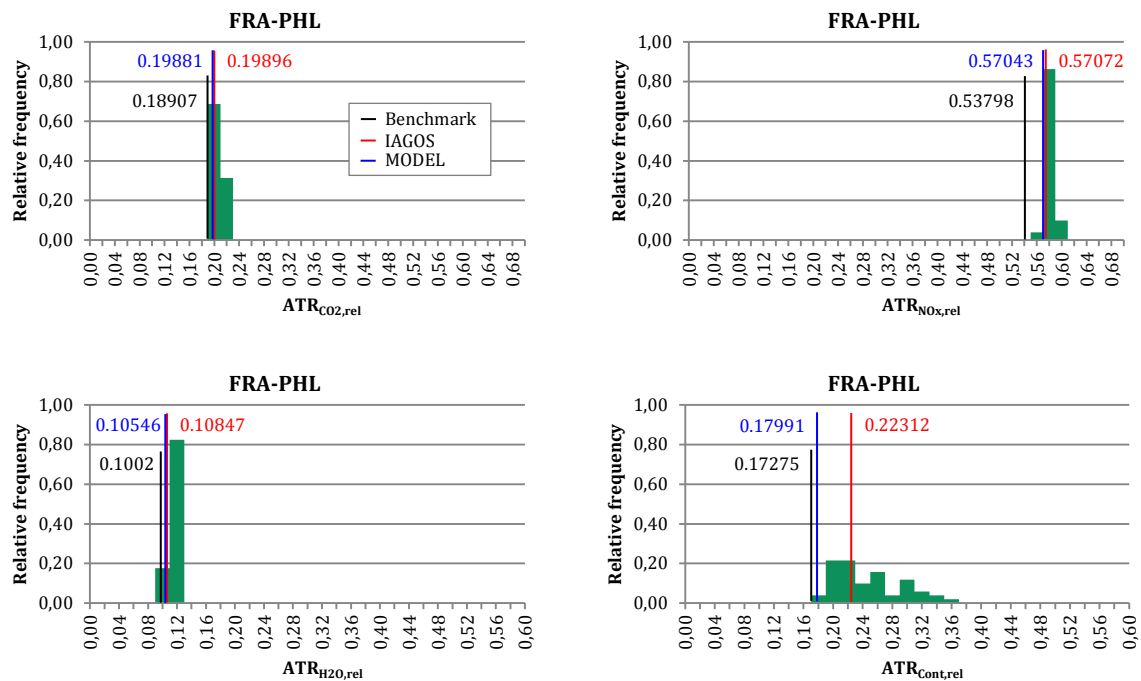


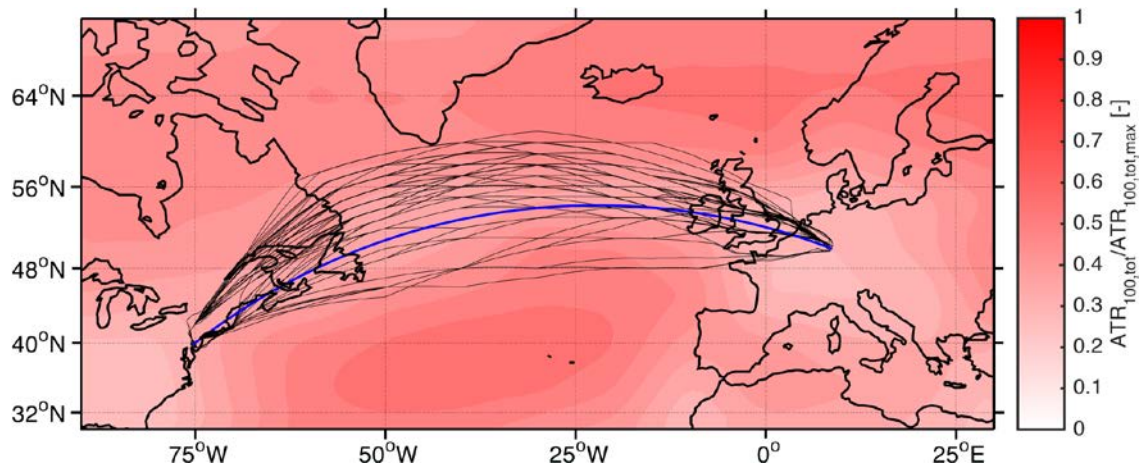
Figure 4.10: Comparison of ATR_{100} components between FRA and PHL

From this sample flight as well as from other segments it appears that the underestimation of total $ATR_{100,rel}$ against the other parameters ($BurnedFuel_{rel}$ and $ProducedNO_{x,rel}$) is presumably reducible to $ATR_{Cont,rel}$ where the deviation between the model and the analyzed real data trajectories is greatest. Figure 4.11 therefore illustrates both, the total Climate Cost Function CCF (Figure 4.11 (a)) as well as the CCF of Contrail Induced Cloudiness (CIC) (Figure 4.11 (b)). These are derived with AirClim at a simulated cruising altitude of 38,000 ft (FL380). While $ATR_{Cont,rel}$ is defined three dimensionally, using latitude and longitude values as well as distance ($v_{TAS}(t) \cdot dt$), all other ATR_{100} components are defined two dimensionally (latitude and longitude).¹

¹ Cf. Niklaß et al. (2015) [70].

When comparing the sensitivity distribution of both CCFs it is obvious that $ATR_{Cont,rel}$ significantly affects total ATR_{100} . At closer examination of Figure 4.11, the GC-trajectory (blue line) obviously passes through the area of less climate sensitivity. This applies for the simulation of the pure-GC-trajectory as well, wherefore the results of the model-based simulation are closer to the simulation results of pure GC-trajectories (see Figure 4.10 (bottom right)). In contrast to that, the real data trajectories proceed apart from the GC-trajectory within more climate sensitive areas which is the reason for the underestimation of model-based total ATR_{100} . The development of less climate sensitive areas stems from the water vapor saturation due to frequent traffic within this areas entailing a reduced impact of single flights.

(a) Total Climate Cost Function (CCF)



(b) Contrail induced Cloudiness (CIC) CCF

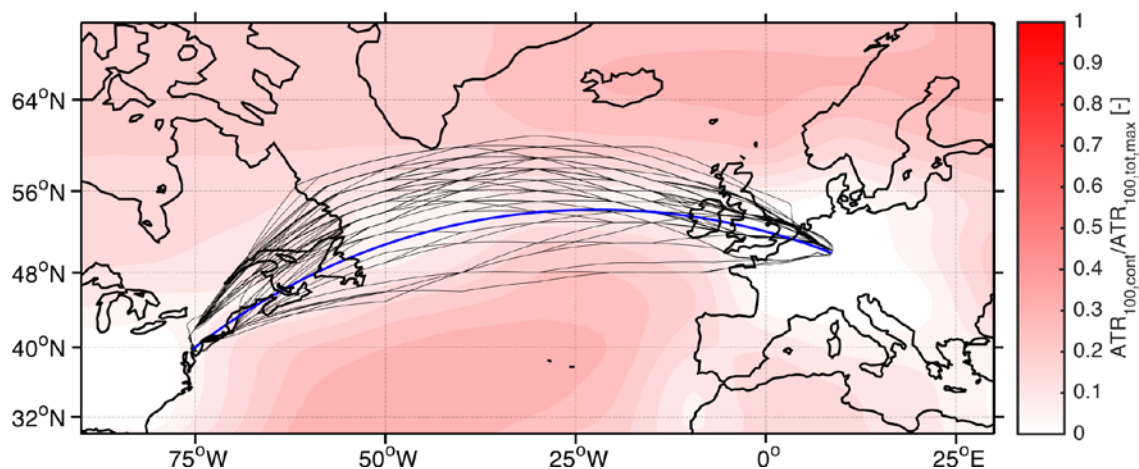


Figure 4.11: Climate cost functions at FL380 derived with AirClim¹

¹ Background information on the used abbreviations: CCF (Climate Cost Function); CIC (Contrail Induces Cloudiness).

Conversely, when considering other trajectories potentially passing through areas of higher climate sensitivity the results would consequently differ from present simulation results. Due to the limited number of trajectories available for the area covered by the CCF it is impossible to make a global statement concerning ATR₁₀₀ results. To globally validate the model by means of climate impact it is therefore necessary to execute prospective studies analyzing a greater number of mixed trajectories by means of a global CCF since climate impact of non-CO₂ emissions strongly depends on location.¹

On balance, the simulation yields a considerable enhancement of results when taking lateral trajectory inefficiencies into account. Consequently, the gap between real data simulation results and model-based simulation results is apparently reduced. This is accompanied by another benefit of the model concerning the simulation within AIR-CAST. Due to increased flight time caused by the inefficient trajectory, block time is increased as well which has direct impacts on variable unit cost such as crew cost and the quality of travel from a passenger perspective. Furthermore, it is assumed that model accuracy increases when considering an overall ATS also including trajectories of intra-regional flights. It was found in literature that trajectory inefficiencies of long haul flights substantially differ from intra-regional flights. While total ground track extension of international long haul flights amounts to 3.3 percent, domestic flights within certain regions exhibit increased total ground track extensions (14 percent in Europe and 12 percent in the US).² The higher values of total ground track extension, compared to enroute inefficiency, potentially arise from reduced total length of trajectories and the increased impact of departure and arrival inefficiency.

Since pursuing data regarding this is not available it is therefore conceivable that present trajectory inefficiencies will be adjusted by means of prospective analyses of more global mixed real data trajectories possibly generating more accurate region-related trajectory inefficiency values. In this context, a distinction between long and short range trajectory inefficiencies could potentially be drawn.

¹ Cf. Niklaß et al. (2015) [70].

² Cf. Reynolds (2014) [74]. The total ground track extension of the analyzed IAGOS long haul trajectories also amounts to 3.3 percent.

5 Conclusion and outlook

This chapter provides a general conclusion regarding the results and benefits of the model developed in this Master Thesis as well as an outlook on potential research needs by prospective studies contributing to the further enhancement of simulations.

5.1 Conclusion

The first thematic emphasis of this Master Thesis was to generate different world regions in order to consider regional differences of lateral airspace-related trajectory inefficiencies in such a way being depicted in the simulation of trajectories executed with the TCM. In total, 21 regions were determined providing individual inefficiencies as well as a global coverage.¹ Due to different potential causes of inefficiencies being related to different flight phases, trajectory inefficiencies particularly consider variations regarding the flight phases: departure, enroute and arrival. To enable this, a comparison of SIDs² and STARs³ of numerous national and international aerodromes resulted in a termination of the departure phase 50 nm after takeoff and an initiation of the arrival phase 60 nm prior to land.⁴ Regarding these flight phases and the world regions, trajectory inefficiencies were specified for the AIRCAST⁵ base year 2012.⁶

The major thematic emphasis of this Master Thesis, however, was placed on the development of a generic model with Matlab to depict lateral airspace-related trajectory inefficiencies for the application in prospective simulations. In this context, first, fundamental trajectory parameters were explained for their further use during the calculations executed by the model.⁷ Subsequently, the previously defined regions and the

¹ See Chapter 2.3.1 above for more details.

² SID: Standard Instrument Departure.

³ STAR: Standard Instrument Arrival.

⁴ See Chapter 2.3.2 above for more details.

⁵ AIRCAST: Air Travel Forecast.

⁶ See Chapter 2.4 above for more details.

⁷ See Chapter 3.1 above for more details.

delimitation of flight phases were modeled.¹ On the basis of this, a fragmentation of the trajectory is performed which constitutes the core of the model. In this context, potential flight phase transitions and intersection points with the regions are determined.² Due to side effects from trajectory calculations these may include erroneously calculated intersection points which are eliminated ensuring a proper depiction of common trajectories on a global scale.³ In a next step, the corrected intersection points are provided along with the associated fragment-related trajectory inefficiencies for the TCM simulation.⁴ At this, the inefficient trajectory is simulated along the equator by extending the initial GC-trajectory fragments by their associated inefficiency factors resulting in an overall extended ancillary trajectory. As every point within the atmosphere has different climate impact sensitivities it is necessary to project the arising emissions of the ancillary trajectory onto the actual GC-trajectory. This is realized by a compression and relocation onto the initial trajectory length and position by compressing the distances between the trajectory's discrete points by the associated inefficiency factors.⁵

Within the last chapter the model was applied and validated, estimating to what extent future trajectory simulations would approximate reality. For this purpose, three isolated simulations were executed comprising: firstly, a reference simulation of pure GC-trajectories; secondly, a simulation of available real data trajectories obtained from the IAGOS⁶ database and; finally, a simulation which considers trajectory inefficiencies by implementing the model developed in this Master Thesis.⁷ In this context, the simulation results were compared to assess the benefits of this model.⁸ It was established that, with regard to total inefficiency of the analyzed trajectories, the simulation results based on the implemented model slightly overestimate the available real data trajectories by approximately 1.52 percent. The overestimation is presuma-

¹ See Chapter 3.2 above for more details.

² See Chapter 3.3.1 above for more details.

³ See Chapter 3.3.2 above for more details.

⁴ See Chapter 3.4.1 above for more details.

⁵ See Chapter 3.4.2 above for more details.

⁶ IAGOS: In-service Aircraft for a Global Observing System which is a European research infrastructure executing long-term observations of the atmospheric composition providing a database for atmospheric data on a global scale.

⁷ See Chapter 4.2 above for more details.

⁸ See Chapter 4.3 above for more details.

bly reducible to the application of general trajectory inefficiencies (also designed for short and medium range trajectories) on long range trajectories. However, this is closer to the simulation results of the available real data trajectories than the simulation results of pure GC-simulation (approximately 3.29 percent). For the simulation within AIRCAST the simulation of inefficient trajectories has wider implications. With regard to increased flight time, block time is increases as well which has direct impacts on variable unit cost such as crew cost and the quality of travel from a passenger perspective. With regard to burned fuel, the simulation of inefficient trajectories overestimates the simulation of the available real data trajectories by approximately 1.90 percent. In contrast, the reference simulation is approximately 3.87 percent away from the available real data trajectories. While the simulation of inefficient trajectories generates approximately 2.12 percent more NO_x than real data trajectory simulation, the reference simulation underestimates this by approximately 4.22 percent. It is striking that burned fuel and NO_x disproportionately increase against trajectory inefficiency. These are reducible to higher takeoff masses caused by an increased fuel requirement due to longer trajectories. Consequently, the heavier aircraft entails a reduced climb rate and therefore a longer climb phase which raises NO_x emissions. Concerning ATR₁₀₀-results, the model-based simulation results underestimate simulation results of the available real data trajectories by approximately 1.37 percent. This is possibly traced back to a routing of real data trajectories within more climate sensitive areas compared to the corresponding GC-trajectories. Here, too, the simulation of inefficient trajectories is closer to the simulation of the available real data trajectories than the simulation of pure GC-trajectories (approximately 5.51 percent).

On balance, when considering trajectory inefficiencies, the model-based simulation results consistently approximate simulation results of the available real data trajectories showing a clear added value against conventional simulations. Due to the limited number of real data trajectories available and the spatial delimitation of the CCF¹, a global statement, concerning ATR₁₀₀ results, is not feasible on the basis of the trajectories analyzed within this Master Thesis. However, circumstantial evidence points out that the modeled climate impact (ATR₁₀₀) with the inefficiency model is closer to

¹ CCF: Climate Cost Function.

reality than without the model. To globally validate the model by means of ATR₁₀₀ it is necessary to execute prospective studies analyzing mixed trajectories by means of a global CCF since climate impacts of non-CO₂ emissions strongly depend on location.

5.2 Outlook

By considering trajectory inefficiencies in future simulations the generic model developed through this Master Thesis constitutes a sound basis and enhancement for pursuing, especially quantitative studies.

For the purpose of this Master Thesis a zero-improvement/-worsening scenario was assumed while differences in regional trajectory inefficiencies are kept constant for all time slices (2012-2050). However, when adapting prospective trajectory inefficiencies, alterations of flight guidance can be considered on a global scale leading to an adjustment of fuel consumption and emissions contributing to more accurate forecasts of climate impacts. It is therefore conceivable that trajectory inefficiencies will be adjusted by means of a more global analyzation of mixed real data trajectories including the consideration of vertical trajectory inefficiencies potentially generating more accurate region-related trajectory inefficiency values. Furthermore, the analysis of the available real data trajectories yields evident differences between airports regarding departure and arrival trajectory inefficiencies. However, these are neither reducible to regions being located in nor to airport size. For this reason, investigations of correlations between aerodromes and departure and arrival trajectory inefficiencies should be carried out in prospective studies. Last but not least, consideration should be given to the comparison of wind-optimized trajectories with real data trajectories. This would potentially yield trajectory inefficiencies by means of air distance being more pronounced in terms of flight time. However, regarding future scenarios, this proves difficult since prospective wind fields are unknown.

A Annex

A.1 FIRs by ATFM implementation status (2014)

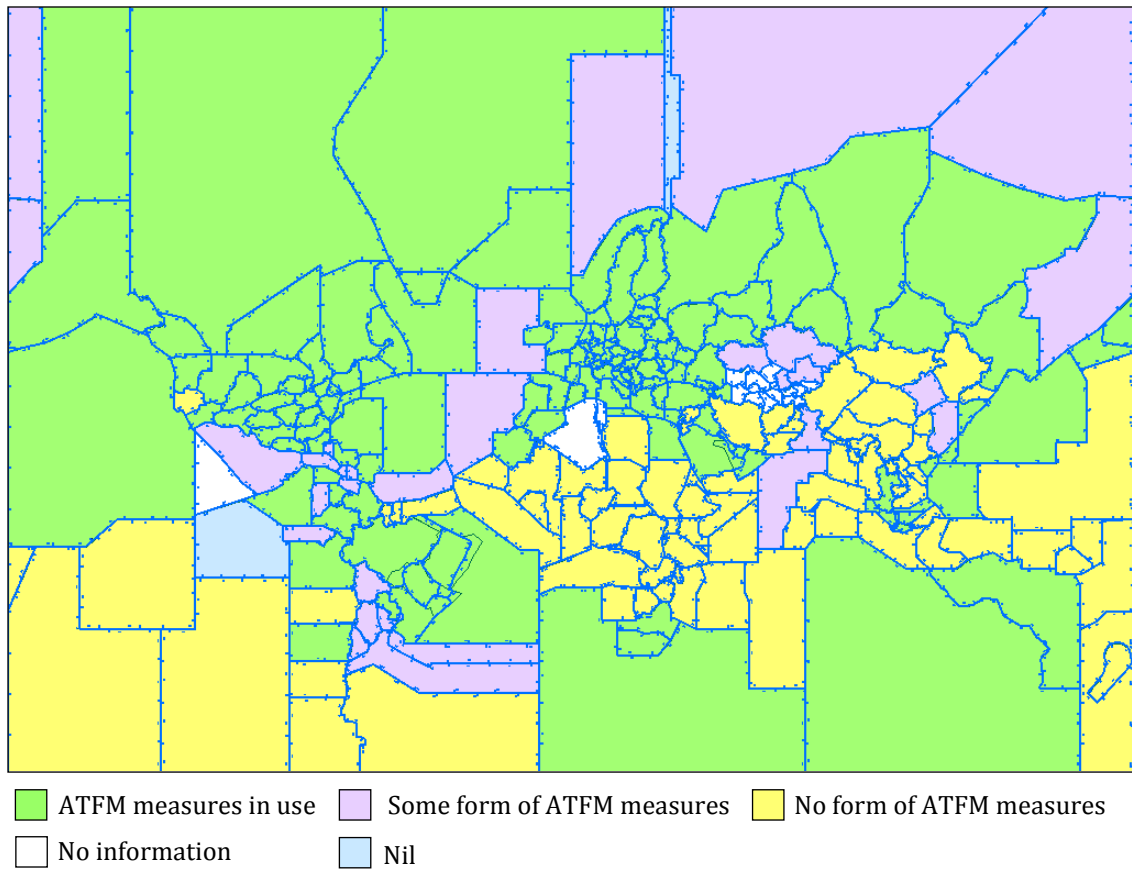


Figure A.1: FIRs by ATFM implementation status ¹

¹ Cf. ICAO [40], ATFM status layer.

A.2 FIRs by traffic volume (2010)

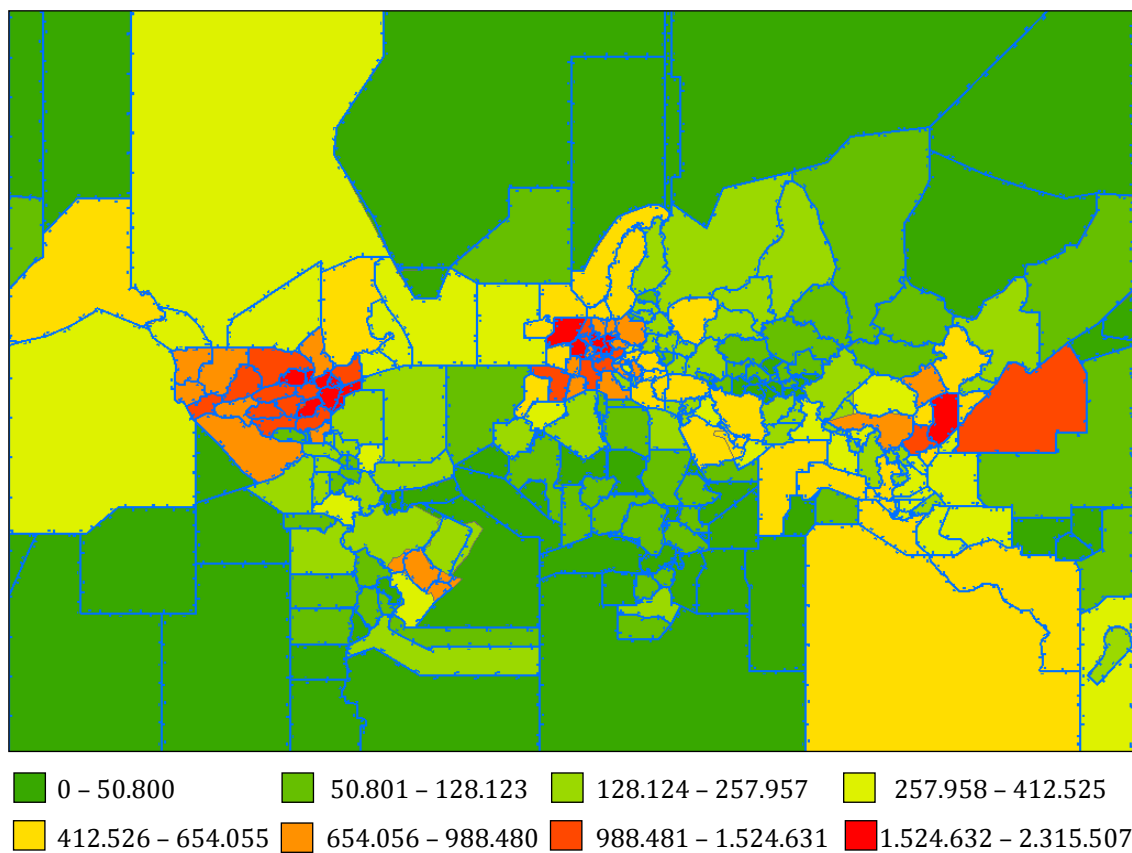


Figure A.2: FIRs by air traffic volume ¹

¹ Traffic volumes by movements in 2010, cf. ICAO [40], 2010 NB Vol/FIRs layer.

A.3 Comparison of projects providing emissions inventories

Table A.1: Comparison of projects providing emission inventories

	AIM	AERO2k	ANCAT/ EC-2	DLR	DLR-2	NASA	AERO-MS	AIRCAST
Publication	Krammer 2011	Eyers et al. 2004	Gardner et al. 1998	Schaefer et al. 2013	Schmitt and Brunner 1997	Sutkus et al. 2001	EASA 2010	- / -
Provision of prognosis	Prognosis for 2050	Prognosis for 2025	Prognosis for 2015	Prognosis 2011-2030	Prognosis for 2015	Prognoses for 2015 and 2020	Prognosis for 2056	Prognosis until 2050
Type of considered trajectories	Great circle	Real routing	Great circle	Great circle	Great circle	Great circle	Great circle	Great circle
Consideration of lateral trajectory inefficiencies	Yes	- / -	No	Yes, as part of total trajectory inefficiency	No	No	Yes	Yes
Consideration of vertical trajectory inefficiencies	No	- / -	No	Yes, as part of total trajectory inefficiency	No	No	No	No
Consideration of regional differences in trajectory inefficiency (number of regions)	Yes (7)	No	No	No	No	No	Yes (14)	Yes (21)
Consideration of departure and arrival inefficiencies	Yes, differentiation between departure, enroute and arrival areas	No	No	No	No	No	No	Yes, differentiation between departure, enroute and arrival airspaces
Consideration of Wind	No	No	No	No	No	No	No	No

A.4 Explanations to the download of the IAGOS data

For the purpose of research, the data is available out of charge provided on the homepage of IAGOS.¹ In a first step, to open the download form, the option *Searching by geolocation* is selected to then choose the main parameters within the first selection block. Here, altitude constraints and the period of time as well as parameters and aircraft are selected.² The tick has to be set on *raw data* to obtain the entire lateral trajectory data. Before further processing, the availability of the data is checked.


Altitude min	<input type="text" value="0.0"/>		
Altitude max	<input type="text" value="13000.0"/>		
Beginning Date	<input type="text" value="2012/01/01 00:00"/>		
Ending Date	<input type="text" value="2012/12/31 23:59"/>		
Select parameters	<input checked="" type="checkbox"/> Air Temperature <input type="checkbox"/> Aircraft Air Speed <input type="checkbox"/> Aircraft Ground Speed <input type="checkbox"/> Aircraft Static Temperature <input type="checkbox"/> CO <input type="checkbox"/> H2O <input type="checkbox"/> H2O Static Temperature		
Select aircraft	<input checked="" type="checkbox"/> mozaic 3 <input checked="" type="checkbox"/> mozaic 4 <input type="checkbox"/> mozaic 5		
Select data type	<input checked="" type="radio"/> raw data <input type="radio"/> averaged data <input type="radio"/> profiles		
You can check if data exist for your selection before launching extraction			<input type="button" value="Check"/>

Figure A.3: Selection of IAGOS data

Within the second selection block *Result format*, the checks are put at *A single file containing your selection*. Furthermore, the data is sorted by *date* and delimited by *TAB* ensuring a simple processing of individual values which are flagged by *NaN* if unknown. By pushing the *Extract* button the data is obtained in the TXT-format.

Result format

Type	<input checked="" type="radio"/> A single file containing your selection only <input type="radio"/> All the (entire) IAGOS flights files given at least one record is satisfying the selection
Sort by	<input checked="" type="radio"/> date <input type="radio"/> latitude <input type="radio"/> longitude <input type="radio"/> altitude
Delimiter used in files	<input type="radio"/> ; <input checked="" type="radio"/> TAB <input type="radio"/> SPACE
Flag value for unknown values	<input type="radio"/> -99.99 <input checked="" type="radio"/> NaN
<input type="button" value="Extract"/>	

Figure A.4: Result format of IAGOS data

¹ The data is provided on the homepage of IAGOS, cf. IAGOS [33].

² Besides *Air Temperature*, the aircraft *mosaic 2*, *mosaic 3*, *mosaic 4*, *iagos 1* and *iagos 2* were selected.

A.5 IAGOS aerodromes

Table A.2: Available aerodromes from IAGOS database extraction

#	City	ICAO code ¹	IATA code ²	Latitude [°]	Longitude [°]
1	Abu Dhabi	OMAA	AUH	24.443394	54.652708
2	Addis Ababa	HAAB	ADD	8.977922	38.799353
3	Ashgabat	UTAA	ASB	37.986817	58.360997
4	Asmara	HHAS	ASM	15.291908	38.911019
5	Atlanta	KATL	ATL	33.636700	-84.427864
6	Baku	UBBB	GYD	40.633333	49.566666
7	Boston	KBOS	BOS	42.362964	-71.006425
8	Calgary	CYYC	YYC	51.122614	-114.013347
9	Chicago	KORD	ORD	41.979333	-87.907389
10	Dallas	KDFW	DFW	32.897231	-97.037694
11	Doha	OTBD	DOH	25.274564	51.608378
12	Dusseldorf	EDDL	DUS	51.289425	6.766647
13	Frankfurt	EDDF	FRA	50.033306	8.570456
14	Guangzhou	ZGGG	CAN	23.392472	113.298794
15	Hanoi	VVNB	HAN	21.220328	105.805575
16	Ho Chi Minh City	VVTS	SGN	10.818792	106.651828
17	Hong Kong	VHHH	HKG	22.308919	113.914603
18	Jakarta	WIII	CGK	-6.125719	106.656506
19	Jeddah	OEJN	JED	21.681136	39.155486
20	Kagoshima	RJFK	KOJ	31.803375	130.719403
21	Khartoum	HSSS	KRT	15.589508	32.553164
22	Kuwait City	OKBK	KWI	29.226764	47.979953
23	Lagos	DNMM	LOS	6.577378	3.321167
24	Luanda	FNLU	LAD	-8.858311	13.231089
25	Madras (Chennai)	VOMM	MAA	12.994472	80.180464
26	Manila	RPLL	MNL	14.508647	121.019581
27	Muharraq	OBBI	BAH	26.267919	50.636950
28	Muscat	OOMS	MCT	23.592858	58.281797
29	Nanjing	ZSNJ	NKG	31.732139	118.863136
30	New York	KJFK	JFK	40.639750	-73.778925
31	Okinawa	ROAH	OKA	26.195811	127.645864
32	Osaka	RJGG	NGO	34.858417	136.805394
33	Philadelphia	KPHL	PHL	39.872250	-75.240867
34	Qingdao	ZSQD	TAO	36.266042	120.374531
35	Rio de Janeiro	SBGL	GIG	-22.808903	-43.243647
36	Riyadh	OERK	RUH	24.957458	46.698853
37	Seoul	RKSI	ICN	37.464139	126.440533
38	Shanghai	ZSPD	PVG	31.144086	121.792414
39	Shenyang	ZYTX	SHE	41.640006	123.483439
40	Singapore	WSSS	SIN	1.350164	103.994378
41	Taipei	RCTP	TPE	25.077506	121.233261
42	Tel Aviv	LLBG	TLV	32.011650	34.886194
43	Tokyo	RJAA	NRT	35.765278	140.385556
44	Toronto	CYYZ	YYZ	43.676661	-79.630644
45	Vancouver	CYVR	YVR	49.194694	-123.183967
46	Vienna	LOWW	VIE	48.110278	16.569722
47	Windhoek	FYWH	WHD	-22.479894	17.470950
48	Xiamen	ZSAM	XMN	24.544131	118.127667
49	Zhengzhou	ZHCC	CGO	34.519356	113.841131

¹ For ICAO codes and aerodrome WGS-coordinates cf. ICAO [40].

² Cf. IATA [34].

A.6 Inefficiency analysis of IAGOS trajectories

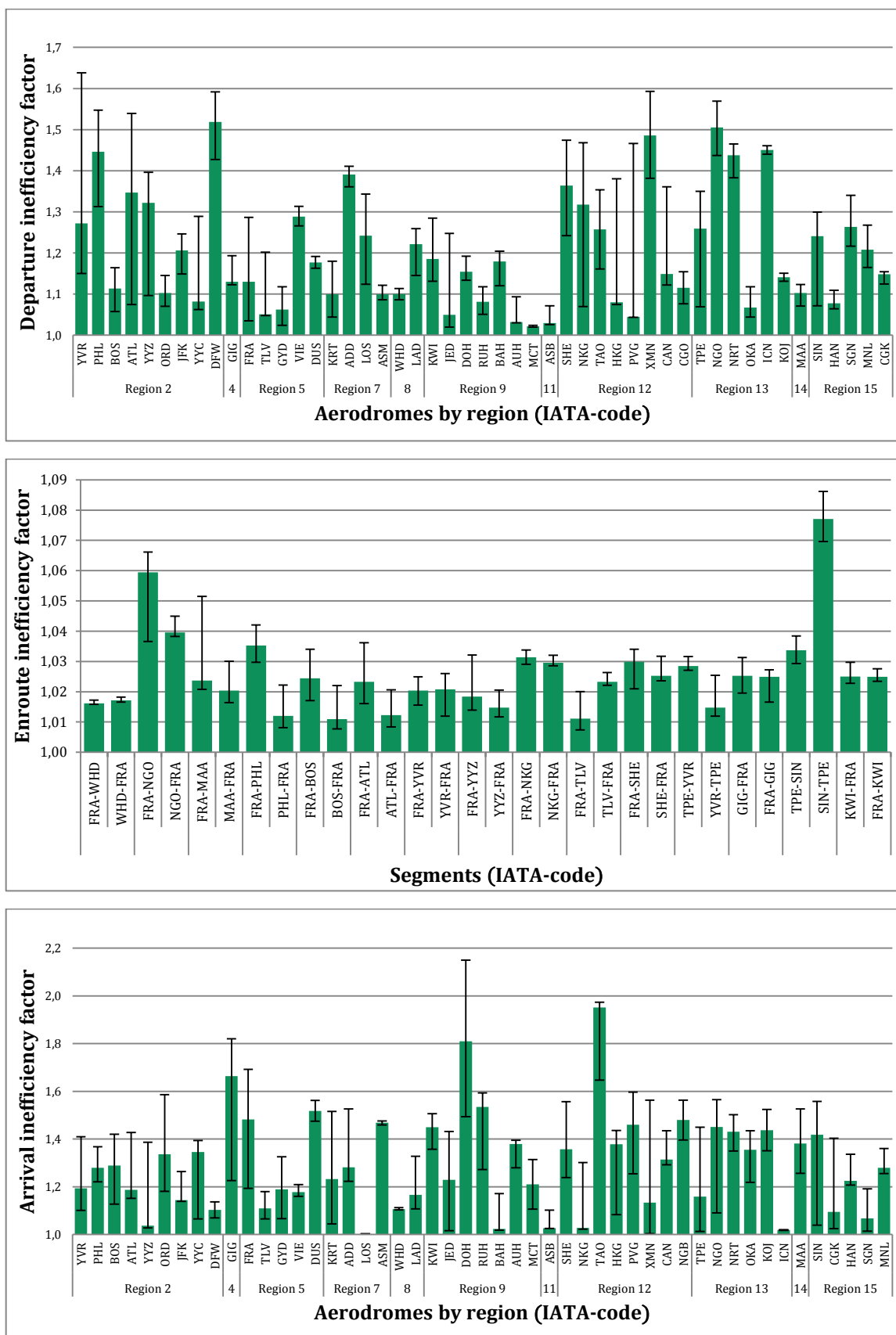


Figure A.5: Inefficiency analysis of real data trajectories

A.7 Distance relative to GC of IAGOS and the model

Table A.3: Distance relative to GC of IAGOS and the model ¹

Route	Distance _{rel,IAGOS}	Distance _{rel,model}	Δ Distance _{rel}
FRA-WHD	1.01711	1.05203	0.03493
WHD-FRA	1.02588	1.05171	0.02584
FRA-NGO	1.06552	1.05750	-0.00803
NGO-FRA	1.04635	1.05720	0.01085
FRA-MAA	1.03144	1.04393	0.01249
MAA-FRA	1.02921	1.04362	0.01441
FRA-PHL	1.04201	1.04167	-0.00034
PHL-FRA	1.03133	1.04299	0.01166
FRA-BOS	1.03308	1.04323	0.01015
BOS-FRA	1.02743	1.04390	0.01648
FRA-ATL	1.02794	1.03980	0.01186
ATL-FRA	1.02530	1.04031	0.01501
FRA-YVR	1.02633	1.04523	0.01889
YVR-FRA	1.02861	1.04525	0.01664
FRA-YYZ	1.02297	1.04281	0.01984
YYZ-FRA	1.02865	1.04297	0.01432
FRA-NKG	1.03537	1.05564	0.02027
NKG-FRA	1.03397	1.05549	0.02152
FRA-TLV	1.01699	1.04418	0.02719
TLV-FRA	1.03770	1.04440	0.00669
FRA-SHE	1.03872	1.05898	0.02026
SHE-FRA	1.03702	1.05894	0.02192
TPE-YVR	1.03242	1.05062	0.01820
YVR-TPE	1.02419	1.05121	0.02702
GIG-FRA	1.02976	1.04400	0.01424
FRA-GIG	1.03475	1.04415	0.00939
TPE-SIN	1.08356	1.05468	-0.02888
SIN-TPE	1.04992	1.05579	0.00588
KWI-FRA	1.04353	1.04406	0.00053
FRA-KWI	1.03562	1.04291	0.00730
Total²	1.03289	1.04861	0.01572

¹ The values are calculated according to Equation (4.1).

² Total values and weighted by frequency.

A.8 Burned fuel relative to GC of IAGOS and the model

Table A.4: Burned fuel relative to GC of IAGOS and the model ¹

Route	BurnedFuel _{rel,IAGOS}	BurnedFuel _{rel,model}	Δ BurnedFuel _{rel}
FRA-WHD	1.02059	1.06308	0.04249
WHD-FRA	1.03126	1.06270	0.03144
FRA-NGO	1.08128	1.07135	-0.00993
NGO-FRA	1.05726	1.07098	0.01373
FRA-MAA	1.03790	1.05307	0.01517
MAA-FRA	1.03524	1.05269	0.01745
FRA-PHL	1.04895	1.04857	-0.00038
PHL-FRA	1.03631	1.05010	0.01380
FRA-BOS	1.03745	1.04934	0.01189
BOS-FRA	1.03098	1.05009	0.01911
FRA-ATL	1.03387	1.04831	0.01444
ATL-FRA	1.03065	1.04893	0.01828
FRA-YVR	1.03179	1.05474	0.02296
YVR-FRA	1.03452	1.05477	0.02025
FRA-YYZ	1.02652	1.04993	0.02340
YYZ-FRA	1.03317	1.05011	0.01693
FRA-NKG	1.04308	1.06822	0.02514
NKG-FRA	1.04140	1.06804	0.02664
FRA-TLV	1.01666	1.04328	0.02662
TLV-FRA	1.03706	1.04348	0.00643
FRA-SHE	1.04679	1.07150	0.02470
SHE-FRA	1.04468	1.07145	0.02677
TPE-YVR	1.04000	1.06288	0.02288
YVR-TPE	1.02987	1.06374	0.03387
GIG-FRA	1.03671	1.05456	0.01786
FRA-GIG	1.04290	1.05475	0.01185
TPE-SIN	1.08314	1.05424	-0.02891
SIN-TPE	1.04954	1.05534	0.00580
KWI-FRA	1.04467	1.04553	0.00087
FRA-KWI	1.03656	1.04435	0.00779
Total²	1.03867	1.05767	0.01901

¹ The values are calculated according to Equation (4.2).

² Total values and weighted by frequency.

A.9 Produced NO_x relative to GC of IAGOS and the model

Table A.5: Produced NO_x relative to GC of IAGOS and the model ¹

Route	ProducedNO _{x,rel,IAGOS}	ProducedNO _{x,rel,model}	Δ ProducedNO _{x,rel}
FRA-WHD	1.02283	1.07012	0.04729
WHD-FRA	1.03467	1.06969	0.03502
FRA-NGO	1.09076	1.07975	-0.01101
NGO-FRA	1.06380	1.07935	0.01554
FRA-MAA	1.04252	1.05958	0.01706
MAA-FRA	1.03960	1.05916	0.01956
FRA-PHL	1.05412	1.05372	-0.00040
PHL-FRA	1.03991	1.05541	0.01550
FRA-BOS	1.04029	1.05352	0.01322
BOS-FRA	1.03334	1.05431	0.02097
FRA-ATL	1.03835	1.05471	0.01637
ATL-FRA	1.03467	1.05542	0.02074
FRA-YVR	1.03529	1.06083	0.02554
YVR-FRA	1.03830	1.06086	0.02256
FRA-YYZ	1.02908	1.05524	0.02616
YYZ-FRA	1.03643	1.05544	0.01901
FRA-NKG	1.04782	1.07597	0.02816
NKG-FRA	1.04599	1.07578	0.02978
FRA-TLV	1.01548	1.04005	0.02458
TLV-FRA	1.03445	1.04024	0.00579
FRA-SHE	1.05198	1.07952	0.02754
SHE-FRA	1.04959	1.07947	0.02988
TPE-YVR	1.04443	1.07017	0.02574
YVR-TPE	1.03325	1.07128	0.03803
GIG-FRA	1.04078	1.06084	0.02006
FRA-GIG	1.04768	1.06105	0.01337
TPE-SIN	1.07843	1.05102	-0.02741
SIN-TPE	1.04665	1.05205	0.00540
KWI-FRA	1.04353	1.04483	0.00130
FRA-KWI	1.03569	1.04368	0.00799
Total²	1.04218	1.06333	0.02115

¹ The values are calculated according to Equation (4.3).

² Total values and weighted by frequency.

A.10 ATR₁₀₀ relative to GC of IAGOS and the model

Table A.6: ATR₁₀₀ relative to GC of IAGOS and the model ¹

Route	ATR _{100,rel,IAGOS}	ATR _{100,rel,model}	Δ ATR _{100,rel}
FRA-PHL	1.09961	1.05461	-0.04499
PHL-FRA	1.08436	1.05547	-0.02889
FRA-BOS	1.07697	1.05597	-0.02099
BOS-FRA	1.06924	1.05565	-0.01359
FRA-ATL	1.06870	1.05395	-0.01475
ATL-FRA	1.07185	1.05446	-0.01738
FRA-YVR	1.03605	1.05511	0.01906
YVR-FRA	1.03903	1.05506	0.01602
FRA-YYZ	1.09641	1.05538	-0.04103
YYZ-FRA	1.05113	1.05545	0.00432
Total²	1.06979	1.05511	-0.01467

¹ The values are calculated according to Equation (4.4).

² Total values and weighted by frequency.

A.11 Relative frequency of Distance_{rel} per segment

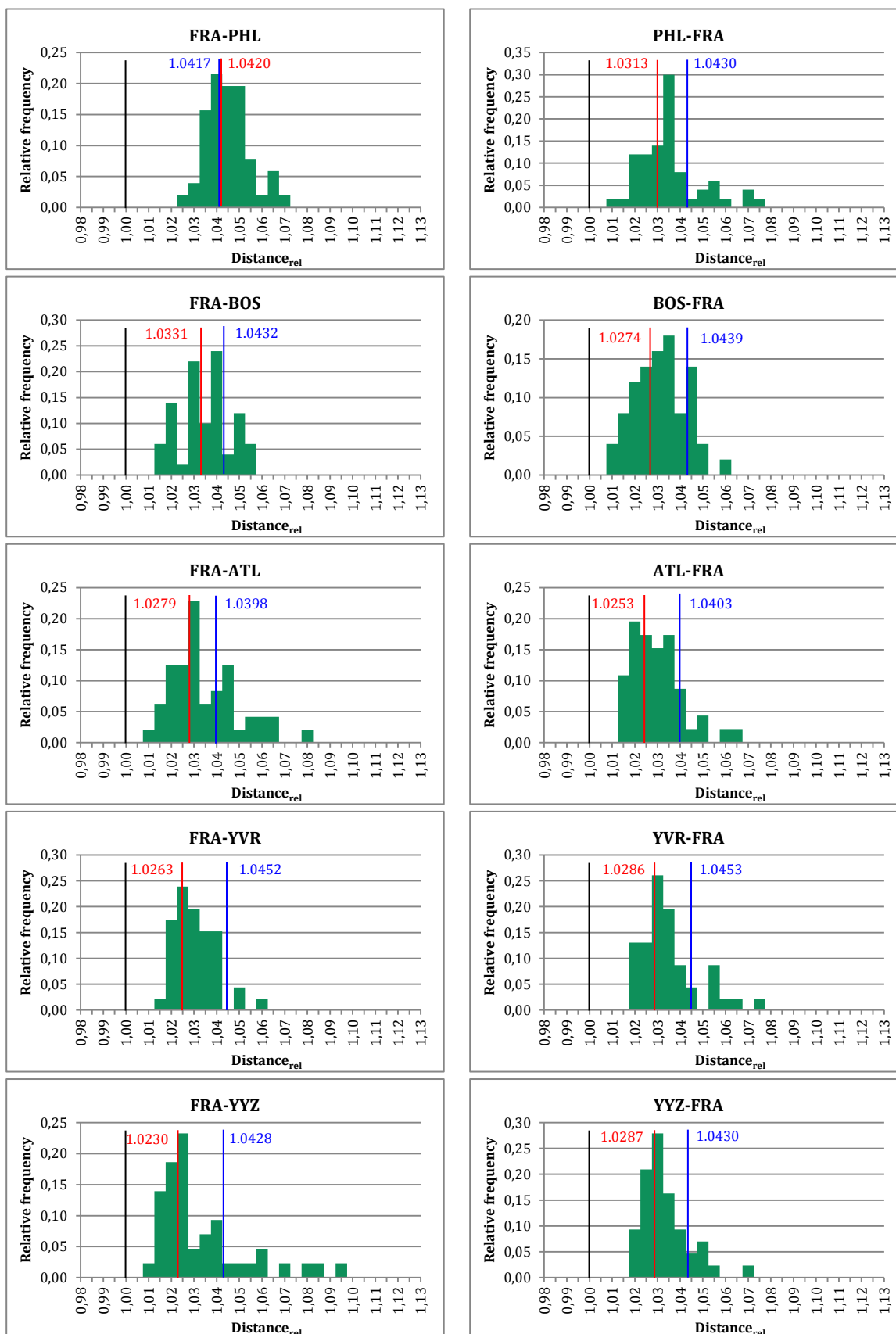


Figure A.6: Relative frequency of Distance_{rel} per segment

A.12 Relative frequency of BurnedFuel_{rel} per segment

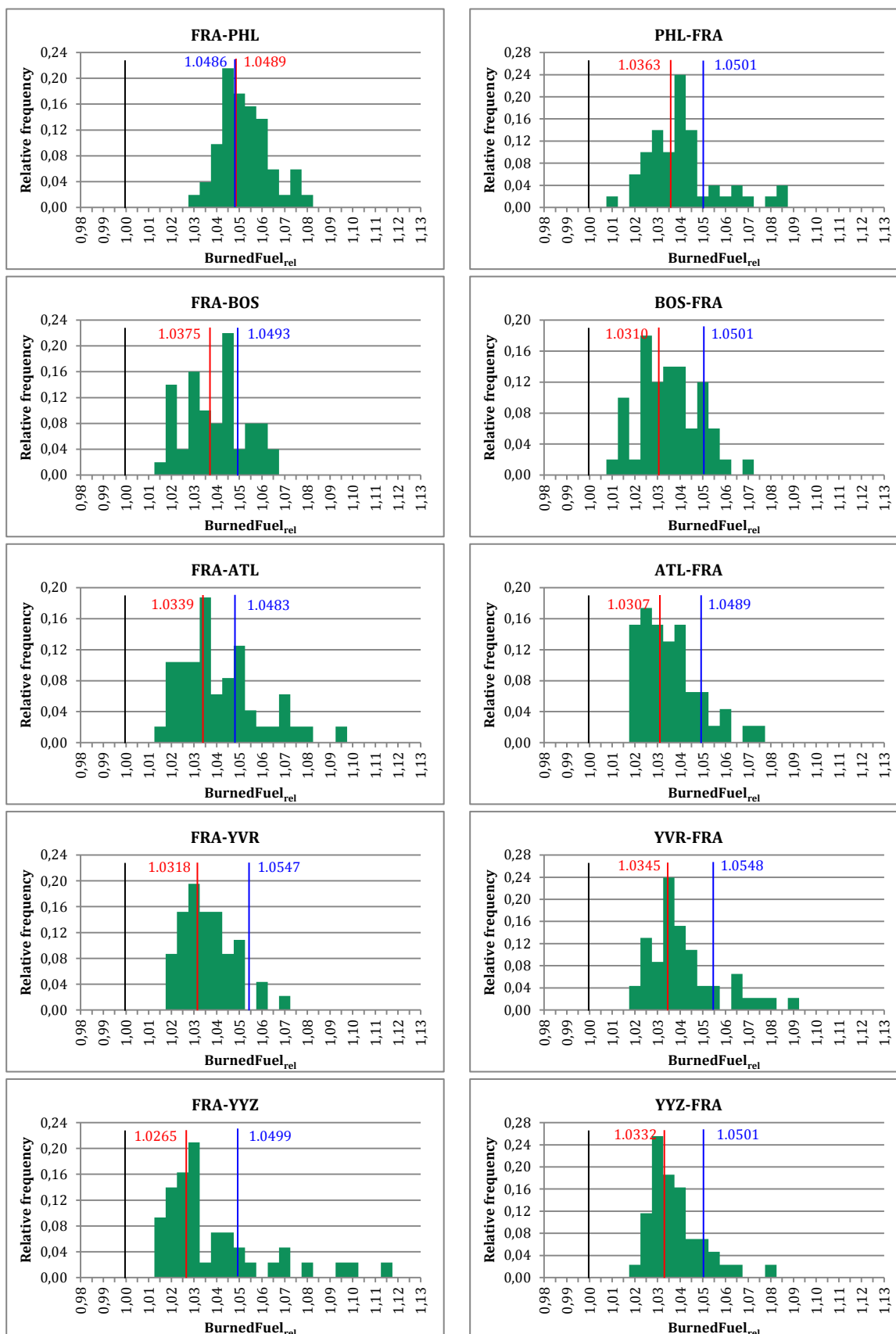


Figure A.7: Relative frequency of BurnedFuel_{rel} per segment

A.13 Relative frequency of ProducedNO_{x,rel} per segment

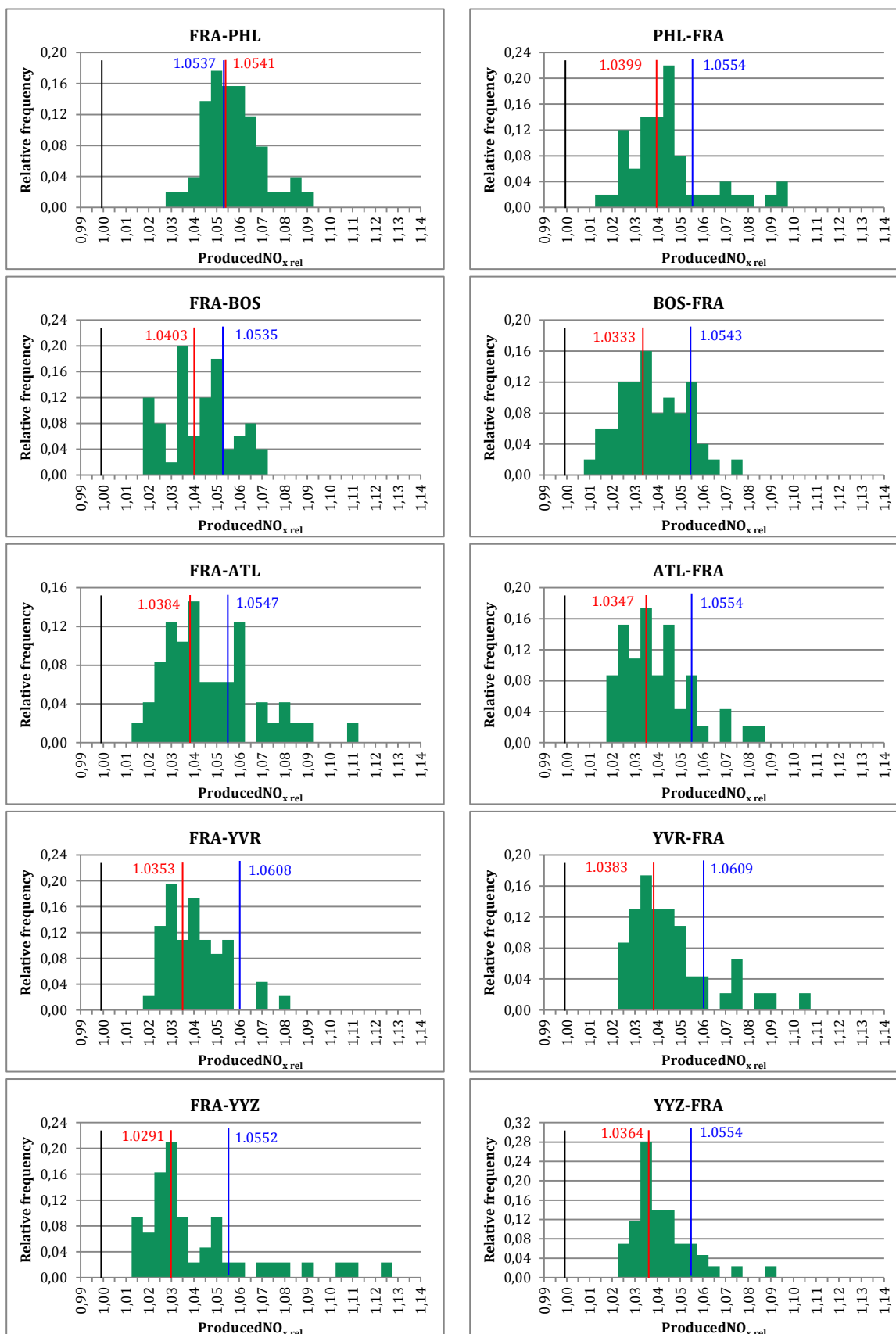


Figure A.8: Relative frequency of ProducedNO_{x,rel} per segment

A.14 Relative frequency of $ATR_{100,rel}$ per segment

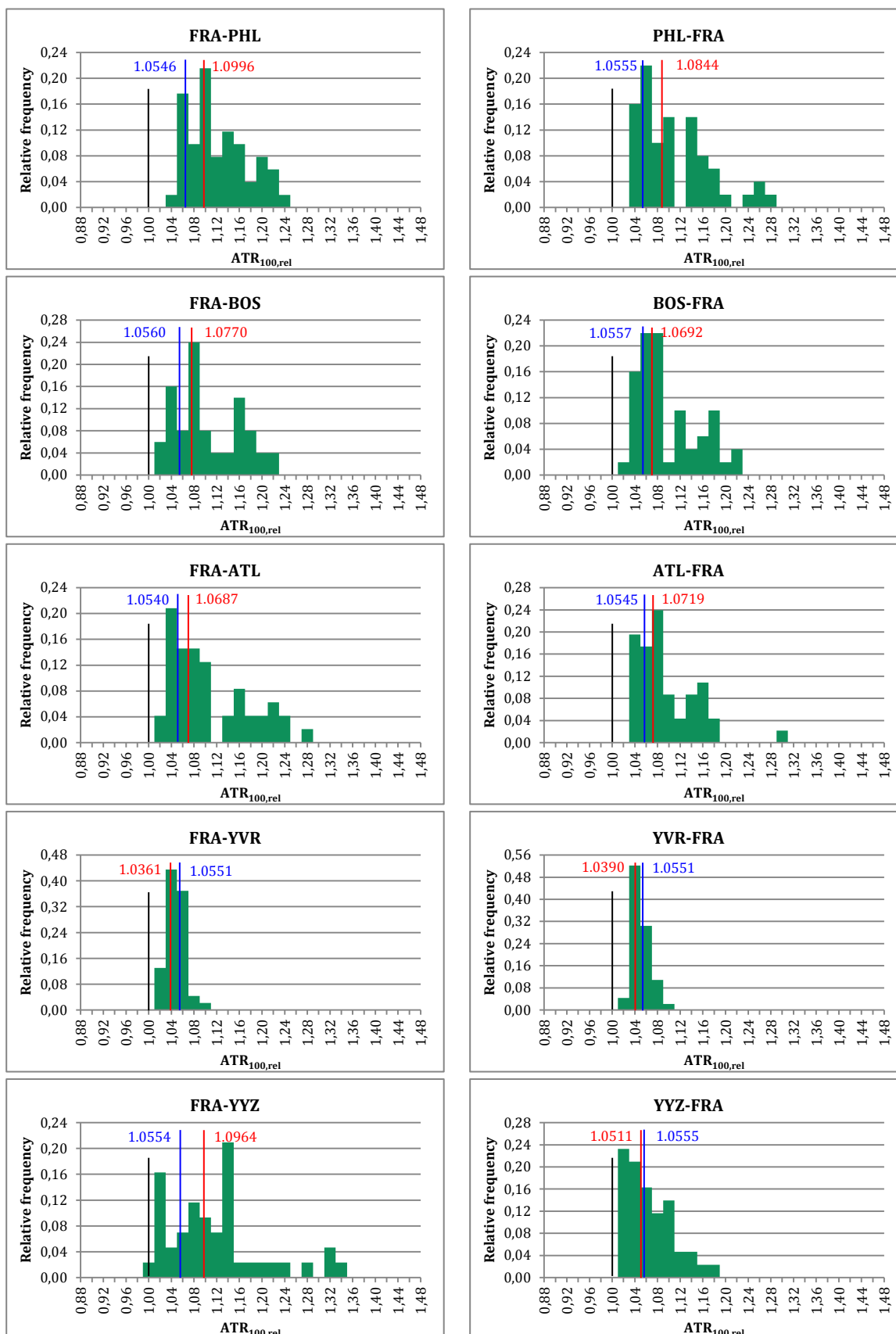


Figure A.9: Relative frequency of $ATR_{100,rel}$ per segment

List of references

- [1] AFRICAN AVIATION, *European airlines dominate African sky*, 1990, available at http://africanaviation.com/European_airlines_dominate_African_sky.html (accessed on November 2, 2015).
- [2] AIRBUS, *A340-300*, available at <http://www.airbus.com/aircraftfamilies/passengeraircraft/a340family/a340-300/> (accessed on November 4, 2015).
- [3] AIRPORT COUNCIL INTERNATIONAL, *ACI Releases its 2012 World Airport Traffic Report*, available at <http://www.aci.aero> (accessed on December 10, 2015).
- [4] AIRSERVICES AUSTRALIA, *OneSKY*, available at <http://www.airservicesaustralia.com/projects/onesky-australia/> (accessed on November 2, 2015).
- [5] BRONSTEIN, I.N.; SEMENDJAJEW, K.A.; MUSIOL, G.; MUEHLIG, H., *Taschenbuch der Mathematik*, Harri Deutsch, 2006.
- [6] CIVIL AVIATION AUTHORITY, *Flight efficiency metric calculation and annual review protocol*, available at <http://www.caa.co.uk/default.aspx?catid=5&pagetype=90&pageid=16698> (accessed on June 29, 2015).
- [7] CIVIL AVIATION SAFETY AUTHORITY, *Aeronautical Review of Upper Airspace Services*, 2011.
- [8] DFS DEUTSCHE FLUGSICHERUNGS GMBH, *SESAR*, available at https://www.dfs.de/dfs_homepage/de/Europa/SESAR/ (accessed on November 2, 2015).
- [9] DIE WELT, *Das sind die laengsten Nonstop-Fluege der Welt*, available at <http://www.welt.de/reise/article124291648/Das-sind-die-laengsten-Nonstop-Fluege-der-Welt.html> (accessed on October 27, 2015).
- [10] DUBOIS, D.; PAYNTER, G., *Fuel Flow Method 2 for Estimating Aircraft Emissions*, SAE Technical Paper 2006-01-1987, 2006.
- [11] DUSSELDORF AIRPORT, *Verkehrszahlen*, available at <http://www.dus.com/de-de/konzern/unternehmen/zahlen-und-fakten/verkehrszahlen> (accessed on December 10, 2015).
- [12] EASA, *Study on Aviation and Economic Modelling (SAVE)*, 2010.
- [13] ECONOMIC RESEARCH CENTER, *Traffic Congestion in Europe*, Report of the 110th Round Table on Transport Economics, 1998.
- [14] EUROCONTROL, *Enhanced Flight Efficiency Indicators*, 2004.
- [15] EUROCONTROL, *Vertical Flight Efficiency*, 2008.
- [16] EUROCONTROL, *Comparison of ATM-related performance: U.S. - Europe*, 2013.

-
- [17] EUROCONTROL, *Performance Indicator - Horizontal Flight Efficiency*, 2014.
- [18] EUROCONTROL, *Performance Review Report: An assessment of Air Traffic Management in Europe during the calendar year 2013*, 2014.
- [19] EUROCONTROL/FAA, *2012 Comparison of Air Traffic Management-related Operational performance: U.S./Europe*, 2013.
- [20] EUROPEAN COMMISSION, *Single Sky: Commission acts to unblock congestion in Europe's airspace*, available at http://europa.eu/rapid/press-release_IP-13-523_en.htm (accessed on June 29, 2015).
- [21] EYERS, C. J.; NORMAN, P.; MIDDEL, J.; PLOHR, M.; ET AL., *Aero2k Global Aviation Emissions Inventories for 2002 and 2025*, 2004.
- [22] FAA FEDERAL AVIATION ADMINISTRATION, *NextGen*, available at <https://www.faa.gov/nextgen/> (accessed on November 2, 2015).
- [23] FRAPORT, *Air Traffic Statistics 2012*, available at <http://www.fraport.com/en.html> (accessed on December 10, 2015).
- [24] GARDNER, R. M., et al., *Global Aircraft Emissions Inventories for 1991/1992 and 2015*, 1998.
- [25] GHOSH, R.; KOELKER, K.; TEREKHOV, I., *Future Passenger Air Traffic Modelling: A theoretical Concept to integrate Quality of Travel, Cost of Travel and Capacity Constraints*, 2015.
- [26] GHOSH, R.; TEREKHOV, I., *Future Passenger Air Traffic Modelling: Trend Analysis of the Global Passenger Air Travel Demand Network*, 2015.
- [27] GMELIN, T. C., *Zusammenfassende Darstellung der Effizienzpotenziale bei Flugzeugen unter besonderer Beruecksichtigung der aktuellen Triebwerkstechnik sowie der absehbaren mittelfristigen Entwicklungen*, 2008.
- [28] GRU AIRPORT, *Statistics*, available at <http://www.gru.com.br/en-us/Gru-Airport-Institucional/Statistics> (accessed on December 10, 2015).
- [29] HACK, K. H., *Aviation Meteorology*, 2nd ed., Karl Heinz Hack 2008, 2008.
- [30] HANNOVER AIRPORT, *Facts & Figures*, available at <http://www.hannover-airport.de/en/company/about-us/daten-und-fakten/> (accessed on December 10, 2015).
- [31] HOWELL, D.; BENNET, M.; BONN, J., *Estimating the enroute efficiency benefits pool*, 2003.
- [32] HOWE-VEENSTRA, R., *Commercial Aircraft Trajectory Optimization and Efficiency of Air Traffic Control Procedures*. Master Thesis, 2011.
- [33] IAGOS, available at <http://www.iagos.org> (accessed on October 19, 2015).
- [34] IATA, *Airline and Airport Code Search*, available at <http://www.iata.org/publications/Pages/code-search.aspx> (accessed on August 6, 2015).
- [35] ICAO, *ICAO ATFM Status: Level of implementation of Air Traffic Flow Management*, available at <http://gis.icao.int/eATFM/> (accessed on November 2, 2015).

-
- [36] ICAO, *Middle East Regional office*, available at <http://www.icao.int/MID/Pages/default.aspx> (accessed on June 10, 2015).
- [37] ICAO, *Air Navigation Plan: Caribbean and South American Regions*, available at <http://www.icao.int/Pages/default.aspx> (accessed on June 5, 2015).
- [38] ICAO, *Air Traffic Flow Management (ATFM) Communications Handbook for the Asia Pacific Region*, Bangkok, 2009.
- [39] ICAO, *Manual on Collaborative Air Traffic Flow Management*. Doc 9971 AN/485, 2nd ed., 2014.
- [40] ICAO, *GIS viewer*, available at <http://gis.icao.int/icaoviewernew/#/> (accessed on May 31, 2015).
- [41] ICAO, *North Atlantic Operations and Airspace Manual*, 2014th ed., (2015).
- [42] INCHEON AIRPORT, *IIAC Airport Statistics*, available at http://www.airport.kr/iiac/pds/sta/Sta_01.iaa?lang=E (accessed on December 10, 2015).
- [43] JEPPESEN, *SBSP Airport Charts*, available at http://download.diegolima.org/Cartas%20Aereas/app_dep/ (accessed on November 2, 2015).
- [44] JEPPESEN, *EDDS Airport Charts*, available at www.swe-gaming.com/fsx/approachcharts/EDDS.pdf (accessed on November 2, 2015).
- [45] JEPPESEN, *EDDL Airport Charts*, available at www.swe-gaming.com/fsx/approachcharts/EDDL.pdf (accessed on November 2, 2015).
- [46] JEPPESEN, *RKSI Airport Charts*, available at www.yinlei.org/x-plane10/jep/RKSI.pdf (accessed on November 2, 2015).
- [47] JEPPESEN, *EDDF Airport Charts*, available at www.fly-sea.com/charts/EDDF.pdf (accessed on November 2, 2015).
- [48] JEPPESEN, *EDDM Airport Charts*, available at www.fly-sea.com/charts/EDDM.pdf (accessed on November 2, 2015).
- [49] JEPPESEN, *LFPG Airport Charts*, available at www.fly-sea.com/charts/LFPG.pdf (accessed on November 2, 2015).
- [50] JEPPESEN, *EDDV Airport Charts*, available at http://www.german-flightcenter.com/portal/Charts/Germany_13_2009/EDDV.pdf (accessed on December 10, 2015).
- [51] JEPPESEN, *ZBAA Airport Charts*, available at www.ivaocn.org/charts/Beijing2008/ZBAA%20Charts.pdf (accessed on November 2, 2015).
- [52] JEPPESEN, *KATL Airport Charts*, available at <https://de.flightaware.com/resources/airport/KATL/procedures> (accessed on November 2, 2015).
- [53] KAGEYAMA, K.; FUKUDA, Y., *Study on analysis method of horizontal flight distance for ATM performance assessment*, 27th International Congress of the Aeronautical Science, 2010.

-
- [54] KETTUNEN, T., ET AL., *Flight efficiency studies in Europe and the United States*, 2005.
- [55] KRAMMER, P., *Evaluation of non-CO2 impacts from widespread use of aviation biofuels*. Master Thesis, 2011.
- [56] LIEBECK, R., *Advanced Subsonic Airplane Design & Economic Studies*, NASA CR-195443, 1995.
- [57] LUEHRS, B., *Erweiterung eines Trajektorienrechners zur Nutzung meteorologischer Daten für die Optimierung von Flugzeugtrajektorien*. Diplomarbeit, 2013.
- [58] MAIN ATM CENTRE, *Zonal Centres of the Russian Federation*, available at <http://www.matfmc.ru/eng/MAIN.html> (accessed on June 10, 2015).
- [59] MATHWORKS, *datenum*, available at <http://de.mathworks.com/help/matlab/ref/datenum.html> (accessed on October 27, 2015).
- [60] MATHWORKS, *distance*, available at <http://de.mathworks.com/help/map/ref/distance.html>.
- [61] MATHWORKS, *flatearthpoly*, available at <http://www.mathworks.com/help/map/ref/flatearthpoly.html> (accessed on July 21, 2015).
- [62] MATHWORKS, *Mapping Toolbox User's Guide*, available at <http://de.mathworks.com/help/map/index.html> (accessed on May 31, 2015).
- [63] MATHWORKS, *polyxpoly*, available at <http://de.mathworks.com/help/map/ref/polyxpoly.html>.
- [64] MATHWORKS, *reckon*, available at <http://de.mathworks.com/help/map/ref/reckon.html> (accessed on October 28, 2015).
- [65] MATHWORKS, *scircle1*, available at <http://de.mathworks.com/help/map/ref/scircle1.html> (accessed on October 28, 2015).
- [66] MATHWORKS, *track2*, available at <http://de.mathworks.com/help/map/ref/track2.html> (accessed on October 28, 2015).
- [67] MATHWORKS, *xml2struct*, available at <http://www.mathworks.com/matlabcentral/fileexchange/28518-xml2struct> (accessed on October 29, 2015).
- [68] MENSEN, H., *Handbuch der Luftfahrt*, 2nd ed., Springer-Verlag, Berlin Heidelberg 2003, 2013.
- [69] MUNICH AIRPORT, *Annual Traffic Report 2012: Air Traffic Statistics*, available at http://www.munich-airport.de/de/company/facts/verkehr/berichte/stat_jahber/index.jsp (accessed on December 10, 2015).
- [70] NIKLAß, M.; LUERS, B.; GREWE, V.; LUCKOVA, T.; ET AL., *Potential to reduce the climate impact of aviation by closure of airspaces*, 19th Air Transport Research Society (ATRS) World Conference, 2015.

-
- [71] NUIC, A.; MOUILLET, V., *User Manual for the Base of Aircraft Data (BADA) Family 4*, ECC Tech./Scien. Report No. 12/22/22-58, 2012.
- [72] REYNOLDS, T.G., *Analysis of Lateral Flight Inefficiency in Global Air Traffic Management*, Eighth AIAA Aviation Technology, Integration and Operations Conference, 2008.
- [73] REYNOLDS, T.G., *Effects of Airspace Charging on Airline Route Selection & Greenhouse Gas Emissions*, Ninth AIAA Aviation Technology, Integration, and Operations Conference (ATIO), 2009.
- [74] REYNOLDS, T.G., *ATM performance assessment using flight inefficiency metrics*, Transport Policy (34) (2014) 63–74.
- [75] SCHAEFER, M.; Jung, M.; Pabst, H., *The regional distribution of air traffic emissions in the past, present and future*, 2013.
- [76] SCHMITT, A.; BRUNNER, B., *Emissions from aviation and their development over time*, in: Pollutants from Air Traffic - Results of Atmospheric Research 1992-1997, pp. 37–52.
- [77] SEADAC, *Gridded Population of the World*, available at <http://sedac.ciesin.columbia.edu/data/collection/gpw-v3> (accessed on October 27, 2015).
- [78] SIMONE, N., *Development of a Rapid Global Aircraft Emissions Estimation Tool with Uncertainty Quantification*, Master Thesis, 2013.
- [79] SUTKUS, D.; BAUGHUM, S.; DUBOIS, D.; *Scheduled Civil Aircraft Emission Inventories for 1999: Database Development and Analysis*, NASA CR-2001-211216, 2001.
- [80] WILKERSON, J.T.; JACOBSON, M.Z.; MALWITZ, A.; BALASUBRAMANIAN, S., ET AL., *Analysis of emission data from global commercial aviation: 2004 and 2006*, Atmospheric Chemistry and Physics (10) (2010) 6391–6408.



Erklärung zur selbstständigen Bearbeitung einer Abschlussarbeit

Gemäß der Allgemeinen Prüfungs- und Studienordnung ist zusammen mit der Abschlussarbeit eine schriftliche Erklärung abzugeben, in der der Studierende bestätigt, dass die Abschlussarbeit „– bei einer Gruppenarbeit die entsprechend gekennzeichneten Teile der Arbeit [(§ 18 Abs. 1 APSO-TI-BM bzw. § 21 Abs. 1 APSO-INGI)] – ohne fremde Hilfe selbständig verfasst und nur die angegebenen Quellen und Hilfsmittel benutzt wurden. Wörtlich oder dem Sinn nach aus anderen Werken entnommene Stellen sind unter Angabe der Quellen kenntlich zu machen.“

Quelle: § 16 Abs. 5 APSO-TI-BM bzw. § 15 Abs. 6 APSO-INGI

Dieses Blatt, mit der folgenden Erklärung, ist nach Fertigstellung der Abschlussarbeit durch den Studierenden auszufüllen und jeweils mit Originalunterschrift als letztes Blatt in das Prüfungsexemplar der Abschlussarbeit einzubinden.

Eine unrichtig abgegebene Erklärung kann -auch nachträglich- zur Ungültigkeit des Studienabschlusses führen.

Erklärung zur selbstständigen Bearbeitung der Arbeit

Hiermit versichere ich,

Name: Hurst

Vorname: Adrian

dass ich die vorliegende Masterarbeit bzw. bei einer Gruppenarbeit die entsprechend gekennzeichneten Teile der Arbeit – mit dem Thema:

Development of a generic model to depict airspace-related trajectory inefficiencies for global air traffic scenarios

ohne fremde Hilfe selbständig verfasst und nur die angegebenen Quellen und Hilfsmittel benutzt habe. Wörtlich oder dem Sinn nach aus anderen Werken entnommene Stellen sind unter Angabe der Quellen kenntlich gemacht.

- die folgende Aussage ist bei Gruppenarbeiten auszufüllen und entfällt bei Einzelarbeiten -

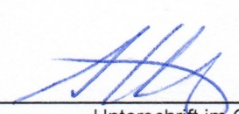
Die Kennzeichnung der von mir erstellten und verantworteten Teile der -bitte auswählen- ist erfolgt durch:

Hamburg

Ort

15.12.2015

Datum


Unterschrift im Original